Study of plasma turbulence by ultrafast sweeping reflectometry on the Tore Supra tokamak

Grégoire Hornung

Aix-Marseille Université

THÈSE DE DOCTORAT

École doctorale: *Physique et Sciences de la Matière*
Mention: **Énergie, Rayonnement, Plasma**

ÉTUDE DE LA TURBULENCE PLASMA PAR RÉFLECTOMÉTRIE À BALAYAGE ULTRA RAPIDE SUR LE TOKAMAK TORE SUPRA

Study of plasma turbulence by ultrafast sweeping reflectometry on the Tore Supra tokamak

présentée par

Grégoire Hornung

Soutenue publiquement le 02 octobre 2013 devant le jury composé de:

Pr. Stéphane heuraux	Rapporteur
Pr. Ulrich stroth	Rapporteur
Dr. Ghassan antar	Examinateur
Pr. Peter beyer	Examinateur
Dr. Frédéric clairet	Directeur de thèse
Dr. Gloria falchetto	Responsable CEA

Laboratoire d'accueil:
Institut de Recherche sur la Fusion par confinement Magnétique
CEA-Cadarache
13108 Saint-Paul-Lez-Durance, France

"Und was in schwankender Erscheinung schwebt, Befestigt mit dauernden Gedanken"

Johann Wolfgang von Goethe

Abstract

Plasma turbulence limits the performance of fusion reactors. Measuring and characterizing the turbulence properties is therefore a crucial issue in order to understand such phenomena. The goal of this thesis is to study the properties of plasma turbulence from ultrafast sweeping reflectometry measurements performed on the Tore Supra Tokamak. Reflectometry is a radar technique that is used to measure the electron density and its fluctuations. In the first part, we compare Langmuir probe and reflectometer data and discuss the possibility to characterize turbulence properties from the reconstructed fluctuating density profiles. Then, we show that the radial variation of the time and spatial scales of the turbulence as well as its radial velocity can be estimated from a cross-correlation analysis applied to the raw reflectometer signals. The modifications of the turbulence properties observed during a parametric scan are interpreted in the light of TEM and ITG turbulence. Finally, we show that the additional heating leads to a significant increase of the radial velocity in the plasma close to the tokamak wall.

Acknowledgements

Je tiens d'abord à exprimer ma reconnaissance aux membres du Jury. C'est grâce aux échanges réguliers avec Stéphane Heuraux que je me suis formé aux théories de la réflectométrie. J'ai découvert la recherche sous la direction de Ulrich Stroth, je le remercie tout particulièrement de m'avoir initié à cette discipline si exigeante qu'est la physique des plasmas. A de nombreuses occasions, j'ai débattu sur la nature de la turbulence avec Ghassan Antar. Ces discussions ont été parfois mouvementées mais toujours très enrichissantes. Enfin, je remercie Peter Beyer pour l'intérêt porté à mes travaux et pour avoir présidé le Jury.

Cette thèse s'est déroulée au sein de l'Institut de Recherche sur la Fusion par confinement Magnétique. Je remercie Xavier Litaudon et Alain Becoulet pour m'avoir offert la possibilité d'intégrer leurs équipes et ainsi, d'avoir pu être au contact de nombreux experts.

La direction et l'encadrement de cette thèse furent respectivement assurés par Frédéric Clairet et Gloria Falchetto. Frédéric Clairet a porté l'ambitieux projet de réflectomètre à balayage ultra rapide. L'analyse et l'interprétation des signaux du réflectomètre furent le coeur de mon projet de thèse et m'ont permis d'acquérir des compétences multiples. Bien que son domaine d'expertise se situe hors de la réflectométrie, Gloria a toujours su comprendre mes travaux et a contribué significativement aux résultats obtenus dans cette thèse. Je les remercie tout deux sincèrement pour leurs disponibilités mais aussi pour m'avoir permis de développer des compétences de travail en équipe. Ces compétences sont souvent placées au second plan dans les activités de recherche, je les crois au contraire essentielles à la réussite des projets scientifiques.

Ce projet de thèse est à l'intersection de plusieurs branches des sciences de la fusion nucléaire.

Il y a d'abord bien sûr la réflectométrie. J'ai une pensée chaleureuse pour Christine Bottereau, Jean-Claude Giacalone et Diego Molina qui ont participé au développement et à la maintenance des réflectomètres. Sébastien Hacquin m'a apporté une aide précieuse sur les questions relatives à la modélisation numérique de la réflectométrie. Ce projet s'inscrit dans la continuité des travaux de thèse de Laure Vermare et Thomas Gerbaud. La lecture de leurs manuscrits m'a permis de prendre connaissance des possibilités offertes par la réflectométrie à balayage et ainsi d'affiner mes axes de recherches. Merci enfin à Roland Sabot qui m'a suggéré l'étude des spectres fréquentiels, piste qui s'est révélée très fructueuse et qui mérité d'être davantage explorée.

Vient ensuite la turbulence, domaine difficile mais passionnant. J'ai grandement apprécié la pédagogie dont Xavier Garbet et Yannick Sarazin ont fait preuve à mon égard. Phillipe Ghendrih m'a formé à l'utilisation du code TOKAM2D. Cet outil numérique fut

essentiel pour interpréter les données de turbulence de SOL. Je l'en remercie. J'ai une pensée toute particulière pour mon ami Berhnard Nold avec qui j'ai beaucoup échangé, malgré la distance qui nous séparait. J'ai très régulièrement interagi avec la "nouvelle" génération de chercheur de l'IRFM. Leurs portes m'étaient toujours ouvertes. Nicolas Fedorczak et Patrick Tamain m'ont énormément appris sur la turbulence de bord, tant d'un point de vue expérimental que théorique. J'ai longuement discuté avec Guilhem Dif-Pradalier de la possibilité de mettre en évidence un transport non-local des particules. Cette question reste cependant ouverte et j'espère pouvoir contribuer prochainement à ce débat. Je tiens à témoigner à ces trois personnes mon admiration, mon amitié et bien sûr à leur adresser mes remerciements.
Il y aussi eu des activités annexes qui m'ont amené à collaborer avec de nombreux experts. J'ai apprécié travailler avec Jamie Gunn sur les signaux des sondes de Langmuir. Les discussions avec Marc Goniche et Laurent Colas au sujet de l'impact du chauffage additionnel sur la turbulence furent très fructueuses. Phillipe Moreau m'a apporté son expertise de pilote sur les questions relatives à la base de données Tore Supra et à la localisation des objets dans le Tore. Qu'ils en soient remerciés.
Même si je n'ai pas eu l'occasion de travailler directement avec eux, je tiens à remercier Marina Becoulet, Guillaume Latu, Virgine Grandgirard, Chantal Passeron, Patrick Maget, Olivier Thomine, Ahmed Ratnani, Eric Nardon, Rémi Dumont, Didier Elbèze et Rémi Guirlet pour les moments passés en leur compagnie, notamment lors des pauses café.
J'ai appris comment valoriser les compétences acquises au cours cette thèse grâce à Christian Clément, je l'en remercie. Je dois beaucoup à Martine Tani qui m'a offert la possibilité d'animer un module de physique au sein de l'ENSGSI. Nos échanges furent source d'ouverture et d'épanouissement.
Je tiens à accorder ici une place importante aux thésards de l'IRFM. Avant d'être des collègues, ils sont surtout des amis. Commençons par ceux qui m'ont précédés. Antoine M., David, Antoine S. et Jérémie. Ceux là en savaient beaucoup mais étaient toujours prêt à partager. Mes camarades de promotion s'appellent Farah, Timothée, Didier, Pierre, Stéphanie, Jonathan et Romain . Merci à eux pour les bons moments passés ensemble à Cadarache, en conférence ou ailleurs. Puis viennent les plus jeunes. Ceux qui ne sont pas encore passés de l'autre coté. Il y a bien sûr ce sacré François qui ne manque jamais une occasion de nous faire partager les nouvelles du monde, qu'elles soient bonnes ou mauvaises. Heureusement que Thomas est là pour temporiser .... ces deux là forment un joli couple. J'adresse mes encouragements à Hugo A. qui s'est récemment lancé dans la réflectométrie mais qui a déjà obtenu de beaux résultats. Merci à Filou de m'avoir fait découvrir beaucoup de belles musiques. Pensée pour Yue qui venait nous voir quand le climat parisien devenait insupportable, un peu de compassion pour Fabien qui quitte bientôt Aix pour s'installer à Paris. Compassion également pour Damien et JB qui passe

une bonne partie de leur thèse à JET ... Souhaitons aussi bonne chance aux petits nouveaux, j'ai nommé Olivier et Quentin. Enfin j'adresse une mention spéciale à Hugo B. et Clothilde avec qui j'ai eu le plaisir de partager mon bureau.
La dernière partie de ces remerciements sera consacrée aux amis et à la famille. J'ai partagé pendant un temps mon lieu de vie avec Clément, Névennick, Antoine B., Lucie B., Sarah et bien sûr Etienne *le bon fifou*. Merci à vous de m'avoir supporté... Ces trois années passées à Aix furent agréables grâce à la compagnie de nombreuses personnes dont Benji & Laeti, Clem, Laura & Alex, Céline & Cyril, et bien d'autres encore! Merci également au *hardcore* thionvillois composé de Cec, Charlène, Vins, PL, Kéké, Auré, Gaelle et Zen. Merci enfin aux bons copains qui habitent un peu plus loin, parmi eux figurent Alix, Céline, Seb, Vivien, Marie & Guillaume, Charlotte, Steph,Vincent P., Caco, Marie & Hugo et Nico.

Pour finir, je tiens à remercier du fond du coeur, Catherine et Claire, Marc et Ben, la petite Jeanne et mes Parents. Ils ont été de solides piliers sur lesquels j'ai toujours pu m'appuyer.
Le plus grand des mercis est pour toi Clara. Ta gentillesse, ton amour, ta bonne humeur, ta patience et ton sourire furent essentiels à l'aboutissement de ces travaux de thèses.

Contents

Chapter 1

Introduction

The world energy consumption has been continuously increasing and has almost doubled in the past 40 years. Nowadays most of human activities heavily rely on fossil fuels, such as oil, gas or coal, which represents 82% of the world energy consumption, while the remaining is divided between renewable (12%) and nuclear energy (6%). Estimates based on the actual energy demand trend, show that the known resources of fossil fuels will be depleted in a time scale ranging between 40 years for oil to two hundred years for coal. In addition to availability issues, these resources are not equally distributed geographically, often leading to strong geopolitical tensions, which will inevitably increase as the resources diminish. Finally, the burning of fossil fuels is also believed to have a strong impact on our environment through the resulting CO_2 emissions, which, in the scientific community, are widely considered to play a significant role in the present global warming. These different economic, geopolitical, and environmental aspects show how important it is to undertake strong political commitments to reduce the dependence from fossil fuels by increasing the usage of existing alternative energy sources. Recent technological improvements improved the efficiency of renewable energies, however, those are still rather expensive. In parallel, research is being carried out to investigate the feasibility of a potentially new energy source, namely the nuclear fusion of light elements, such as that which fuels the Sun. Controlled nuclear fusion might provide a sustainable and environmentally viable solution to the energy problem.

Research is on-going on several scientific and technological issues that still need to be elucidated in order to achieve economically viable fusion power plants. Among those, a large effort is devoted within the plasma community to the understanding and control of the energy losses occurring due to turbulent phenomena in a fusion reactor, which can seriously affect its performance. The turbulent phenomena are still poorly understood due to the complexity of the physics at play and the difficulty of performing localized

and precise measurements in a fusion reactor environment.
This work aimed at bringing new insight on tokamak turbulence physics, thanks to an innovative radar-like technique used to measure density turbulent fluctuations in Tore Supra tokamak.
The basics of nuclear fusion and tokamak plasma physics are briefly reviewed in this introductory chapter. The main instabilities generating turbulent transport in a tokamak are also discussed, mainly aiming at establishing their temporal and spatial scales, which will be relevant for the experimental study.

1.1 Nuclear fusion

Among the different possible fusion reactions, the one which has the highest nuclear cross section occurs among two hydrogen isotopes, deuterium and tritium and is thus considered for a fusion reactor. The products of this reaction are an *alpha particle* (He^4) and a neutron

$$D + T \Rightarrow n + He^4 + 17.6MeV. \tag{1.1}$$

Most of the excess energy (80%) is carried as kinetic energy by the neutron and the remaining (20%) by the alpha particle.
In order to obtain fusion reactions, the positively charged deuterium and tritium nuclei need to be brought to sufficiently high energies to overcome their electrostatic repulsion, typically of the order of 100 keV. At these high energies, electrons and nuclei are not bound anymore and constitute a gas of charged particles which is called a *plasma*.
While in the Sun the confinement of the plasma results from the gravitational forces, on Earth, one of the ways explored to confine the plasma in a reactor is via magnetic fields as we will detail a bit further in the next section.

1.1.1 Lawson criterion

A fusion reactor should trivially produce more energy than it is powered with and be self-sustained. The condition under which fusion reactions can be maintained without any external energy input is referred to as *ignition*. The criterion to reach ignition for a power producing thermonuclear reactor was derived by Lawson [1] and specifies a minimum value of the so-called *triple product* of the ion density n, plasma temperature T and energy confinement time τ_E:

$$nT\tau_e \geq 2.7 \times 10^{21}\ m^{-3}\ keV\ s. \tag{1.2}$$

The energy confinement time can be understood as the typical time after which the plasma cools down when the heat sources are turned off, it thus measures the efficiency of the magnetic confinement.
This so-called Lawson criterion can be physically interpreted as the ratio of the energetic content of the plasma to its losses (or sources in a steady state). The fusion energy gain factor Q, is defined as the ratio of fusion power produced in a reactor to the power required to maintain the plasma in a steady state. The condition for which Q = 1 is named breakeven and means that 20% (for D-T fusion) of the heating power comes from fusion reactions. Q = 20 is thought to be enough for a viable power plant.
The future fusion device, ITER, was designed such to reach Q = 10 and that a significant fraction of the heating power can come from fusion reactions, thus proving the feasibility of a fusion-based production of energy on an industrial level.

1.2 Magnetic confinement

The magnetic confinement concept exploits the fact that the charged particles constituting the plasma are constrained to follow trajectories along the magnetic field lines. The charged particles are indeed free to move parallel to the magnetic field, but gyrate in a so-called Larmor orbit in the direction perpendicular to the field as a result of the Lorentz force. The characteristic scales of the gyromotion are the fast cyclotron pulsation $w_{cj} = ZeB/m_j$ and the Larmor radius $\rho_j = \sqrt{T_j m_j}/Z_j eB$[1]; j denoting the species with the charge $Z_j e$ and mass m_j, T_j and B the local temperature and magnetic field, respectively.

1.2.1 The tokamak configuration

Tamm and Sakharov in the 1950's devised a toroidal magnetic device, that they named *tokamak*, where the magnetic field lines close on themselves, so to avoid particle parallel losses. In the tokamak configuration a strong toroidal magnetic field is produced by external coils and an auxiliary poloidal magnetic field is generated by the current induced in the plasma itself. The combination of the toroidal and poloidal components of the magnetic field produces helical field lines enrolling around the torus, which therefore confine the plasma charged particles. Fig. 1.1 shows a schematic of the tokamak magnetic topology. As illustrated in Fig. 1.2, in the tokamak magnetic topology two regions can be distinguished: the core, where the magnetic field lines are closed, enclosed by the last closed magnetic field surface (LCFS in dashed line) and the Scrape-Off Layer (SOL)

[1]The expression of the Larmor radius given above is only valid if the distribution of the particle velocity is Maxwellian.

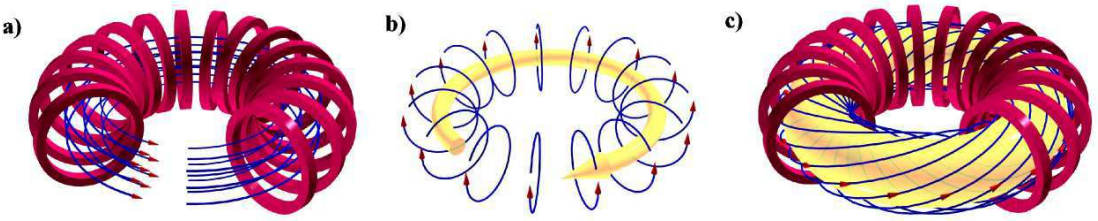

FIGURE 1.1: a) Toroidal magnetic field produced by the external coils. b) Poloidal magnetic field generated by the plasma current. c) Their sum produces helical magnetic field lines.

region, where magnetic field lines are connected to the walls.

On Tore Supra, the tokamak device located in CEA Cadarache, where the experimental studies of this thesis have been performed, the interaction between the plasma and the vacuum vessel is limited by a toroidal metallic component called a limiter.

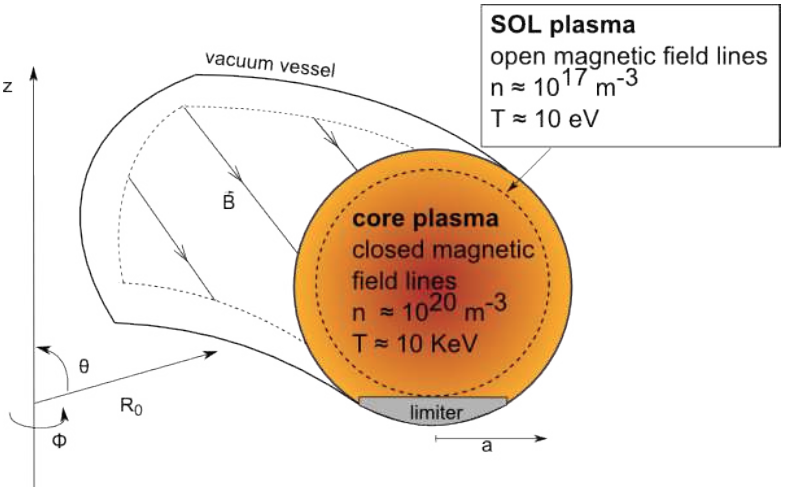

FIGURE 1.2: Schematic of a limited tokamak. R_0 and a are the major and minor radius, respectively.

Particle motions in a tokamak

Charged particles in a tokamak undergo several drifts induced by the magnetic topology. These drifts are rigorously derived in any plasma physics textbook and will be only briefly presented here. Usually, the particle dynamics is decoupled in three components: the gyration motion, the fast parallel dynamics along the magnetic field lines and the slower drifts perpendicular[2] to the field lines.

$$\vec{v} = \vec{v}_{gyro} + \vec{v}_{\parallel} + \vec{v}_{\perp}. \tag{1.3}$$

[2]In this manuscript, the terms *parallel* and *perpendicular* are always related to the unperturbed magnetic field direction.

The parallel velocity is of the order of the thermal velocity $v_{\|j} = \sqrt{T_j/m_j}$, which is thus about 40 times larger for electrons than for protons.
The perpendicular drift can be decomposed as the sum of the $E \times B$, ∇B, curvature and the polarization drift, the latter arises from time varying electric fields:

$$\vec{v}_\perp = \underbrace{\vec{V}_{E\times B}}_{E\times B\ drift} + \underbrace{\vec{V}_{\nabla B}}_{\nabla B\ drift} + \underbrace{\vec{V}_R}_{curvature\ drift} + \underbrace{\vec{V}_p}_{polarization\ drift} \tag{1.4}$$

The three first drifts can be cast in the general form

$$\vec{V}_f = \frac{1}{q}\frac{\vec{F}\times\vec{B}}{B^2}, \tag{1.5}$$

where F is the force acting on the particle. Except for the $E \times B$ drift, those depend on the charge of the particle.

The particle drifts are essential ingredients for the understanding of plasma turbulence. The charge-dependent drifts induce a charge separation and therefore an electric field. Small perturbations may then be amplified due to $E \times B$ drift, resulting in instabilities and turbulent convection. This mechanism is further explained in Sec. 1.4 and illustrated with two examples.

Trapped and passing particles

Charged particles in a tokamak can be cast in two classes, trapped and passing particles. Moving along the magnetic field lines in a tokamak, the charged particles experience a magnetic field which varies between a maximum and a minimum value. The magnetic field can thus act as a magnetic mirror, so that some particles can reverse direction and be reflected back, provided their velocity perpendicular to the field is sufficiently large relative to the parallel velocity (or equivalently their energy sufficiently low). Those particles are thus referred to as *trapped* whereas the particles which freely circulate along the magnetic flied lines are named as *passing*.

The condition for trapping can be expressed in terms of the particle energy

$$\varepsilon = \mu B\left(1 + \left(\frac{v_\|}{v_\perp}\right)^2\right) \lesssim \mu B_0(1+\epsilon), \tag{1.6}$$

where B_0 and μ are the field on the magnetic axis and the magnetic momentum, respectively and $\epsilon = r/R_0$ is the inverse aspect ratio of the torus. The fraction of trapped particles is given by $f_t \approx \sqrt{2\epsilon}$. In Tore Supra, taking $r \approx a \approx 0.7$ m leads to $\epsilon \approx 0.3$, so that about 77% of the particles are trapped.

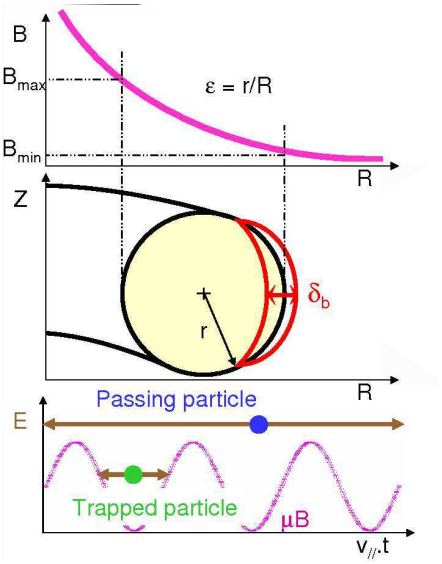

FIGURE 1.3: Top: charateristic magnetic field profile in a Tokamak. Middle: schematic of the banana orbit shape. Bottom: trapped and passing particles energy diagram. Reproduced from [2].

Trapped and passing particle motions are responsible for different perpendicular diffusive transport, as briefly outlined in the following section and can engender turbulence with different characteristics, as we attempted to explore experimentally (Sec. 7.1.3).

1.3 Particle and heat transport in a tokamak plasma.

Cross-field heat transport in a tokamak plasma is a topic of utmost importance because it determines the confinement time τ_E and therefore the performance of the reactor, as explained in Sec. 1.1.1. Consequently, substantial efforts have been dedicated to quantify this transport. The transport is modeled in terms of diffusion coefficients.

In a plasma, binary collisions are the basic mechanisms for the cross-field particle and heat transport, based on a classic random walk model. This is described by a diffusion coefficient, $\chi \sim \delta r^2/\tau_c$ where the characteristic walking time τ_c is given by the collision time (i.e. inverse of the collision frequency)and the step length δr is of the order of the Larmor radius, in a cylindrical geometry.
In a toroidal plasma this collisional transport is enhanced by particle drift orbit effects due to the inhomogeneous equilibrium magnetic field. This process is called neoclassical transport. Neoclassical transport coefficients can be derived for passing and trapped particles, depending on different regime of collisionality [2, 3]. However, the observed perpendicular transport in most tokamak plasmas, is much higher than the predicted neoclassical values, and is therefore referred to as *anomalous*. Understanding the physical mechanisms leading to this enhanced transport is one of the most important issues

for present magnetic fusion devices and future reactors. Enormous effort, both theoretical and computational, has been put to understand physics underlying the anomalous transport and then to match the predicted transport flux with that observed experimentally. It is now recognized that anomalous transport is caused by various turbulent fluctuations. The accurate measure and characterization of the turbulent fluctuations is therefore essential to the understanding of turbulence-driven anomalous transport.
In a quasi-steady turbulent plasma, the turbulent diffusivity coefficient can be estimated via the correlation length, L_c, and time, τ_c, of the fluctuations, as $D_\perp \sim L_c^2/\tau_c$. This expression is particularly convenient as such an estimate can be provided by a statistical analysis of fluctuations diagnostics measurements. In particular, when turbulent fluctuations are caused by low frequency drift waves, having a time scale of the order of the inverse of the drift frequency $\tau_c \sim (\omega^{*i,e})^{-1}$ and a spatial scale of the order of a Larmor radius, $L_c \sim \rho_{i,e}$, the transport coefficient is described by the so-called gyro-Bohm scaling, $D_\perp \sim (\rho_{i,e}/L_T)T/eB$ [4, 5], with L_T the temperature gradient scale length. In the case of turbulent fluctuations of the order of the macroscopic size of the plasma, the transport has the conventional Bohm scaling, $D_\perp \sim T/eB$.

1.4 Plasma instabilities and turbulence

The plasma density and temperature in a tokamak vary by several orders of magnitude between the core and the SOL regions, the strong gradients acting as free energy reservoirs for instabilities to develop.
Tokamak plasmas exhibit a wide range of instabilities, which may be cast in two main classes: slow large scale MHD instabilities and micro-instabilities. Turbulent transport in a tokamak plasma is mainly produced by micro-scale drift-type turbulence, which is driven by local gradients of temperature or density.
Electrostatic plasma turbulence in tokamak can be understood as followed. First, charge separations occurs and creates electric fields. The $E \times B$ convection due to the turbulent electric field displaces plasma elements along the electric potential contours across the magnetic field. Once a phase difference between the potential and density perturbations is established, this process largely determines the radial particle and heat loss in a high temperature plasma.
In the following subsections we will not discuss MHD modes, but we will focus on the micro-instabilities leading to microturbulence, given that this thesis study focuses on the anomalous transport. Basics of plasma turbulence and transport theory are exposed in the lectures of Y. Sarazin [2]. A complete review of plasma turbulence theory can be found in the recent book of W. Horton [6]. A review of the turbulence measurements in tokamak is given in [7] whereas the turbulence diagnostics are reviewed in [8].

1.4.1 Drift-wave instability

Drift-waves are the most basic plasma instabilities. Drift-waves can develop in a slab plasma with an homogeneous magnetic field, at the sufficient condition that a density gradient exists and that the density perturbations have finite wave numbers in both the parallel and perpendicular directions. As the particles move very rapidly along the field line, the following inequality holds $k_\perp >> k_\parallel \neq 0$. The drift-wave mechanism in slab geometry is illustrated in Fig. 1.4 and described below. Initial perturbations of the

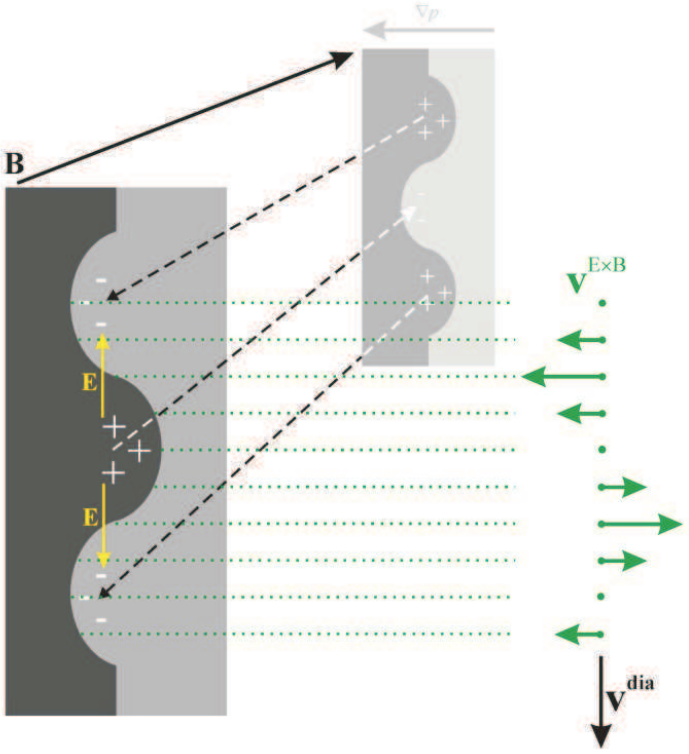

FIGURE 1.4: Schematics of drift-waves in slab geometry. Reproduced from [9].

density gradient are indicated by dark and light regions in fore- and background of the figure. Because of their low inertia, electrons are supposed to react rapidly on parallel density perturbations (dashed arrows parallel to the magnetic field in the figure). As a result, positively and negatively charged regions build-up in high and low density regions, respectively. Vertical[3] electric fields and the resulting $E \times B$ drifts are represented as vertical and horizontal arrows, respectively. In the case of adiabatic electrons, those instantaneously respond to the potential fluctuations, the density perturbation does not grow but propagates in the vertical direction at v^{dia}, the diamagnetic velocity. If the electron are non-adiabatic, a time lag between density and potential perturbations appears. If the phase shift between density and potential fluctuations is negative, i.e. $\varphi_n - \varphi_\phi < 0$,

[3] At the tokamak midplane, the *vertical* direction corresponds approximately to the poloidal direction.

the initial density perturbation grows and becomes unstable. Oppositely, if the phase-shift is positive, the resulting $E \times B$ will stabilize the perturbation. This simple picture allows us to estimate the typical frequencies of drift-waves turbulence

$$\begin{aligned} w_{dw} &\approx w_{*e} \equiv k_\perp v^{dia} \\ w_{dw} &\approx \rho_s c_s k_\perp / L_n, \end{aligned} \tag{1.7}$$

where w_{*e} is the electron diamagnetic frequency, c_s and L_n are the sound speed and the density gradient scale length, respectively. Note that the drift-waves frequency depends on $k_\perp$, which is related to the scale of the perturbation across the magnetic field.

1.4.2 Interchange instability

One of the possible underlying mechanisms for plasma turbulence, are micro-instabilities which belong to the pressure-driven family of interchange modes. In a tokamak, as depicted in Fig. 1.1 the magnetic field decreases with the major radius, inducing a magnetic field gradient. The magnetic field gradient leads to the interchange instabilities, which can develop even if $k_\parallel = 0$. Consequently, those instabilities are often considered as bidimensional. The interchange instability is the analog of the Rayleigh-Taylor instability for neutral fluids [10]. A Rayleigh-Taylor instability occurs when a heavy fluid is on top of a lighter fluid. If the layer between the two fluids is perturbed, the fluids will interchange their positions. In a tokamak, an interchange mode is unstable when the gradient of the magnetic field is aligned with the equilibrium pressure gradient. In this case the exchange of two flux tubes around a field line releases free energy. The interchange mechanism can either stabilize or destabilize an initial density perturbation depending the respective directions of the magnetic gradient ∇B and the pressure gradient ∇P. The basics of the interchange mechanism is depicted on Fig. 1.5. On the high field side of the tokamak, *good* curvature region, the plasma ∇B and ∇P point into opposites directions, a density perturbation makes the ions and electrons move downward and upward, respectively. The resulting $E \times B$ drift stabilizes the initial density perturbation. When ∇B and ∇P are aligned and point in the same direction, e.g. on the low field side, the $E \times B$, ∇B and curvature drifts combine to destabilise the density convective cells and an outwards instability appears. Also, since the trapped particles are localised on the low field side -which corresponds to the zone of minimum field along the field lines- these are expected to play a prominent role in the interchange process. Note that the frequency of the interchange instabilities is also of the order of the diamagnetic frequency.

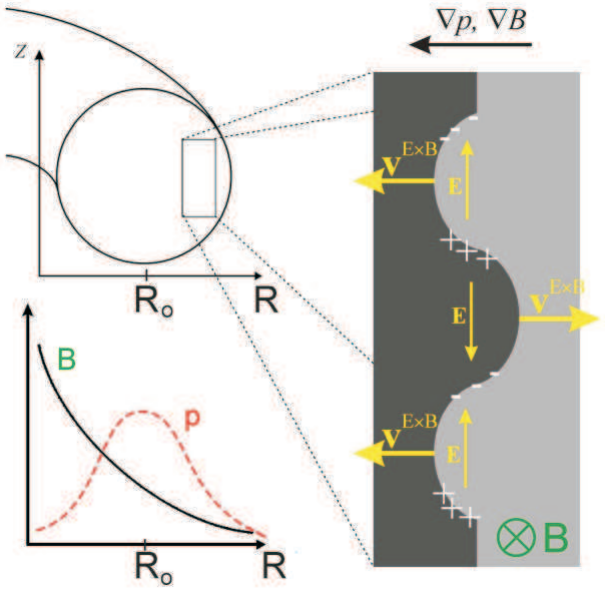

FIGURE 1.5: Interchange instability in the *bad* curvature region. The upper left plot depicts a section of a torus. The pressure and the magnetic field are maximum on the torus axis and at the symmetry axis, respectively, as depicted in the lower left plot. The right scheme illustrates the interchange instability. The magnetic field is perpendicular and points into the plane of the figure. On the low field side of the torus, ∇B and ∇p point in the same direction. Assuming an initial density perturbation (marked by dark and light regions), the curvature drift leads to a charge separation which causes an $E \times B$ drift. The resulting $E \times B$ drift amplifies the initial density perturbation. Reproduced from [9].

1.4.3 Core plasma instabilities

The main core plasma instabilities in a tokamak, belonging to the family of drift-waves, are the electrostatic ITG and the shorter wavelength electron-scale, ETG, respectively driven by ion or electron temperature gradients. The latter only includes the passing electrons whereas the former includes both trapped and passing particles. ITG and ETG instabilities have critical thresholds in temperature gradient and are also referred to $\eta_{i,e}$ modes, where $\eta_{i,e} = |L_n/L_{T_{i,e}}|$ denotes the ratio of the density scale length to that of the ion (electron) temperature. The ITG is generally the main instability responsible for ion heat transport in the plasma core. Correspondingly, ETG modes may produce large electron heat flux, on the electron scale.

Trapped electrons can contribute to the drive of ITG modes, enhancing the ITG growth rate [11, 12] , but they may also be the source of trapped electron modes (TEMs) [13]. TEMs are driven by density gradients in the presence of magnetic curvature and can cause electron particle transport as well as turbulent electron heat flux -depending on the local plasma parameters and collisionality- on the ion scale.
In the collisional plasma edge, a range of fluid instabilities (*ballooning modes*) which

we will not further investigate here, are driven by gradients in pressure, resistivity and current.
ITG, TEM and ETG are characterised by different spatial scales, as summarized in Fig. 1.6.

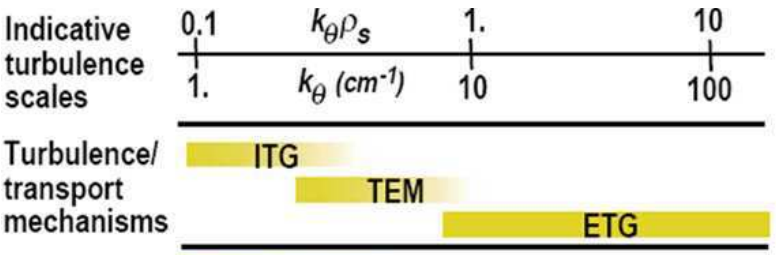

FIGURE 1.6: Spatial scales of ITG, TEM and ETG turbulence. Reproduced from [14].

Linear analytical predictions as well as numerical simulations show that the poloidal spectra of ITG peaks at $k_\theta\rho_s \approx 0.3-0.4$ [15] and that of TEMs $k_\theta\rho_s \approx 0.2$ [16], whereas the ETG spectrum peaks at higher values $k_\theta\rho_s \approx 5$ [17].
For typical parameters of Tore Supra core plasmas (e.g. $T_e \approx 1keV$, $B = 3$ T and $L_n = a = 72$ cm), we can estimate that ITG and TEM characteristic frequencies are in the range 30-60 kHz and their spatial scales are about 1-2 centimeters, whereas ETG have higher frequency 300 kHz and a scale of about 0.1 millimeters.

1.4.4 SOL turbulence

Large scales and long lived propagating density structures are observed in the SOL of nearly all plasma devices. Often referred to as blobs, these structures are though to originate from interchange instabilities in toroidal devices [18] and can contribute up to 50 % of the particle transport in the SOL region [19]. A theoretical review of blob turbulence is given in [20] whereas a complete review of the comparison of blob theory and experiment can be found in [21].

In order to get some insight in the phenomenology of blobs, a simple blob model, originally developed in [22], is presented here and illustrated in Fig. 1.7. Assuming an initial density perturbation elongated along the parallel direction and connected to the walls, the ∇B drift causes a polarization of the density perturbation. The polarization is a key element for the blob dynamics because it gives rise to an $E\times B$ velocity which advects the blob through the SOL. This polarization is mitigated by the current flowing in the parallel direction. Consequently, the blob dynamics is also greatly dependent on the choice of the current closure scheme. In this model, the *sheath-connected* boundary condition

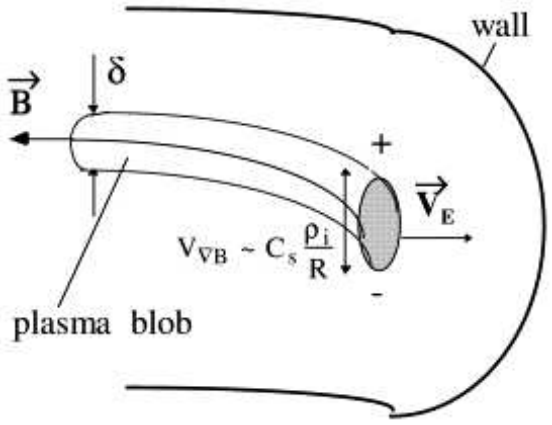

FIGURE 1.7: Schematics of a plasma blob. Due to the polarization, the $\mathbf{E} \times \mathbf{B}$ drift causes the blob to propagate radially outward. Reproduced from [22].

is used, $J_{\parallel}|_{wall} = ne^2 c_s \Phi / T_e$. If we consider a plasma at constant temperature and a Gaussian shaped blob $n_b(x, y) = n_b(x) exp(-y^2/(2\delta^2))$ which does not interact with the background plasma, then the blob is convected without deformation at the velocity

$$v_x = c_s (L_{\parallel}/R)(\rho_s/\delta)^2. \tag{1.8}$$

Here, x and y denote the radial and poloidal coordinates, respectively. $L_{\parallel}$, R and δ are the parallel connection length, the major radius and the characteristic blob size.

The blob lifetime t_b is mainly limited by the parallel loss of particles along the field lines, consequently the blob lifetime is of the order of $t_{\parallel} = L_{\parallel}/c_s$. On this time scale, the blob travels a distance $\Delta x \approx v_x t_{\parallel}$. Substituting v_x in Eq. 1.8 we find that $\delta^2 = L_{\parallel}^2 \rho_s^2 / R \Delta_x$.

Using typical parameters of Tore Supra SOL ($L_{\parallel} \approx 30$ m, $T_e = 10$ eV $B = 2.5 T$), we can now estimate the blob time scale $t_b \approx 1$ ms and, using $\Delta x = 0.1$ m (the typical width of Tore Supra SOL), the blob characteristic size $\delta \sim 1$ cm.

Analytical models often consider blobs as isolated structures which propagate without interacting in a homogeneous background plasma. Experimentally, the existence of temperature and density gradients in the SOL region breaks the assumption of homogeneity. Consequently, these ideal models may help to qualitatively explain the blobs properties but might be to simplistic to be compared to the experimental measurements, as discussed in Sec. 7.2.3. As an alternative, numerical simulations with SOL turbulence codes can be used for the interpretation of the SOL turbulence data. An attempt is presented in Sec. 7.2.4.

1.5 Scope of the thesis and outline

As outlined through the previous sections, anomalous transport of heat and particles in a tokamak plasma is at present believed to be induced by turbulence, driven by micro-instabilities. As a consequence, the understanding and control of turbulence is critical for the performance of a fusion reactor. A description of turbulence phenomena in a tokamak, based on first-principle physics is unfortunately still lacking, given the complexity of both the topology and physics into play in such a system. Therefore measurements of turbulence in a tokamak are an essential, though challenging, task.
Turbulence diagnostics should on the one hand, be able to operate in a hot and magnetised medium, and on the other, provide sufficient resolution to probe turbulence scales, possibly on a large extent of the poloidal section of the tokamak. Very few diagnostics meet these specifications. Perturbing techniques such as electrostatic probes are restricted to low temperature plasma regions such as the outer edge or the SOL. Core turbulence can be studied with imaging systems such as the beam electron spectroscopy (BES).

Microwave diagnostics such as reflectometer systems can also be used to investigate plasma turbulence. Traditionally, fixed-frequency correlation reflectometers were used to determine the turbulence properties. In this work, we used an alternative sweeping frequency reflectometer system. One of the great advantages of the sweeping systems is their ability to provide continuous measurements of the plasma density and its fluctuations from the very far SOL to the tokamak core.
It will be shown in Sec. 2.3.2 that the sweeping system has a spatial resolution which is sufficient to both resolve the spatial scales corresponding to the blobby turbulence ($\sim$ 1 cm, Sec. 1.4.4) but also the ITG and TEM turbulence ($\sim$ 1-2 cm, Sec 1.4.3).
From its beginnings [23–25], the frequency sweeping reflectometry had to deal with plasma turbulence which was scrambling the reflected signal, thus preventing from a correct electron density profile reconstruction. This issue was actually overcome on the sweeping reflectometer operating on Tore Supra [26], by decreasing the sweeping time from the millisecond to the microsecond range and by using the heterodyne detection technique. Thanks to these technical enhancements, the improved quality of the signal allowed to study the close relationship between the density fluctuations and the signal fluctuations. MHD activity, micro-turbulence profiles, and wavenumber spectra were thus determined (PhD thesis L. Vermare [27] and T. Gerbaud [28]). The sweeping reflectometer was upgraded in 2008 and is now able to follow the evolution of the density fluctuations at a rate of 333 kHz, being consequently ascribed as an *ultrafast* sweeping technique. The time resolution of the reflectometer system is now below the estimated time scale of the turbulent fluctuations both in the SOL ($\sim$ 1 ms, Sec. 1.4.4) and in the

core plasma ($\sim 15 - 30\,\mu s$, Sec. 1.4.3). This upgrade should thus open the possibility of investigating the dynamical properties of the turbulent fluctuations.

The main goal of this work is indeed to provide original measurements of the turbulent fluctuations by taking advantages of the possibilities offered by the ultrafast sweeping reflectometer. To achieve this, our work plan was divided in three steps.
First, as ultrafast sweeping reflectometry is a new method, its capability to measure turbulence was investigated. Then, statistical analysis methods were developed and applied to the reflected signals in order to quantify the turbulence properties in Tore Supra discharges. In particular, the radial and temporal characteristics of the turbulent fluctuations have been analysed. Finally, parametric dependencies of the turbulence properties have been investigated.
To support the reporting of these activities, the present manuscript is divided as follows.

- In Chapter 2 , Tore Supra tokamak is introduced as well as the diagnostics used in this work. A special emphasis is given to the description of the ultrafast sweeping reflectometer.

- Chapter 3 presents the basic physics of plasma-wave interactions, relevant to reflectometry, which is indeed a radar technique based on the propagation of an electromagnetic wave in a magnetized plasma.

- Chapter 4 details how density fluctuations can be recovered from the density profile reconstruction with the Bottollier-Curtet recursive algorithm in WKB approximation. Capabilities and issues are there highlighted.

- In Chapter 5, measurements of electron density fluctuations from the ultrafast sweeping reflectometer are compared to those from a Langmuir probe in the SOL.

- In Chapter 6, statistical analysis of the raw reflectometer signals is used to characterize the turbulence properties in ohmic plasmas.

- In Chapter 7, the parametric dependences of the turbulence properties with respect to the average electron density and the plasma current are investigated.
- Last but not least, the effects of the ion cyclotron frequency heating on the turbulence properties are discussed in detail in Chapter 8.

- Conclusion and perspectives are finally given in Chapter 9.

Chapter 2

Experimental setup

In this chapter, the experimental setup is presented. The Tore Supra tokamak and its heating systems are briefly described in the first section. Then, the technical aspects of the ultrafast sweeping reflectometer are presented. During this work, other diagnostics such as fixed-frequency and Doppler reflectometry as well as Langmuir probes were used to support the sweeping reflectometer measurements. These diagnostics are also introduced here.

2.1 Tore Supra Tokamak

Tore Supra is a circular section limiter tokamak located in CEA, Cadarache, France. Tore Supra was designed to explore fusion technologies and physics under the conditions of long pulse discharges. Discharges lasting several minutes are possible thanks to superconductive toroidal field coils. Moreover, all the plasma facing components are actively cooled.

Tore Supra characteristics and the associated typical ohmic discharge values are listed in Tab. 2.1.

2.1.1 Heating systems

In Tore Supra, the plasma is heated by electromagnetic waves. As the plasma turbulence properties might be affected by the electromagnetic heating, the latter is of importance for this work. In order to transfer the energy from the wave to the plasma, the wave frequency is chosen such as to match a particle frequency. Three wave heatings systems,

Magnetic field on the axis, B_0	max. 3.8 T
Major radius, R	2.38 m
Minor radius, a	0.72 m
Mean electron density, $\langle n_e \rangle$	3×10^{19} m^{-3}
Density at the LCFS, n_e^{LCFS}	8×10^{18} m^{-3}
Density 5 cm outside the LCFS, n_e^{SOL}	1.9×10^{18} m^{-3}
SOL density gradient length, λ_{SOL}	3 cm
Plasma current, Ip	1 MA
Central electron temperature, T_{e0}	5 KeV
Central ion temperature, T_{i0}	2 KeV

TABLE 2.1: Tore Supra parameters.

operating at different frequencies, are available on Tore Supra. Although only one of those is of importance for this work, all are presented for the sake of completeness.

- **Electron cyclotron resonance heating**

  A 118 GHz electron cyclotron heating (ECRH) has been installed in 2004 [29]. It delivers 400 kW power in long pulse operations. The system is composed of 2 gyrotrons. When working at the nominal magnetic field ($B_0 = 3.8\,T$), the power is deposed in the central plasma. The system can also be used for current drive. Due to technical failure, the ECRH system was not available during the last experimental campaign. As a consequence, ECRH heated plasmas were not studied during this work.

- **Lower hybrid current drive**

  The Tore Supra 3.7 GHz lower hybrid current drive (LHCD) system was designed to inject 8 MW in long pulse operation [30]. Tore Supra LHCD is mainly used for current drive.

  During LH heating, suprathermal electrons are massively created and generate a relativistic downshift of the electron cyclotron frequency in the plasma center as well as its second harmonic. Thus non negligible emission of radiation coming from the core is detected by the reflectometer particularly close to the first cutoff[1] frequencies which can also increase substantially the noise over all the cutoff frequency range, particularly at low magnetic field. Because of its parasitic effects on the reflectometer signals, LH heated plasmas were not studied in this work.

- **Ion cyclotron resonance heating**

  The ion cyclotron resonant heating (ICRH) is the main auxiliary heating system on Tore Supra. The ICRH operates between 40 to 80 MHz. ICR waves can be

[1] The definition of the cutoff is given in Sec. 3.1.3.

launched from three different antennas. Each launcher can inject up to 4 MW power [31].

More details on the ICRH system are given in Sec. 8 where the turbulent properties in ICRH heated plasma are studied.

Fig. 2.1 shows a top view of Tore Supra. The locations of the different heating systems are shown.

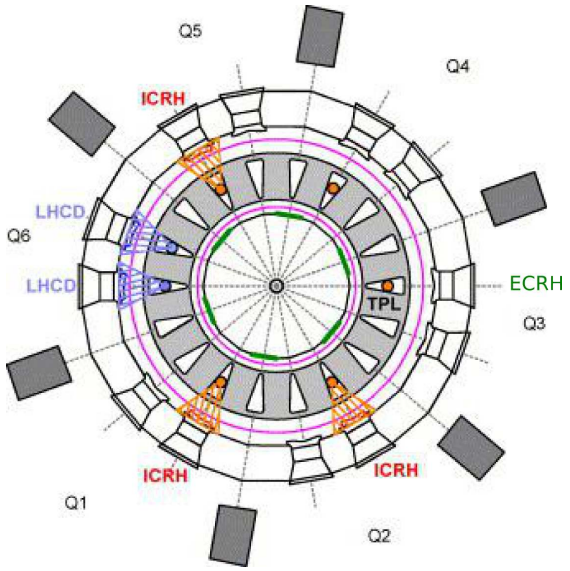

FIGURE 2.1: Top view of Tore Supra vacuum vessel. The locations of the heating systems are indicated.

2.2 Turbulence diagnostics in Tore Supra

Several diagnostics, as Langmuir probes, reflectometers and fast camera , provide turbulence activity measurements on Tore Supra. Diagnostics of the first two kinds are detailed below because they were used complementary to the ultrafast sweeping reflectometry.

When analyzing turbulent data obtained with several diagnostics, their localizations (Fig. 2.2) have to be taken into account because turbulence properties may vary due to spatial asymmetries. Due to the fast parallel transport, we expect small toroidal asymmetries whereas poloidal asymmetries might be more pronounced as discussed in Sec. 5.3.1.

2.2.1 Langmuir probes

Plasma quantities as density, floating potential and electron temperature can be obtained by the use of electrostatic probes called Langmuir probes. This diagnostic technique was

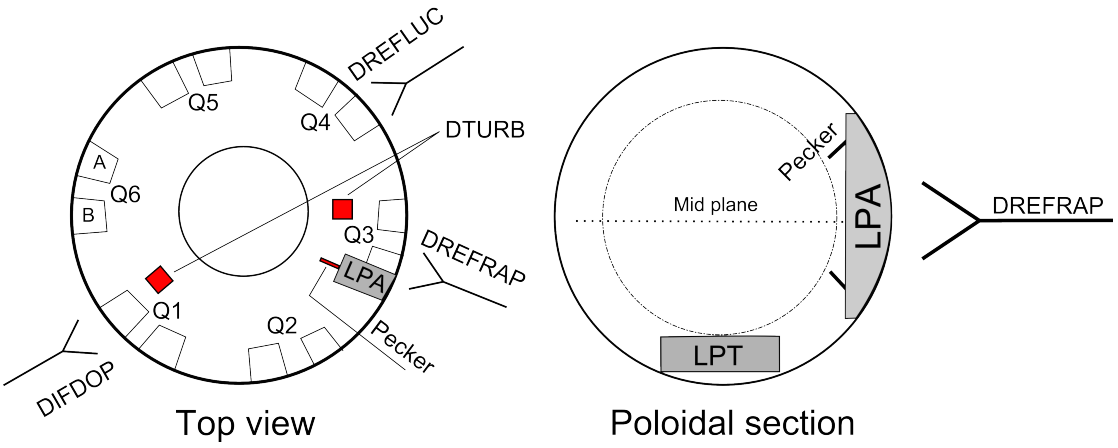

FIGURE 2.2: Left: top view of Tore Supra vacuum vessel. The reflectometers are located in the equatorial plane whereas the rake probes are located at the top of the device. The pecker probes are inserted in the antenna protection (LPA). Dturb and Pecker designate the rake and the reciprocating probes, respectively. Derefrap, Drefluc and Difdop designate the ultrafast sweeping, the fast hopping and the Doppler reflectometers, respectively. Right: poloidal view in front of the ultrafast sweeping reflectometer. LPT stands for the toroidal limiter.

developed ninety years ago by the Nobel prize winner I. Langmuir [32]. These probes are still intensively used today. They offer an excellent spatial and temporal resolution. Langmuir probes consist in a wire isolated from the plasma except for a small tip. They are mainly used in low-temperature and edge fusion plasmas because hot plasma would destroy the probe. Langmuir probes are an invasive technique and perturb the plasma locally. Langmuir probes measurements are performed by biasing the pin and measuring the collected current. The probe bias can be swept in order to measure the electron temperature. Fig. 2.3 illustrates a typical current-voltage (I-V) curve. Three distinct regions appear in the I-V curve. If the pin is sufficiently negatively biased , all electrons

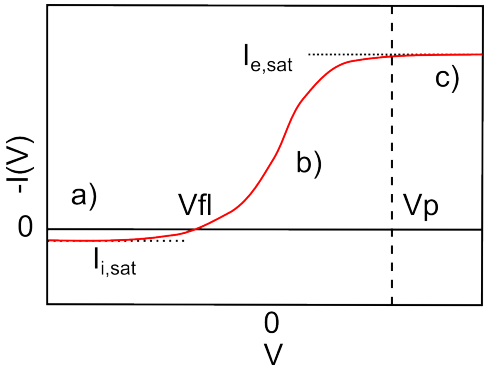

FIGURE 2.3: Langmuir probe I-V curve. The I-V curve is divided in three regions : ion-saturation current (a), transition region (b) and electron saturation range.

are repelled. There is a saturation of the captured ions, therefore the measured current is called ion-saturation current ($I_{i,sat}$). In opposite, if the pin is sufficiently positively

biased, only electrons are captured, this gives the electron-saturation current. In between, both electrons and ions are captured and contribute to the resulting current.

In a collisionless unmagnetized plasma with Maxwellian electrons and cold ions, $I_{i,sat}$ is expressed as:

$$I_{i,sat} = A_{coll}^{eff} e n_e \sqrt{\frac{ZT_e + T_i}{m_i}}, \tag{2.1}$$

with e the elementary charge, n_e the electron density, $T_{e,i}$ the electron and ion temperatures and m_i the ion mass. A_{coll}^{eff} is the effective collector area and depends mainly on the probe geometry. $I_{i,sat}$ fluctuations are usually used as proxy to monitor the density fluctuations under the assumption of small temperature fluctuations. This assumption is questionable given that significant electron temperature fluctuations have been reported in several devices [33–35]. We will address this issue in Sec. 5.3.5.

Now that the basic Langmuir probe principles have been reviewed, we can focus on the design of the Tore Supra probes.

The pecker probe .

The pecker probe is a tunnel probe system newly installed in the Tore Supra antenna protection (LPA) [36]. It consists of two probes located in the same equatorial port than the sweeping reflectometer Drefrap, 20° upward and downward the equatorial plane, respectively (Fig. 2.2) . The probe plunges into the plasma back and forth and explores a region extanding approximately from the LPA to the LCFS. The plunges, also referred to as probe reciprocations, last 10 ms.

Plasma measurements are performed through circular collectors placed on both sides of the probes. The probes are operated in I-V mode and can measure the electron temperature, the plasma density and the Mach number. Nonetheless, only $I_{i,sat}$ data are explicitly used here. Data obtained with the Pecker probes have been extensively compared to Drefrap data because of their spatial proximity which reduces the effects of eventual poloidal asymmetries. The probes were operating for the first time during Tore Supra 2011 experimental campaign. Unfortunately, the lower probes broke down after few discharges which restricted the analysis of the pecker probes data to those collected by the upper probe.

An example of the swept bias applied to the pecker probe is shown on Fig. 2.4 a). To extract the ion saturation current component, only the parts of the signal for which

the bias is below -50V[2]. Consequently, measurements of $I_{i,sat}$ are not available for each position during the probe reciprocation but are restricted to specific intervals. This can be seen on Fig. 2.4 b). The part of the signal for which the probe collectors were partially shadowed by the LPA has also been removed.

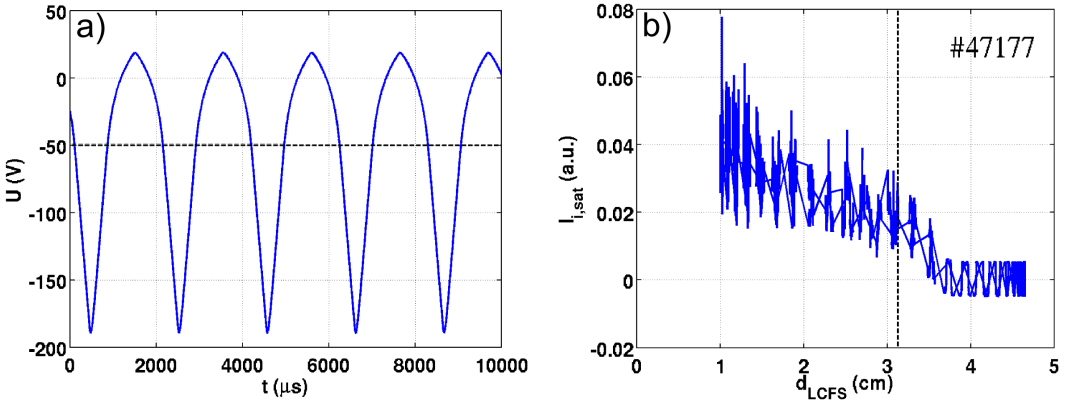

FIGURE 2.4: a) Bias applied to the pecker probe. The ion saturation regime is reached for potential below -50 V (the black dashed line). b) $I_{i,sat}$ measured by the pecker probe. Only the measurements inside the region limited by the black dashed line are meaningful.

2.2.2 Reflectometers

Reflectometry is radar technique aiming at scanning the plasma with electromagnetic waves. Several plasma parameters, such as the electron density, can be inferred from the characteristics of the probing waves.
The propagation of electromagnetic waves in a plasma is described in the next chapter. Here, we focus on the technical aspects of Tore Supra reflectometers.

- **Fast hopping reflectometer**

  The O-mode fast hopping reflectometer Drefluc operates in the D-band (105-150 GHz) installed on the equatorial port Q4A. Drefluc performs frequency sweeping as well; consequently it can also provide electron density profile measurements [38]. When working at fixed frequency, the data acquisition is set to 1 MHz leading to 1 μs time resolution. The system can perform 31 frequency plateaus, each lasting up to 8 ms, in a single plasma discharge. The excellent time resolution of the fast hopping reflectometer allows us to follow the time evolution of the turbulence. Moreover, Drefluc has a good signal to noise ratio and will be used to validate the

[2]This specific threshold value was not randomly chosen but results from a trade-off between the guarantee of operating in the ion saturation regime [37] and the maximization of the number of available data points.

temporal measurements performed with the ultrafast sweeping reflectometer (see Sec. 6.2.3).

- **Doppler reflectometry**

  Doppler reflectometry is based on backscattering rather than reflection at a well defined plasma layer. The Doppler reflectometer Difdop is installed in the equatorial port Q1A. Difdop can be either used in O-mode polarization in the V-band (50-75 GHz) or in X-mode polarization in the W-band (75-110 GHz). In term of plasma accessibility, the plasma is probed from $r/a = 0.5$ to $r/a = 0.9$ for the O-mode and from $r/a = 0.85$ to $r/a \geq 1$ for the X-mode. The probing beam is launched with a poloidal angle which can vary from -1 to 10°. The data are acquired at 10 MHz. More details are given in [39].

  Among other quantities, the perpendicular fluctuations velocities $V_\perp$ can be estimated from Doppler reflectometry measurements. $V_\perp$ is determined from the Doppler shift $w_d = k_\perp V_\perp$ of the Doppler spectrum. The perpendicular wavenumber $k_\perp$ is obtained using ray tracing calculations. Both the toroidal and poloidal velocities contribute to the perpendicular velocity. However, due to the small tilt angle of the magnetic field line $\alpha \approx r/qR << 1$, the perpendicular velocity is dominated by the poloidal velocity (Fig . 2.5).

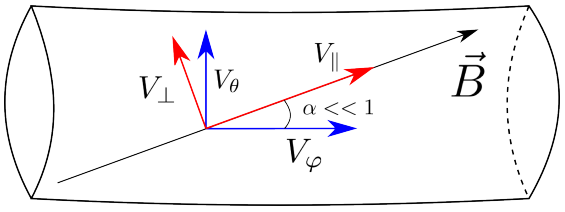

FIGURE 2.5: Schematic of a field line lying on a flux surface. The velocities in the laboratory frame (V_θ and V_φ) and in the plasma frame ($V_\perp$ and $V_\parallel$) are represented .

Now that the auxiliary turbulence diagnostics have been briefly described, a detailed description of Drefrap, the ultrafast sweeping reflectometer, is presented in the next section.

2.3 Tore Supra ultrafast sweeping reflectometer

Drefrap is an X-mode heterodyne ultrafast sweeping reflectometer installed in Tore Supra Q3A equatorial port right next to the antenna protection (see Fig. 2.2 and Fig. 2.6). Drefrap operates in V- (50-75 GHz) and W-band (75-110 GHz) frequency range.

FIGURE 2.6: Left: outside view of the tokamak. The reflectometer is marked with a blue ellipse. Right: equatorial port shared by the reflectometer and the LPA.

An extensive description of the diagnostic can be found in [40]. Thanks to a recent upgrade [41], the sweeping time is as low as 2 μs which makes Drefrap the world's fastest sweeping reflectometer.

2.3.1 Design of the ultrafast sweeping reflectometer

Fig. 2.7 shows the schematic of the set-up.

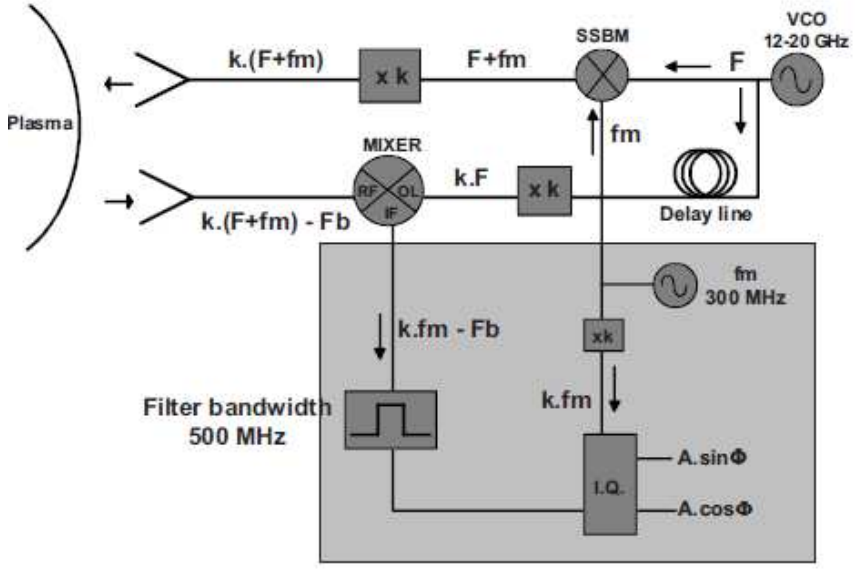

FIGURE 2.7: Schematic of Drefrap with k=4 and 6 for the V and W bands, respectively. Reproduced from [41].

The frequency ramp (12-20 GHz) is generated by a voltage controlled oscillator (VCO). Then the signal is separated in two branches, namely the plasma signal and the reference signal. The single side band modulator (SSBM) adds a modulation frequency f_m to the

main frequency F. The SSBM is a key component for the heterodyne system because it shifts the signal frequency to a frequency band where the mixer signal to noise ratio is higher [42]. Before being launched to the plasma, the frequency is multiplied to reach the required probing frequency. After the round trip in the plasma, the wave comes back and is measured by the receiving antenna. The propagation of the wave into the plasma has introduced a frequency shift corresponding to the beat frequency. The beat frequency is of interest because it is proportional to the time of flight of the probing wave. The reference signal, which has been delayed to compensate the propagation of the probing wave into the wave guides, is mixed to the probing signal. Finally, the modulation frequency is removed and an I/Q detector is used to separate the in-phase and 90° phase components of the signal. This separation is required to measure the amplitude and phase of the reflected signal independently. The reflectometer signal is acquired by a 4 channels module (10 bit digitization, 32 Mb/channel) having a sampling frequency of 2 GHz/sample.

2.3.2 Recorded signal

A significant advantage of sweeping reflectometry is the ability to perform successive frequency ramps. Each frequency ramp lasts 2 μs and 1 μs dead time is required to initialize the frequency between two ramps. The recorded signal is expressed as

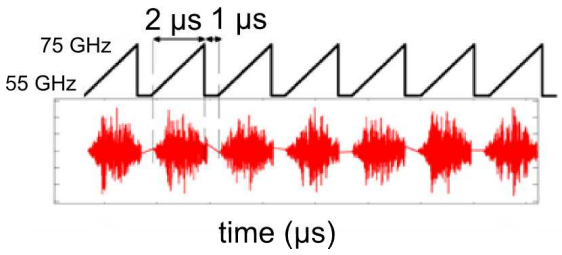

FIGURE 2.8: Example of a signal recorded by the V band reflectometer during successive frequency ramps. Both V and W bands are swept simultaneously.

$$S(F,t) = A(F,t)e^{i\phi(F,t)}, \tag{2.2}$$

with A and ϕ the signal amplitude and phase, respectively. In practice data are stored in m-by-n matrices with $1 \leq i \leq m$ stands for the frequency index and $1 \leq j \leq n$ stands for the time index. Generally $m = 2000$ which leads to a relative submillimetric spatial resolution (reminding that the probing frequency is linked to the radial position). The acquisition system can record up to 10000 sweeps per shot. Fig. 2.8 shows an example of the recorded signals during a burst of frequency ramp.

Chapter 3

Propagation of electromagnetic waves in a plasma

In this chapter, the basic properties of electromagnetic waves in plasma are reviewed. First, the dispersion relation is derived in the case of an homogeneous magnetized plasma. The dispersion relation reveals two particularly important polarization modes for fusion studies, the O and X mode. The experimental results reported in this manuscript were obtained using X-mode, thus more attention is paid to this polarization.
In the second part, the expression of the wave electric field is given for a spatially varying plasma. Finally, the effects of electronic density fluctuations on the electromagnetic wave propagation is addressed, which is a key issue for this PhD work.

3.1 Propagation in a homogeneous plasma

The expressions presented in this section are based on the early work of Ginzburg [43]. Here, we restrict our analysis to the case of monochromatic plane waves $\vec{E}_0 e^{i(wt-\vec{k}\vec{r})}$, where w and $\vec{k}$ denote the frequency and the wave vector, respectively. The fundamental equations which rule the behavior of electromagnetic fields in plasmas are the Maxwell equations in continuous medium. We consider Maxwell equations coupled to the electron motion equation in absence of external magnetization

$$\vec{\nabla} \times \vec{\nabla} \times \vec{E} + \mu_0 \frac{\partial}{\partial t} \vec{j} + \frac{1}{c^2} \frac{\partial^2}{\partial t^2} \vec{E} = \vec{0}, \tag{3.1}$$

and Ohm's law

$$\vec{j} = \bar{\sigma}\vec{E}, \tag{3.2}$$

where $\bar{\sigma}$ is the conductivity tensor which describes the plasma properties. An expression of the conductivity tensor can be obtained under the following assumptions,

- **Stationarity**

  The plasma time scales are significantly longer than the period of the probing wave. Thus, the plasma is considered to be stationary during a wave period.

- **Cold plasma**

  The probing wave phase velocity is of the order of the speed of light, the particle thermal velocity is therefore assumed to be small with respect to the phase velocity. It results that the electron motion is due to the probing wave fields at the leading order [44] .

- **High frequencies**

  The ion and neutral particles are considered at rest because of their large inertia. This assumption is fully justified as far as the probing wave frequency is well above the ion characteristic frequencies, which is the case for reflectometry in a tokamak. Only the electrons will contribute to the conductivity tensor.

- **Linearity**

  Eq. 3.1 is linear at first order, meaning that any linear combination of monochromatic propagating waves is a solution. This assumption can be applied since the launched power is very low.

3.1.1 Dispersion relation

The propagation of waves in a plasma is completely described by the dispersion relation $w(k)$ which links the frequency to the wave vector. The dispersion relation contains information on the reflection points, which play a major role in reflectometry. Under the previous assumptions, Eq. 3.1 can be rewritten as

$$\vec{k} \times \vec{k} \times \vec{E} + \frac{w^2}{c^2}\left(\bar{I} + \frac{i}{w\epsilon_0}\bar{\sigma}\right)\vec{E} = 0. \tag{3.3}$$

The conductivity tensor is expressed along directions which are parallel ($\parallel$) and perpendicular ($\perp$) to the magnetic field $\vec{B}_0$ [45]

$$\bar{\sigma} = \epsilon_0 w \begin{pmatrix} -\frac{w_{pe}^2}{w^2-w_{ce}^2} & -i\frac{w_{ce}}{w}\frac{w_{pe}^2}{w^2-w_{ce}^2} & 0 \\ i\frac{w_{ce}}{w}\frac{w_{pe}^2}{w^2-w_{ce}^2} & -\frac{w_{pe}^2}{w^2-w_{ce}^2} & 0 \\ 0 & 0 & -\frac{w_{pe}^2}{w^2} \end{pmatrix} \begin{matrix} (\perp) \\ (\perp) \\ (\parallel) \end{matrix} . \tag{3.4}$$

The conductivity depends on the plasma density and magnetic field through the plasma electron $w_{pe} = \sqrt{n_e^2 e^2/\epsilon_0 m_e}$ and cyclotron frequency $w_{ce} = eB/m_e$, respectively.

The perpendicular propagation is mainly relevant for reflectometry studies ($\vec{k} \perp \vec{B}$); taking $\vec{B}_0 = B_0 \vec{e}_z$, Eq. 3.3 reads

$$\begin{pmatrix} 1-\frac{w_{pe}^2}{w^2-w_{ce}^2} & i\frac{w_{ce}}{w}\frac{w_{pe}^2}{w^2-w_{ce}^2} & 0 \\ -i\frac{w_{ce}}{w}\frac{w_{pe}^2}{w^2-w_{ce}^2} & 1-\frac{w_{pe}^2}{w^2-w_{ce}^2}-N^2 & 0 \\ 0 & 0 & 1-\frac{w_{pe}^2}{w^2}-N^2 \end{pmatrix} \begin{pmatrix} E_x \\ E_y \\ E_z \end{pmatrix} = 0. \tag{3.5}$$

$N = ck/w$ is the wave index of refraction. Eq. 3.5 is a linear system which has non trivial solutions only if the determinant is zero. This leads to the dispersion relation

$$D(w, N) = (\epsilon_3 - N^2)(\epsilon_1^2 - N^2\epsilon_1 - \epsilon_2^2) = 0, \tag{3.6}$$

with ϵ_i defined as

$$\epsilon_1 = 1 - \frac{w_{pe}^2}{w^2 - w_{ce}^2} \tag{3.7}$$

$$\epsilon_2 = \frac{w_{ce}}{w}\frac{w_{pe}^2}{w^2 - w_{ce}^2} \tag{3.8}$$

$$\epsilon_3 = 1 - \frac{w_{pe}^2}{w^2} \tag{3.9}$$

This equation has several solutions which correspond to different polarization modes.

3.1.2 Polarization modes

Ordinary mode

The ordinary mode (O-mode) refractive index is obtained from $\epsilon_3 - N^2 = 0$, which gives

$$N_O^2 = 1 - \frac{w_{pe}^2}{w^2}. \tag{3.10}$$

The last expression shows that O-mode waves propagate independently of the magnetic field. This results from the collinearity of the wave electric field and the magnetic field (Fig. 3.1). Due to simple expression of the refractive index, most of analytical results were obtained for O-mode reflectometry. Unfortunately, O-mode waves have limited plasma accessibility in the edge of tokamak plasmas [46].

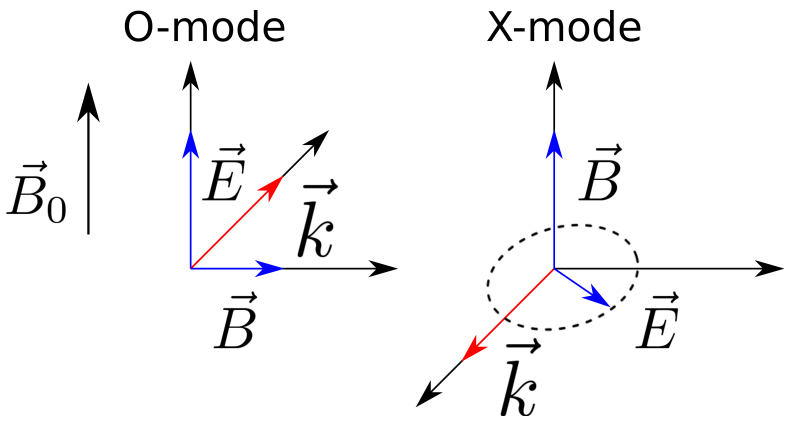

FIGURE 3.1: O- and X-mode polarization.

Extraordinary mode

The reflectometer used during this PhD work operates in the upper branch of extraordinary mode (X-mode), therefore more attention will be paid to X-mode wave properties. In this case, the wave electric field is perpendicular to the magnetic field (Fig. 3.1). N_X is obtained by looking for the second solution of Eq. 3.6,

$$N_X = 1 - \frac{w_{pe}^2}{w^2} \frac{w^2 - w_{pe}^2}{w^2 - w_{pe}^2 - w_{ce}^2}. \tag{3.11}$$

Contrary to the O-mode, the X-mode refractive index depends on both electron density and magnetic field.

3.1.3 Resonance and cutoff

Specific plasma regions exist and are of primary importance for wave propagation in a plasma. These regions are defined with respect to the local refractive index values.

- **Propagation in vacuum :** $N_X \to 1$

  If the wave frequency is much larger than the local plasma and electron cyclotron frequency, then the wave does not *feel* the plasma and propagates freely as in vacuum.

- **cutoff :** $N_X = 0$

  The waves propagate in the plasma for $k^2 > 0$ and are evanescent for $k^2 < 0$. The plasma layer which separates these two regimes is called the cutoff layer. The cutoff layer is the turning point of the probing wave. In X-mode, two frequencies satisfy $N_X = 0$

$$w_{XL} = \frac{1}{2}\left(\sqrt{w_{ce}^2 + 4w_{pe}^2} - w_{ce}\right) \tag{3.12}$$

$$w_{XH} = \frac{1}{2}\left(\sqrt{w_{ce}^2 + 4w_{pe}^2} + w_{ce}\right). \tag{3.13}$$

  These frequencies are called lower and upper cutoff frequencies, respectively.

- **Resonance :** $N_X \to \infty$

  For $w = \sqrt{w_{pe}^2 + w_{ce}^2}$, the wave energy is transferred to the plasma. For reflectometry studies, the resonant frequencies should be avoided. This is done by working with frequencies in the range of the upper cutoff frequency.

The values of the electron plasma, electron cyclotron, lower and upper cutoff frequencies with respect to the radial position are shown in Fig. 3.2 for a central magnetic field B_0=2.8 T and a central density $n_{e0} = 3 \times 10^{19}\, m^{-3}$.

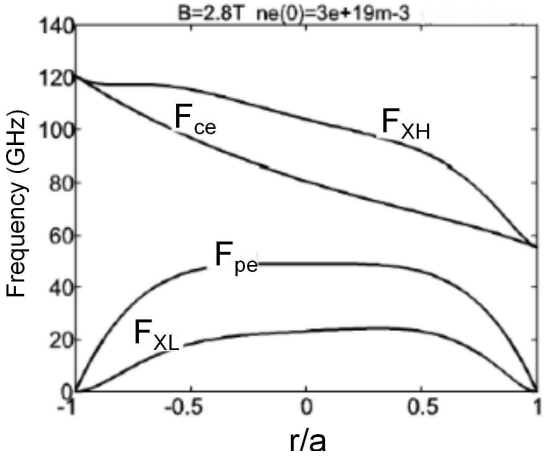

FIGURE 3.2: Values of the electron plasma (F_{pe}), electron cyclotron (F_{ce}), lower (F_{XL}) and upper (F_{XH}) cutoff frequencies with respect to the radial position computed at B=2.8 T and $n_{e0} = 3 \times 10^{19}\, m^{-3}$. Adapted from [27].

3.2 Propagation in a spatially varying plasma

Strong density gradients are present in tokamak plasmas. The plasma core density differs by at least 3 orders of magnitude from the density close to the wall. This radial dependence should be taken into account in order to derive a reflectometry theory relevant to tokamak plasmas. To this end, we consider a stationary plasma with density varying only along the radial direction. In this case, the evolution of the wave electric field is described by the 1-D Helmholtz equation

$$\left(\frac{d^2}{dr^2} - k^2(r)\right) E(r) = 0. \tag{3.14}$$

$k(r)$ is the local wave number and is linked to the vacuum wave number by the relation $k(r) = k_0 N(r)$. Eq. 3.14 can be solved analytically if the medium varies slowly with respect to the wave length. This assumption is referred to as the WKB approximation. Under this assumption, the solutions should have locally the same form as the solutions in homogeneous medium

$$E(r) = E_0(r) e^{i\phi(r)} \tag{3.15}$$

Eq. 3.14 is rewritten as

$$\frac{d^2E_0}{dr^2} + iE_0\frac{d^2\phi}{dr^2} + 2i\frac{dE_0}{dr}\frac{d\phi}{dr} + E_0\left(k^2 - \left(\frac{d\phi}{dr}\right)^2\right) = 0. \tag{3.16}$$

The electric field amplitude is assumed to vary slowly with respect to the phase. The second order derivative of the electric field can thus be neglected. In this case, Eq. 3.16 vanishes when the real and imaginary part vanish. The solution of $k^2 - \left(\frac{d\phi}{dr}\right)^2 = 0$ gives the phase

$$\phi(r) = \pm \int_{-\infty}^{r} k(r')dr'. \tag{3.17}$$

Solving

$$E_0\frac{d^2\phi}{dr^2} + 2\frac{dE_0}{dr}\frac{d\phi}{dr} = 0, \tag{3.18}$$

gives the electric field amplitude $E_0(r) = \frac{A}{\sqrt{d\phi/dr}}$, where A is an integration constant.

Finally, the solution of Eq. 3.14 takes the form

$$E(r) = \frac{A}{\sqrt{k(r)}} e^{\pm i k_0 \int_{-\infty}^{r} N(r')dr'}. \tag{3.19}$$

This solution is valid far from the cutoff where the medium varies slowly.

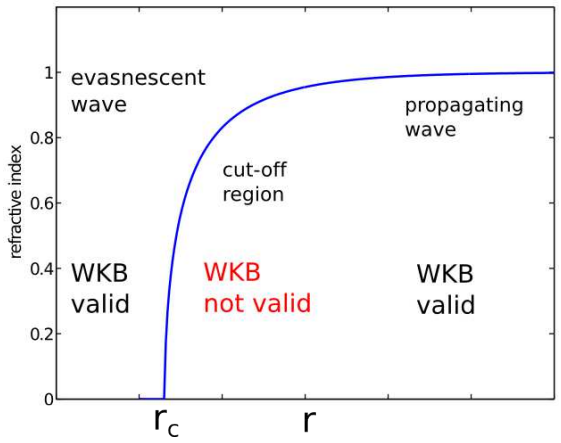

FIGURE 3.3: Typical behavior of X-mode refractive index. Far from the cutoff, WKB approximation is valid and propagating waves are solutions of the Helmholtz equation. In the vicinity of the cutoff, the refractive index varies rapidly and WKB approximation breaks down. Behind the cutoff, WKB approximation is again valid and waves are evanescent.

Eq. 3.19 shows that the electric field is enhanced when the wave approaches the cutoff region. Therefore, most of plasma wave interactions take place in the surroundings of the cutoff layer which ensures that reflectometry measurements are well localized spatially [47].

The phase term plays a role of primary importance for the density profile reconstruction. Phase effects which arise at the cutoff layer have to be taken into account. To this end, it is sufficient to impose continuity between the propagating and evanescent waves. This procedure is described in details in [48]. The resulting phase is expressed as

$$\phi(r_c) = 2 \int_{-\infty}^{r_c} k(r')dr' - \pi/2. \tag{3.20}$$

r_c denotes the cutoff layer position. This expression is nothing but the WKB expression with an additive term. This new term accounts for the non "mirror-like" reflection of the wave on the cutoff layer. This expression is valid as long as the wavelength is shorter or equal to the density gradient scale length [49].

3.3 Propagation in a turbulent plasma

Besides of anisotropy, a tokamak plasma is a highly turbulent medium. Up to now, the effects of density fluctuations on the probing waves have been ignored. Nonetheless, the wave is scattered by density fluctuations during its propagation. Formally, this scattering takes place in all directions. However, only the signal scattered back to the receiving antenna is of interest for reflectometry studies. The Bragg condition states that the scattering is the most efficient when the momentum and energy of the waves are conserved,

$$\begin{aligned} \vec{k}_s &= \vec{k}_i \pm \vec{k}_f \\ w_s &= w_i \pm w_f. \end{aligned} \tag{3.21}$$

The subscripts s, i and f refer to the scattered wave, the incident (probing) wave and the density fluctuations, respectively. Providing that $w_f \ll w_i$, the dispersion relation requires that $|k_i| = |k_s|$ [27]. The scattering angle (Fig. 3.4) follows the Bragg's law

$$|k_f| = 2|k_i| sin(\frac{\theta}{2}). \tag{3.22}$$

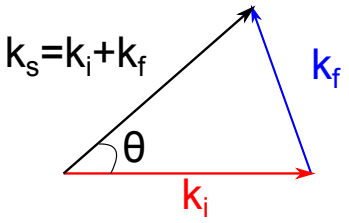

FIGURE 3.4: Illustration of the Bragg resonant condition

At normal incidence, which is mainly relevant to sweeping reflectometry, the Bragg condition reduces to $|k_f| = 2k_i$.

Chapter 4

Density profile reconstruction in presence of fluctuations

Sweeping reflectometry was initially developed to measure the electron density profile in fusion experiments [23]. Turbulence induced density fluctuations were considered to have a deleterious effect on the density profile reconstruction [50]. A proper density profile reconstruction requires that the plasma does not evolve while being probed. On the first reflectometers, the sweeping time was too long to freeze the turbulence and consequently, fulfill the latter condition.

The sweeping time of the Tore Supra reflectometer has been recently reduced to 2 μs which should be sufficient to freeze the turbulence [41] given that the turbulence power spectrum is dominated by frequencies below 500 kHz [51, 52]. Such an improvement might offer the possibility to reconstruct the density profile in presence of turbulent fluctuations. This latter point is addressed here. First, the influence of the sweeping time on the determination of the time of flight of the probing wave is presented. Then the profile reconstruction algorithm is briefly described and its ability to reconstruct fluctuating profile is analyzed in detail.

4.1 Influence of the sweeping time on the time of flight of the probing wave.

The time of flight τ is the time the probing wave takes to travel back and forth from the antenna to the cut-off layer

$$\tau(F) = \frac{1}{2\pi}\frac{\partial\phi(F)}{\partial F}, \tag{4.1}$$

F and ϕ are the probing wave frequency and the phase of the complex signal, respectively. τ can be either calculated using the phase derivative or the beat frequency F_b

$$F_b(F) = \frac{1}{2\pi}\frac{\partial\phi(F)}{\partial t} = V_s\tau(F), \tag{4.2}$$

where $V_s = \Delta F/\Delta t$ is the sweeping rate.

The beat frequency can be computed using a sliding FFT analysis. The procedure is described in [26] and will not be further detailed here. Fig. 4.1 illustrates the influence of the sweeping time on the determination of the time of flight. In case of a large

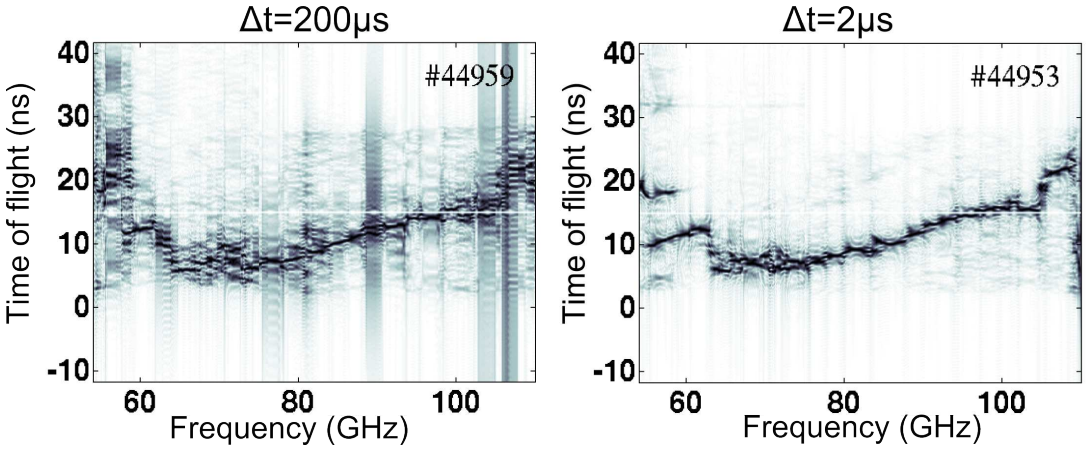

FIGURE 4.1: Time of flight measured with 200 μs (left) and 2 μs (right) sweeping time. Tore Supra discharges used in this example are Ohmic discharges with similar plasma parameters.

sweeping time $\Delta t = 200\ \mu s$ (low sweeping rate) the turbulence is not frozen. The Doppler shift created by the turbulent structures motions during the sweep makes the precise evaluation of the time of flight difficult (Fig. 4.1, left). This is mostly due to the fact that the widths of the beat and turbulent frequency spectra are similar (of the order of 1 MHz). Inversely, when the sweeping time is sufficiently short, the width of the beat frequency spectrum is much larger than those of the turbulent spectra. The time of flight is therefore more precisely determined (Fig. 4.1, left).

4.2 Profile reconstruction algorithm

The routine reconstruction of electron density profiles on TS discharges is performed by means of the Bottollier-Curtet (B-C) algorithm [25]. The fundamental assumption underlying the algorithm is the monotonicity of the refractive index. The implications of the latter assumption on the reconstruction of fluctuating density profiles are discussed in Sec. 4.2.1. Without detailing completely the algorithm, we present here the basic

ideas. A complete description of the algorithm is presented in [24]. B-C algorithm is based on the WKB approximation which states that the phase is the integral of the local wavenumber between a reference position (which is usually the antenna position r_a) and the cutoff layer position $r_c(F)$

$$\phi(F) = 2k_0(F) \int_{r_a}^{r_c(F)} N_X(F, n_e(r), B(r))dr - \frac{\pi}{2}. \tag{4.3}$$

Here, the dependences of the refractive index have been explicited. ϕ and F are directly measured and $B(r)$ can be obtained from the magnetic equilibrium reconstruction. The unknown quantities are the cutoff layer position $r_c(F)$ and the electron density $n_e(r)$. Using Eq. 4.3, it is easy to see that the difference of the phases measured for two adjacent probing frequencies F_{i+1} and F_i is the shaded area depicted on Fig. 4.2

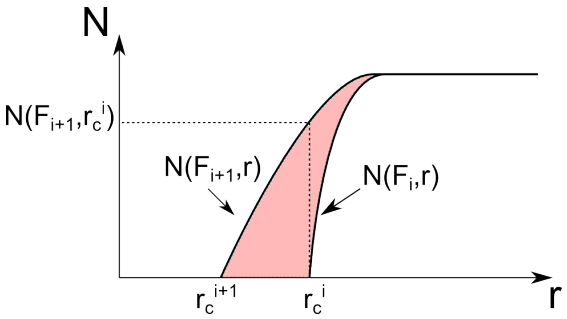

FIGURE 4.2: Schematic of the Bottollier-Curtet algorithm for electron density profile reconstruction.

The shaded area is proportional to the area of the triangle of base $r_c^{i+1} - r_c^i$ and height $N_X(F_{i+1}, r_c^i)$

$$\frac{\phi(F_{i+1})}{k_0(F_{i+1})} - \frac{\phi(F_i)}{k_0(F_i)} \propto \frac{4}{3}(r_c^{i+1} - r_c^i)N(F_{i+1}, r_c^i). \tag{4.4}$$

If the density profile is known up to r_c^i and by assuming that it can be linearized [1] between the cutoff positions r_c^i and r_c^{i+1}, the term $N(F_{i+1}, r_c^i)$ can be explicitly calculated. It is then trivial to compute the r_c^{i+1} radial cutoff position. The associated density is obtained via the cutoff condition

$$F_{pe}^2(r_c^{i+1}) = F_{i+1}^2 - F_{i+1}F_{ce}(r_c^{i+1}.) \tag{4.5}$$

The B-C algorithm is initialized by thresholding the reflected signal amplitude. Close to the tokamak walls, the electron density is very low and the probing wave is not sufficiently

[1] An optimized version of the algorithm has been proposed in [53] where the dielectric permittivity is assumed to be linear between two successive radial positions

reflected. The first probing frequency for which the amplitude of the reflected signal is above the threshold is called the first cutoff frequency F_1. The electron density associated to the first cutoff frequency is assumed to be equal to zero. Therefore, the first cutoff position r_1 is deduced from $F_1 = F_{ce}(r_1)$.

4.2.1 Effect of a gaussian density fluctuation on the profile reconstruction

A sufficiently large density fluctuation may shadow a part of the density profile. In this case, the probing wave *does not see* the part of the profile behind the fluctuation. Such a situation seems intuitively problematic for the profile reconstruction. Indeed, the Bottolier-Curtet algorithm was originally designed to reconstruct unperturbed density profiles, i.e. density profiles which monotonically increases from the SOL to the plasma center. The monotonicity might be violated in presence of density fluctuations. The first question to concentrate on is thus the following : what is the largest fluctuation amplitude for which the density profile can be properly reconstructed? This question is addressed by considering density profiles perturbed by a Gaussian fluctuation. An analytic condition which links the problem parameters (amplitude, width and position of the perturbation; scale length of the density profile) is derived for the case of linear and exponential density profiles. This condition sets a limit for the perturbed profile reconstruction.

Condition for a proper density profile reconstruction in X-mode reflectometry

As the probing wave propagates through the plasma, the wave *does not feel* directly the density fluctuations but rather the fluctuations of the refractive index N_X. Close to the cutoff,

$$F_{pe}^2 \approx F^2 - FF_{ce} \tag{4.6}$$

and N_X reduces to:

$$N_X(F, r) = \sqrt{2(1 - \frac{F_{pe}^2(r)}{F^2 - FF_{ce}(r)})} \tag{4.7}$$

At this point, the reconstruction is assumed to be correct if the refractive index decreases monotonically as the wave goes deeper into the plasma: $\partial N_X/\partial r > 0$ where r is the distance to the plasma center. This hypothesis is justified in the next paragraph. Since

$N_x \geq 0$ on the wave path, $\partial N_X/\partial r > 0 \leftrightarrow \partial N_X^2/\partial r > 0$. Using simple algebra, Eq. 4.7 leads to

$$\frac{\partial N_X^2}{\partial r} = -2\frac{(F^2 - FF_{ce})\partial_r F_{pe}^2 - F_{pe}^2\partial_r(F^2 - FF_{ce})}{(F^2 - FF_{ce})^2}. \tag{4.8}$$

Using again Eq. 4.6 and the fact that the probing frequency is fixed and does not depend on the radial position; $\partial_r F = 0$, the previous condition corresponds to

$$\partial_r N_X > 0 \leftrightarrow \partial_r F_{pe}^2 + F\partial_r F_{ce} < 0. \tag{4.9}$$

Exponential density profile

Here, we examine the case of an exponential density profile perturbed by a Gaussian fluctuation.

$$n_e(r) = n_{e0}e^{-\frac{1}{L_n}(r-a)}(1 + Ae^{-\frac{(r-r_0)^2}{2\sigma^2}}). \tag{4.10}$$

This profile is defined for $r > a$, a being the position where the density is maximal and equals to n_{e0}. A, r_0 and σ are the amplitude, position and width of the Gaussian perturbation, respectively. L_n is the unperturbed density profile scale length. The magnetic field profile is chosen to decrease as $1/r$ (typical for any tokamak), $B(r) = B_0R_0/(R_0 + r)$. B_0 is the magnetic field on the magnetic axis. The condition set by Eq. 4.9 reads

$$\partial_r F_{pe}^2 < -F\partial_r F_{ce}. \tag{4.11}$$

This implies that the derivative of the density profile must always be lower than the opposite of the magnetic field profile derivative. It can be easily shown that the derivative of a Gaussian is maximal at $r = r_0 \pm \sigma$. In case of a positive perturbation ($A > 0$), it is sufficient to find the parameters for which Eq. 4.11 holds at the position $r = r_0 - \sigma$ to ensure that the relation will be true everywhere. Rigorously, $\partial_r F_{pe}^2$ is not exactly maximum at $r = r_0 - \sigma$ because of the contribution of the unperturbed profile. However, this introduces only a small correction term. It will be shown numerically that the last assumption is fully justified.

At $r = r_0 - \sigma$, Eq. 4.11 writes

$$\frac{e^2}{4\pi^2 m_e \epsilon_0} n_{e0} e^{-\frac{1}{L_n}(r_0-\sigma-a)} \left(A e^{-1/2} (\frac{1}{\sigma} - \frac{1}{L_n}) - \frac{1}{L_n} \right) < -F \partial_r F_{ce}. \tag{4.12}$$

Noticing that $\partial_r F_{ce} = -F_{ce}/(r + R_0)$,

$$A e^{-1/2} \left(\frac{1}{\sigma} - \frac{1}{L_n} \right) - \frac{1}{L_n} < \frac{F F_{ce}(r_0 - \sigma)}{F_{pe}^{eq}(r_0 - \sigma)^2} \frac{1}{r_0 - \sigma + R_0}. \tag{4.13}$$

with

$$F_{pe}^{eq}(r) = \sqrt{\frac{e^2}{4\pi^2 m_e} n_{e0} e^{-(r-a)/L_n}}, \tag{4.14}$$

the plasma frequency associated to the unperturbed density profile. A condition on the perturbation amplitude is explicitly found

$$A < \left(\frac{F F_{ce}(r_0 - \sigma)}{(F_{pe}^{eq}(r_0 - \sigma))^2} \frac{1}{r_0 - \sigma + R_0} + \frac{1}{L_n} \right) \frac{e^{1/2}}{\frac{1}{\sigma} - \frac{1}{L_n}} \tag{4.15}$$

Linear density profile

The same exercise can be done in the case of a linear density profile.

$$n_e(r) = n_{e0}(1 - \frac{1}{L_n}(r - a))(1 + A e^{-\frac{(r-r_0)^2}{2\sigma^2}}). \tag{4.16}$$

After similar algebra, a condition on the perturbation amplitude is also obtained,

$$A < \left(\frac{F F_{ce}(r_0 - \sigma)}{(F_{pe}^{eq}(r_0 - \sigma))^2} \frac{1}{r_0 - \sigma + R_0} + \frac{1}{L_n} \right) \frac{e^{1/2}}{\frac{1}{\sigma}(1 - \frac{1}{L_n}(r_0 - \sigma - a)) - \frac{1}{L_n}} \tag{4.17}$$

Numerical validation

The model is validated for SOL plasma conditions, i.e. exponential density profile and large scale turbulence, which are of primary importance when comparing data from the reflectometer and the Pecker probes (Chapter 5). Starting with a known exponential density profile, the corresponding refractive index is computed for the relevant cutoff frequencies. The geometric optics phase is obtained by integrating the refractive index on the ray path (Eq. 4.3). Once the phase has been computed, the density profile is reconstructed with the B-C algorithm.

The density gradient length, perturbation width and position are fixed and set to typical values for SOL plasmas ($n_{e0} = 10^{18}\ m^{-3}$, L_n=2 cm, σ=0.5 cm and r_0= 5 cm). Only the perturbation amplitude is tuned around the limiting value giving by Eq. 4.15.

For the parameters used in this example, the limiting amplitude value is $A = 226\%$. Fig.4.3 shows the density profile reconstruction, for a density perturbation with $A = 220$ %. The perturbed density profile is clearly non-monotonic but the curve $N_x = 0$ is still monotonic. It can be observed that the profile is correctly reconstructed. In X-mode, the magnetic field damps the effect of density perturbations. This 'magnetic smoothing' allows to correctly reconstruct density profiles with relatively high density perturbations.

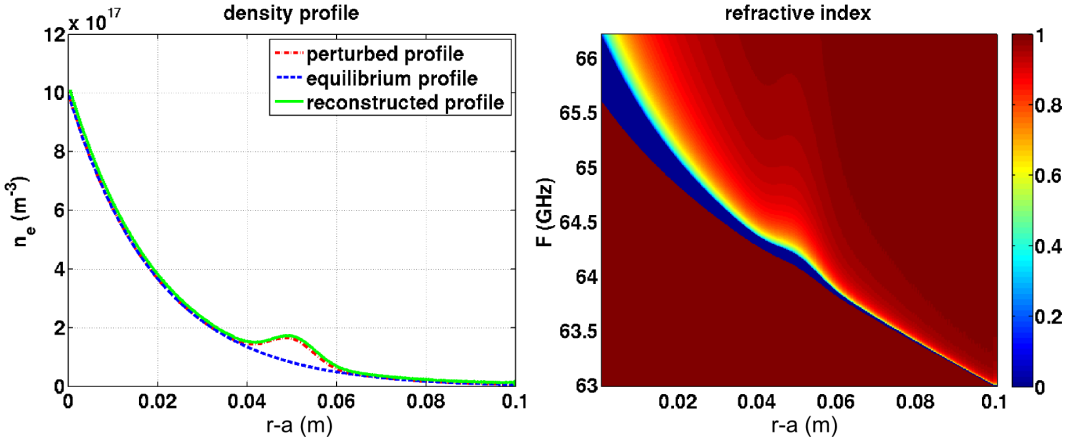

FIGURE 4.3: a) equilibrium profile (blue dashed curve), perturbed profile (red dashed-dotted curve) and reconstructed profile (green curve). The parameters are $n_{e0} = 10^{18}\ m^{-3}$, L_n=2 cm, $A = 220$ %, σ=0.5 cm and r_0= 5 cm. b) Refractive index computed on the perturbed profile.

When the perturbation amplitude exceeds the limiting value, the $N_X = 0$ curve is no longer monotonic (Fig. 4.4, simulation is performed for $A = 270$ %). The reconstructed profile oscillates behind the density perturbation. These oscillations lead to multiple density values for a given radial position which is physically unacceptable. However, if the perturbation amplitude does not exceed strongly the limiting value, the unperturbed part of the profile is still correctly reconstructed.

Using Eq. 4.15, parameters which ensure the convergence of the reconstruction algorithm can be estimated numerically with around 10% confidence.

Fig. 4.5 shows the behavior of the amplitude threshold when the others parameters are tuned. Three dependencies are clearly observable:

1. The outer is the perturbation, the larger is the amplitude threshold.

2. The steeper is the density profile gradient, the larger is the amplitude threshold.

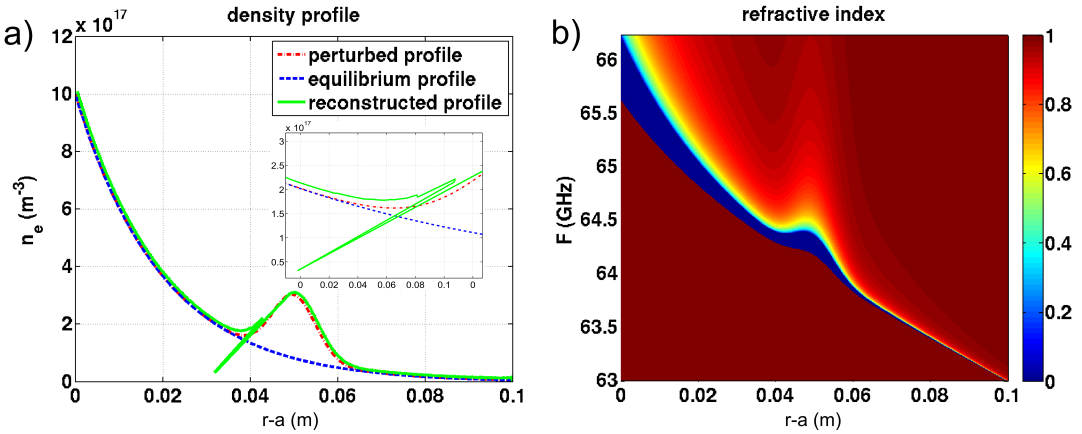

FIGURE 4.4: a) equilibrium profile (blue dashed curve), perturbed profile (red dashed-dotted curve) and reconstructed profile (green curve). The parameters are $n_{e0} = 10^{18}\ m^{-3}$, L_n=2 cm, A = 270 %, σ=0.5 cm and r_0= 5 cm. The inset is a zoom of the oscillation. b) Refractive index computed on the perturbed profile.

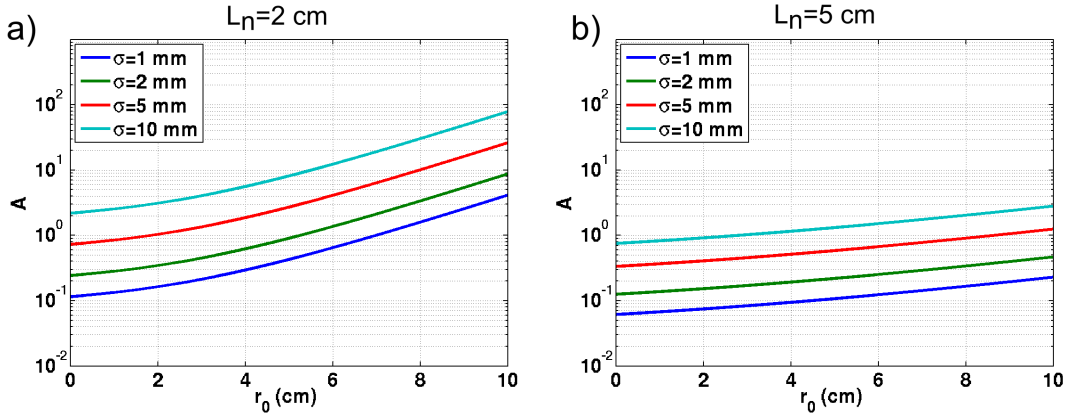

FIGURE 4.5: Dependence of the limiting amplitude (A) with respect to the perturbation position (r_0). The x-axis represents the perturbation position. Two values of the density gradient scale length are studied (a and b). For each case, the perturbation width (σ) is tuned.

3. The larger is the width of the perturbation, the larger is the amplitude threshold.

In spite of its simplicity, qualitative conclusions can be drawn from the model. The fluctuation level was estimated around tens of percent in the Tore Supra SOL [54]. In the far SOL, the turbulence is believed to be dominated by large-scale high-amplitude fluctuations. Therefore, all the conditions required for a correct density profile reconstruction might be fulfilled in this region (i.e. the refractive index is monotonic, there is no secondary cutoff). Closer to the LCFS, small scales fluctuations are present and can potentially degrade the density profile reconstruction.

4.3 Statistical analysis of fluctuating density profiles

The experimental values used as inputs for the density reconstruction algorithm are the phase $\phi(F,t)$ and the magnetic field profiles $B(R)$. The outputs are the reconstructed radial positions $R(F,t)$ and the associated electron densities $n_e(F,t)$. An example of fluctuating density profile reconstructed with the B-C algorithm is shown in Fig. 4.6 a). Around the initialization position ($r/a \approx 1.225$), the reconstructed profile slightly oscillates (Fig. 4.6 c)). These oscillations are quickly damped and do not impact the rest of the profile.

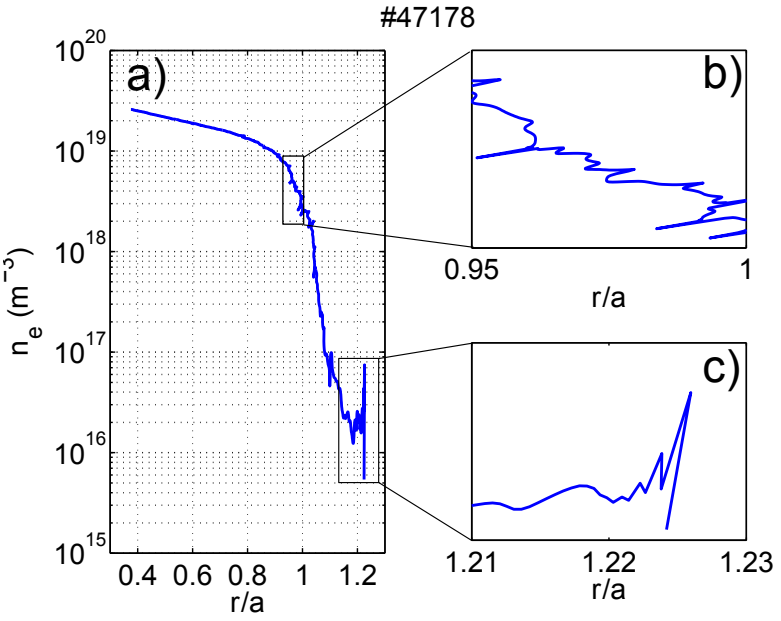

FIGURE 4.6: a) Reconstructed fluctuating density profile with respect to the normalized radial position for the ohmic discharge #47178. Zooms of the LCFS and extreme SOL regions are also shown (b and c).

Close to the LCFS, reconstruction accidents are common and lead to multiple density values for a fixed radial position (Fig. 4.6 b)). These accidents are possibly linked to a high fluctuation level, as mentioned in the previous section.

In the following, statistical tools are used to quantify the fluctuations properties. It has to be stressed that $R(F,t)$ and $n_e(F,t)$ are non independent quantities. A common error is to assume that, for a given frequency, only the density evolves. This error basically consists in treating $n_e(\mathbf{F},\mathbf{t})$ as $n_e(\mathbf{R},\mathbf{t})$. Fig. 4.7 shows that, at fixed frequency, both the density and radial position time series significantly fluctuate.

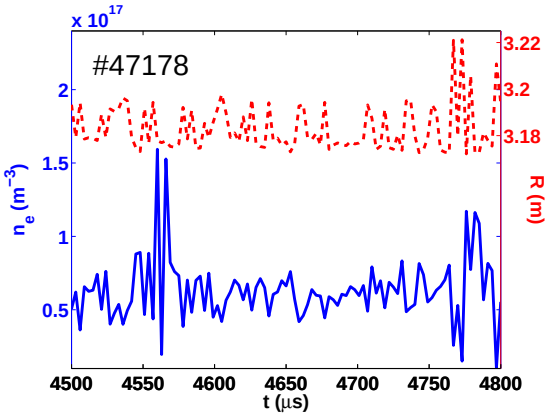

FIGURE 4.7: Time trace of the reconstruced density $n_e(F_0, t)$ (blue line) and radial position $R(F_0, t)$ (red-dashed line) for a fixed frequency (ohmic discharge #47178).

4.3.1 Joint probability distribution

The joint probability distribution[2] is an appropriate tool to take into account the joint variation of the radial positions and densities. The joint probability distribution PDF(n_e, R) gives the probability that a data point (n_e, R) lies in the interval $[n_e \pm \Delta n_e/2, R \pm \Delta R/2]$. Δn_e and ΔR are the bin sizes for the density and radial position, respectively. The size of the bin must be sufficiently large in order to obtain a significant number of points in each bin. In the example presented on Fig. 4.8, the bin sizes are $\Delta n_e = 6.14 \times 10^{16}$ m^{-3} and $\Delta R = 1.6$ mm. 3000 sweeps were performed during the burst shown on Fig. 4.8. Given that 2000 data points (n_e, R) are reconstructed for each sweeps, 6×10^6 data points were used to compute the $PDF(n_e, R)$. Consequently, a probability of 10^{-4} means that 600 data points lie in the corresponding bin.
The joint PDF is an elegant way to show the dispersion of the reconstructed density profiles. It can be observed that the distribution of the reconstructed profiles significantly broadens when going inside the closed field lines region ($R_{LCFS} = 3.1$ m).

4.3.2 Conditional probability distribution

When dealing with density fluctuations, it is more convenient to look at the statistical properties of the density fluctuations at a fixed position. This is done by using the conditional probability distribution $PDF_R(n_e)$. $PDF_R(n_e)$ is computed in two steps. First the densities $n_e(F, t)$ for which the associated radial positions $R(F, t)$ lie in the interval $[R \pm \Delta R/2]$ are extracted, then the PDF is computed on these densities. The

[2]Rigorously, only the *statistical* (and not the *probability*) distribution can be estimated from the data. However, the statistical distribution is assumed to converge to the probability distribution if the number of experimental data points is large enough. For the sake of clarity and simplicity, the statistical distribution are referred to as *PDFs* here)

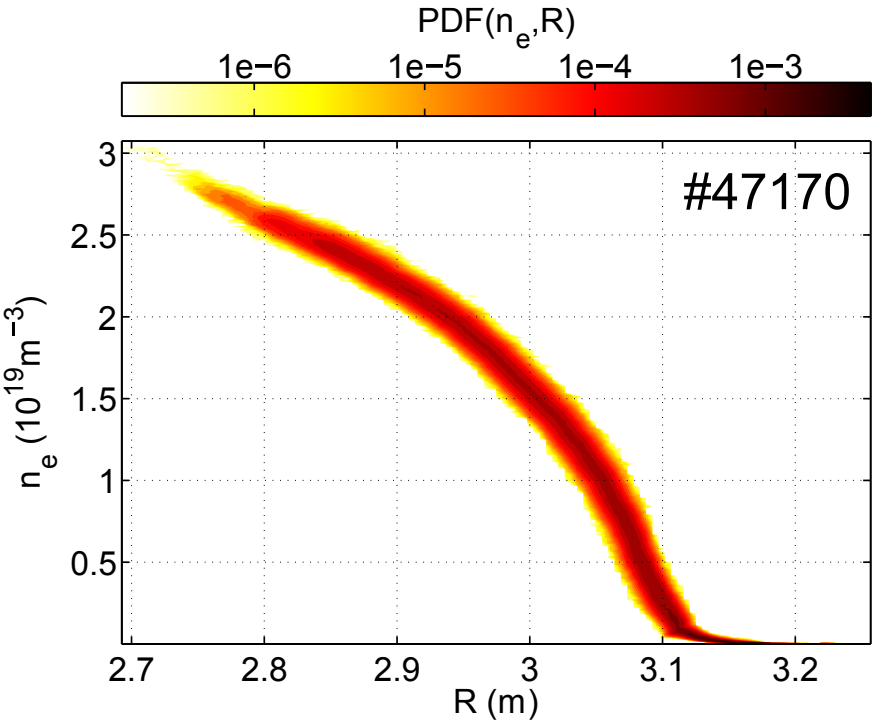

FIGURE 4.8: Joint statistical distribution of the reconstructed density and radial position.

conditional $PDF_R(n_e)$ can be seen as *a radial cut* of the joint $PDF(n_e, R)$ as depicted on Fig. 4.9 b).

In the following, the radial coordinate r/a is used in order to highlight the differences between the SOL ($r/a > 1$) and the close field lines region ($r/a < 1$). Fig. 4.9 a) shows the $PDF_{r/a}(n_e)$ with respect to the radial position. The $PDF_{r/a}(n_e)$ was obtained by dividing the profile into radial intervals of approximately 5 mm. In each interval, the density has been normalized by subtracting the mean value and dividing by the standard deviation. The skewness profile, which measures the asymmetry of the distribution, is superposed. The skewness is a third order moments and is defined for an arbitrary data set x_i as

$$S \approx \frac{1}{N} \sum_{i=1}^{N} \left(\frac{x_i - \langle x \rangle}{\sigma_x} \right)^3, \tag{4.18}$$

where are $\langle x \rangle$ and σ_x are the mean value and standard deviation, respectively.

In the core region ($r/a < 0.8$), the turbulence is broadband and exhibits Gaussian statistics leading to nearly symmetric distribution (the skewness is roughly equal to zero). Just inside the LCFS, the distribution is skewed towards negative values (Fig. 4.9 b)) whereas outside the LCFS, the distribution is skewed towards positive values (Fig. 4.9 c)). The skewness inversion is characteristic of the edge SOL transition and was observed in many tokamaks [21]. Skewed distributions are considered as to be

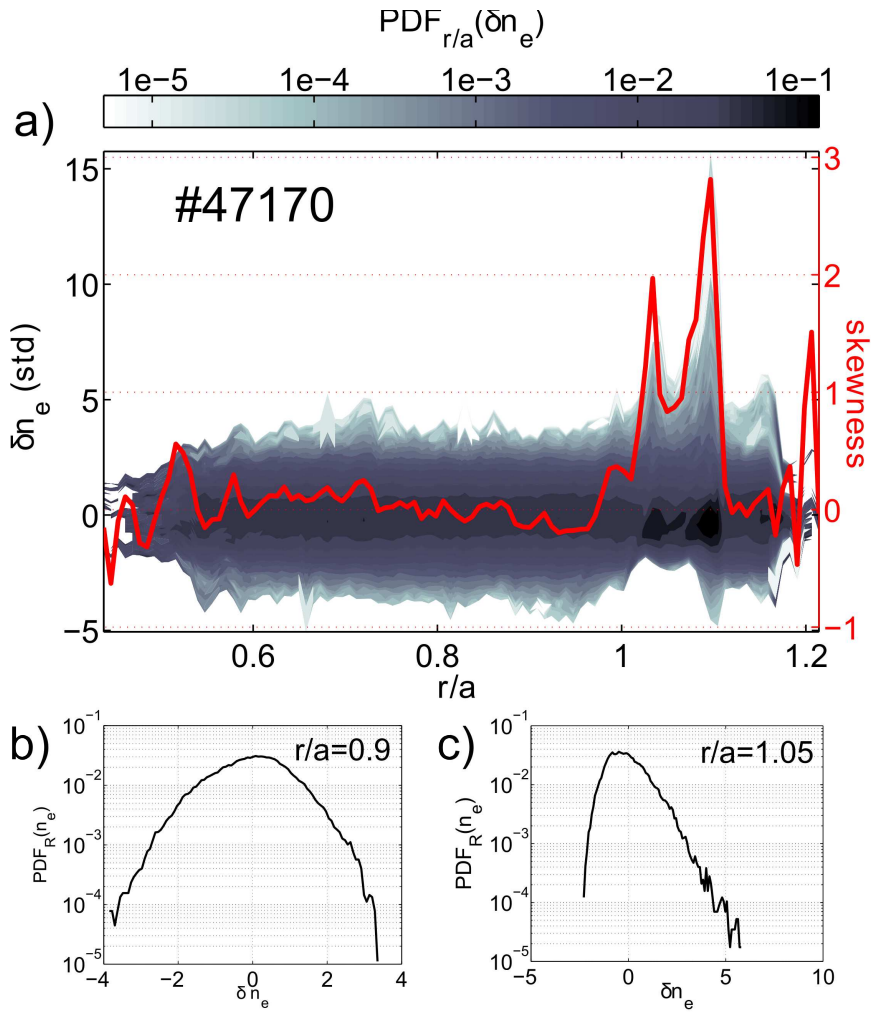

FIGURE 4.9: a) Conditional statistical distributions of the reconstructed density given the radial position. b) and c) distribution of the normalized density at $r/a = 0.9$ and $r/a = 1.05$.

consequence of coherent structures which originate in the surroundings of the LCFS. The coherent structures can be either negative or positive density fluctuations. Negative density fluctuations are dominant in the edge region ($0.8 \leq r/a < 1$), which leads to the negative skewness. Inversely, positive density fluctuations are dominant in the SOL plasma and leads to positive skewness.

Nevertheless, an extended analysis of the statistical properties of the fluctuating density profile is prevented by two "side effects" of the reconstruction algorithm. These effects are presented in the following section.

4.3.3 Statistical properties of the density profiles in the far SOL

Fig. 4.10 shows the joint and conditional statistical distributions computed for TS discharge #47178 in the far SOL region. Two branches on the joint statistical distribution

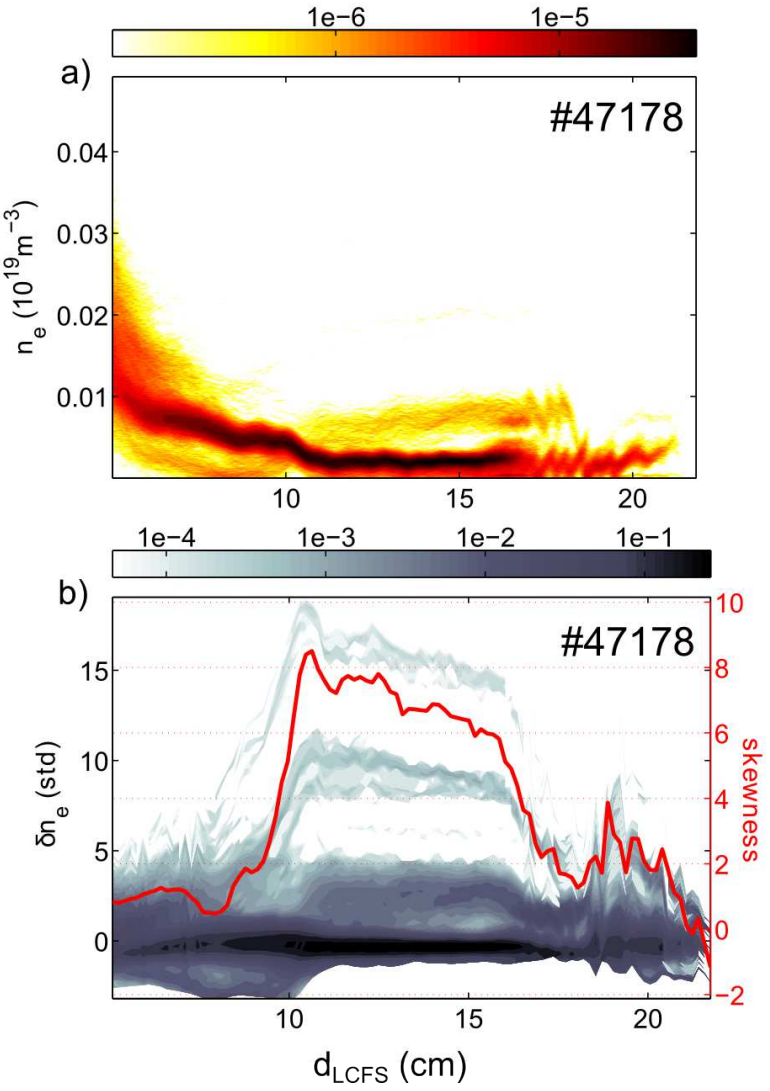

FIGURE 4.10: a) Joint probability distribution of the reconstructed density and radial position in the far SOL. b) conditional probability distribution of the density given the radial position in the far SOL. The radial position is labeled by d_{LCFS}, the distance to the LCFS.

are clearly seen in Fig. 4.10 a). The lower branch corresponds to the most frequent profile. The number of profiles in the upper branch is about 100, which is significantly lower than the number of profiles in the lower branch. However, it is sufficient to distort the high order statistical moments, which are very sensitive to large but rare events. Fig. 4.10. b) shows the conditional statistical distribution of the density and the associated skewness. The skewness reaches extremely large values (≈ 8) where the distribution is multimodal. Deeper in the SOL ($d_{LCFS} < 10$ cm), the skewness decreases to moderate values ($S \approx 1$) which traduces asymmetric but monomodal distributions.
In the following, some possible causes of the multimodal distributions are discussed.

Fig. 4.11 shows the time evolution of the first cutoff position for the ohmic discharge #47178. For t $< 600\ \mu$s, the first cutoff position varies smoothly and the plasma is

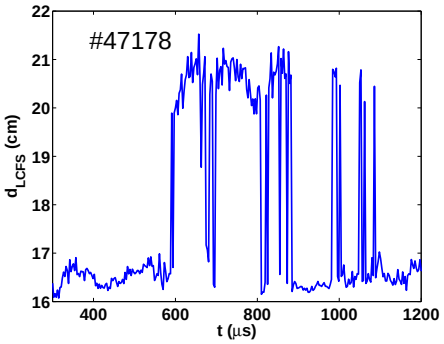

FIGURE 4.11: Time evolution of the first cutoff position for the Ohmic discharge #47178.

detected about 16.5 cm outside the LCFS. Then, an abrupt "jump" of roughly 4 cm amplitude is clearly visible around t $\approx$ 600 μs, taking place in 3 μs. Such a time series will obviously give a double peaked histogram, i.e multimodal statistics, with one peak around $d_{LCFS} \approx 16.5$ cm and the other at about $d_{LCFS} \approx 20.5$ cm.
Given that large radially propagating structures are abundantly observed in the SOL, it is quite natural to wonder if these jumps result from these turbulent structures. Such a possibility implies that the structures would propagate radially at about $4 \times 10^{-2}/3 \times 10^{-6} \approx 13$ km s^{-1} which is up to two orders of magnitude above the characteristic convective velocity ($\approx$ 0.1-1 km s $^{-1}$, see [21] and references therein). Consequently, propagating structures can hardly account for the jumps. An alternative mechanism is presented in the next paragraph.

Density profile initialization

The density profile initialization is critical for a proper reconstruction of the density profile in the far SOL. Recently, a new signal processing method based on tomographic analysis [55] has been developed and applied on the Tore Supra reflectometer signals. Among the merits of the new technique, it is now possible to initialize the density profile at densities as low as 10^{16} m^{-3}. Once parasitic echoes (as the backwall echo) have been removed, the profile is initialized by thresholding the reflected amplitude. As the density increases, the plasma becomes more reflecting and the signal amplitude increases. This threshold based method is suitable when the reflected amplitude monotonically increases with the probing frequency, which is unfortunately not the general case. Fig. 4.12 shows the reflected amplitude for two successive sweeps. The amplitudes have been low pass filtered in order to keep only the trend. The reflected amplitude globally increases with the probing frequency although this increase is not fully monotonic. A bump is observed around $F = 58\,GHz$ in the reflected amplitude. During the first sweep , the bump is below the threshold and the initialization frequency is $F_1 \approx 60.5$ GHz (the corresponding

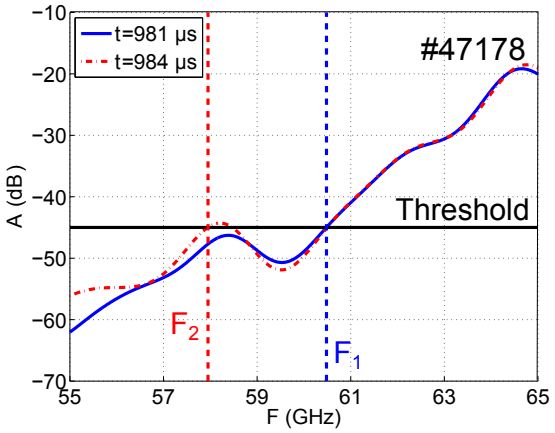

FIGURE 4.12: Reflected amplitude with respect to the probing frequencies measured for two successive sweeps. The threshold and the initialization frequencies are also shown.

cutoff position is $R_1 \approx 3.26$ m). During the following sweep, the reflected amplitude has only slightly increased but now the amplitude crosses the threshold in front of the bump. The initialization frequency is thus significantly shifted towards a lower value ($F_2 \approx 58$ GHz, $R_2 \approx 3.3$ m) leading to a jump of the first cutoff position. It has to be stressed that the bump observed on the reflected amplitude is not a direct consequence of the turbulent activity. Indeed, the time average of the reflected amplitude still presents the bump while the turbulence effects cancel out. On this example, it might be sufficient to raise the threshold value to get rid of the jump problem. However, if the value chosen for the threshold is too large, a significant part of the plasma profile will not be taken into account. The choice of the threshold value should result from a compromise between jump avoidance and initializing the profile sufficiently far in the SOL. It is not possible to define a threshold value which gives optimal results independently of the plasma discharge. The threshold value needs to be determined on a case by case basis which makes difficult to effectively and automatically initialize the density profile.

4.3.4 Long range correlations in the closed magnetic field line region

In the core plasma, the density fluctuation level is moderate ($< 1\%$) [56]. This low fluctuation level should guarantee a proper density profile reconstruction. However, it is shown here that the core density profiles are affected by *accidents* which take place close to the LCFS.

Fig. 4.13 shows the contours of the reconstructed density for the ohmic discharge #47475. It can be asserted that density contours measured around r/a=0.3 up to r/a=0.9 are highly correlated. This very long range correlation results from a shift of the reconstructed profiles, which is an artificial effect introduced by the reconstruction algorithm.

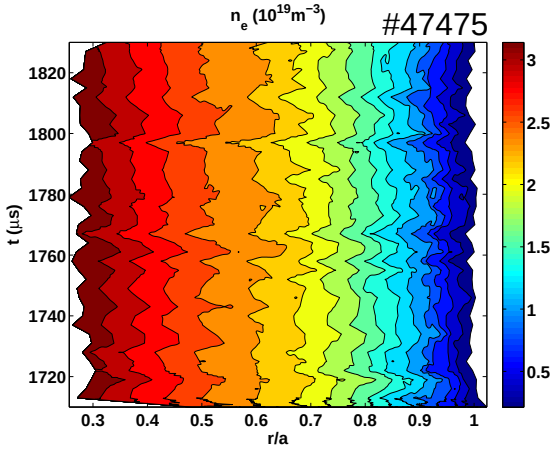

FIGURE 4.13: Contour plot of the reconstructed density for the #47175 Ohmic discharge

In the following, a numerical model is used to identify the origin of the observed shifts of the profile. Fig. 4.14 a) shows the time of flight (ToF) determined by FFT analysis on #47178 .

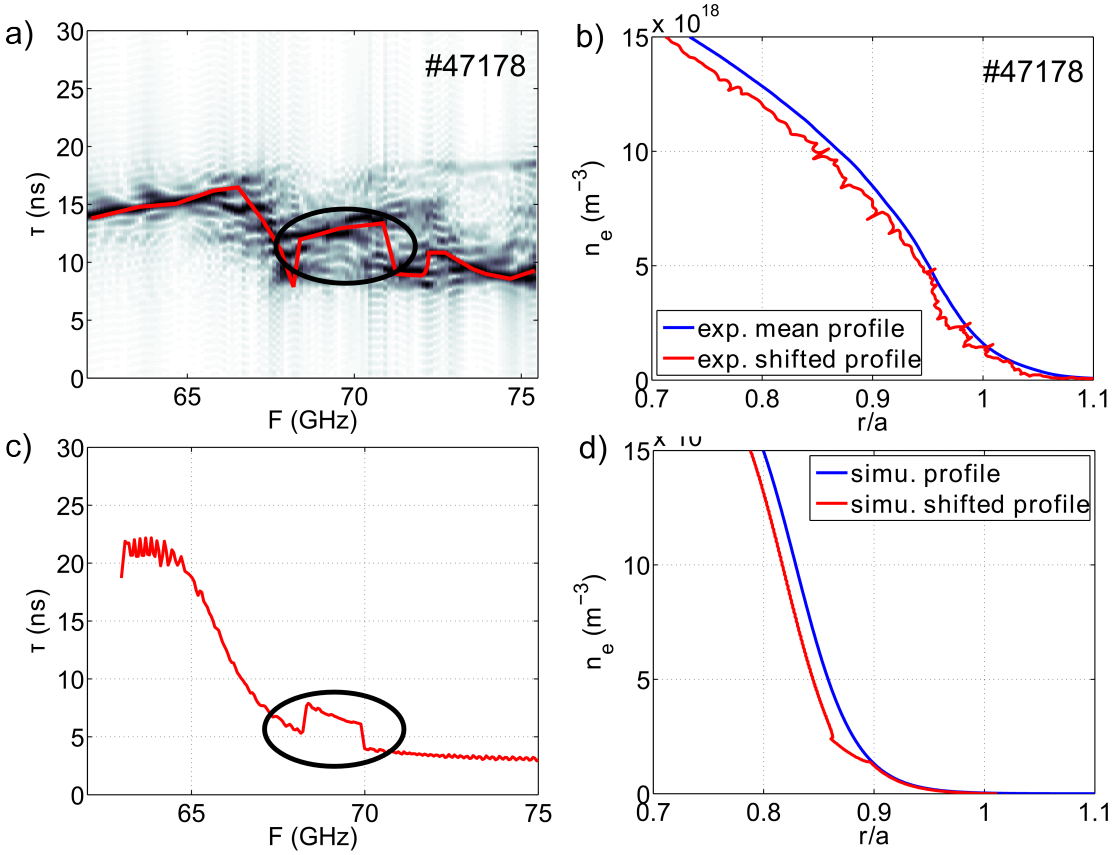

FIGURE 4.14: a) time of flight determined by FFT analysis and b), the associated reconstructed density profile (the mean profile is also shown). c) simulated time of flight and d), the associated perturbed density profile (the unperturbed profile is also shown).

A jump of the ToF , observed around $F \approx 68$ GHz, possibly causes a global shift of the fluctuating profiles with respect to the mean profile (Fig. 4.14 b). This situation was numerically reproduced in order to investigate the link between the ToF jumps and profile shifts. To this end, the ToF associated to an initial density profile (Fig. 4.14 d, blue curve) was computed using the WKB approximation. A rectangular step type perturbation was superimposed (Fig. 4.14 c) to qualitatively reproduced the experimental features. The density profile (Fig. 4.14 d, red curve) reconstructed from the perturbed ToF is clearly shifted with respect to the initial profile. This models confirms, at least qualitatively, that the profile shifts are due to jumps of the ToF. The jumps of the ToF appear in the surroundings of the LCFS. As the jumps are not compensated, the recursive reconstruction algorithm propagates the error to the whole profile. The origin of these jumps has not yet been identified.

4.4 Summary

The reconstruction of fluctuating density profiles was addressed in this chapter. The possible shadowing of the density profile by large amplitude fluctuations turned out to be a marginal problem. It was shown in Sec. 4.2.1 that thanks to X-mode polarization, the density profile remains monotonic up to relatively large fluctuation levels. However, various phenomena, which were not considered a priori, may have deleterious effects when reconstructing fluctuating density profiles. The threshold method used to initialize the density profile frequently leads to jumps of the first cutoff position. These jumps generate multimodal statistical distributions (Sec. 4.3.3). In the closed magnetic field line region, the instantaneous profiles are shifted one respect to each other. The global shift is caused by leaps of the time of flight which appear in the surrounding of the LCFS.

With the present treatment of sweeping reflectometry data, the fluctuating profiles appear to be affected by artificial effects introduced by the reconstruction algorithm. The analysis of the fluctuation properties of the reconstructed profile should be thus avoided particularly in the plasma core and far SOL. However, it might be possible to solve the initialization problem. It was shown that the jumps of the first cutoff position were related to the non monotonicity of the mean reflected amplitude. A method, which takes into account the mean amplitude profile, may bring satisfactory results for the profile initialization. It would probably be more complicated to overcome the shift of the profiles given that it is closely linked to the recursive character of the B-C algorithm.

It appears that the region right outside the LCFS is not affected by these undesired effects. As a consequence, the next chapter is devoted to analyze the fluctuation properties

in the few centimeters beyond the LCFS, where measurements from ultrafast sweeping reflectometry and pecker probes are available.

Chapter 5

Comparison of the measurements from ultrafast sweeping reflectometry and pecker probe in Tore Supra SOL

Turbulence measurements in tokamak plasmas are challenging. The interpretation of turbulent data often requires strong assumptions. In general, the justification of the assumptions cannot be forwardly deduced from the measured data. However, the assumptions can be indirectly tested by comparing data obtained from independent diagnostics. If turbulence data, measured by diagnostics based on significantly different physical mechanisms, exhibit the same properties, it is then reasonable to accept the underlying assumptions.

This idea has motivated a detailed comparison of the signals measured by the ultrafast sweeping reflectometer and the Langmuir probe. Both diagnostics are sensitive to the electron density and its fluctuations, consequently the properties of the latter will be compared with the aim to discuss the assumptions underlying the interpretation of their signals, and specifically the role played by the electron temperature fluctuations. To this purpose, measurements obtained in Ohmic discharges in the SOL region of Tore Supra are presented.

First, the parameters of the analysed discharges are presented. As a visual inspection of the data is not sufficient to decide if the measurements from both diagnostics are consistent, several indicators are used. The density profiles are shown in the close[1] SOL.

[1] *Close* SOL designates the region extending from the LCFS to 2-3 cm outside the LCFS, where probe measurements are available.

Then, the statistical distributions computed at a fixed radial position are compared. The fluctuation level and the skewness radial profiles are also analyzed. Finally, the temporal properties of the probe and reflectometer signal are investigated.

5.1 Parameters of the analyzed discharges

The experimental setup and the two diagnostics have been extensively presented in Chap. 2 and only few points are reminded here. The reflectometer and the probes share the same equatorial port on the Tore Supra tokamak. The probe is inserted in the antenna limiter (LPA) right next to the reflectometer. The spatial proximity of the reflectometer and the probe reduces the eventual effects of poloidal and toroidal asymmetries.

7 Ohmic discharges ($\#47125, 47126, 47171, 47177 - 47179, 47182$) have been analyzed. During a single discharge, several independent datasets can be acquired. A dataset acquired by the reflectometer is referred to as a *burst* whereas a dataset acquired by the probe is referred to as a *plunge*. In total, 16 bursts and plunges have been compared. The bursts and plunges were performed almost simultaneously. This quasi-simultaneity guarantees that the plasma parameters do not evolve between a burst and the associated plunge. However, the plasma parameters might possibly evolve between different data acquisitions. The range of parameters covered by the chosen dataset is presented in Tab. 5.1.

Parameter	B_0 (T)	$\langle n_e \rangle$ (m^{-3})	Ip (MA)	P_Ω (MW)	R_0 (m)	LCFS (m)	LPA (m)
Min. value	3.2	1.4×10^{19}	0.85	0.63	2.35	3.06	3.13
Max. value	3.7	5.0×10^{19}	1.3	1.43	2.52	3.13	3.15

TABLE 5.1: Range of plasma parameters for the 16 analyzed datasets corresponding to 7 Ohmic discharges $\#47125, 47126, 47171, 47177 - 47179, 47182$

5.2 SOL density profiles

The SOL electron density profiles were reconstructed for the 16 datasets. Density profiles obtained by reflectometry measurements were averaged over time intervals lasting between 3 and 15 ms, i.e. much longer than the fluctuations time scale.

5.2.1 Reconstruction of density profiles from the ion-saturation current measurement

The probe scans a region of 3.5 cm radial extent in approximately 1 ms. The probe density profiles were obtained using the relation between the ion-saturation current and the electron density , $I_{i,sat} = Aen_e c_s^{probe}$, with $c_s^{probe} = \sqrt{(ZT_e + T_i)/m_i}$ and A the effective collection area. $I_{i,sat}$ and T_e are obtained by an exponential fit of the I-V curves. In general, the charge Z and the ion temperature T_i are not measured in the SOL plasma; setting their values to $Z = 1$ and $T_i = 2T_e$ is considered as a reasonable choice [57].

5.2.2 Comparison of the SOL density profiles

Fig. 5.1 a)-c) show 3 among the density profiles measured by probe and reflectometry. In these examples, the density measured by the probe is larger than the density measured by reflectometry. This difference is confirmed by Fig. 5.1 d) which shows the probe density against the reflectometer density for the 16 datasets. All the probe densities stand above the reflectometer densities.

5.2.3 Discussion

We first investigate whether the observed density discrepancy might be due to an underestimate of the ion temperature T_i and/or the charge Z. The role of Z on the ion-saturation current was found to be unsignificant [58], consequently only the impact of T_i is discussed here using a *reductio ad absurdum*. Assuming that the errors on the ion-saturation current and the average density profiles are negligible, then the ratio of these two quantities should provide a correct estimate of the ion sound speed, $c_s^{reflecto.} = I_{i,sat}/Aen_e^{reflecto.}$. The difference between $c_s^{reflecto.}$ and c_s^{probe} may reveal how large is the error on the assumption of the ion temperature. Fig. 5.2 shows a typical example of the comparison of $c_s^{reflecto.}$ and c_s^{probe}. c_s^{probe} decreases whereas $c_s^{reflecto.}$ increases with the distance to the LCFS, respectively. An increase of the ion sound speed in the SOL region requires that the ion temperature increases to compensate the decrease of the electron temperature. Experimental measurement in Tore Supra SOL shows a decrease of T_i with the distance to the LCFS [57]. Consequently, this scenario is hardly acceptable.

The ratio of the ion-to-electron temperature is plausibly underestimated but cannot explain alone the differences on the measured densities. Many other error sources can have deleterious effects on the density measurements. To list a few, uncertainties on the

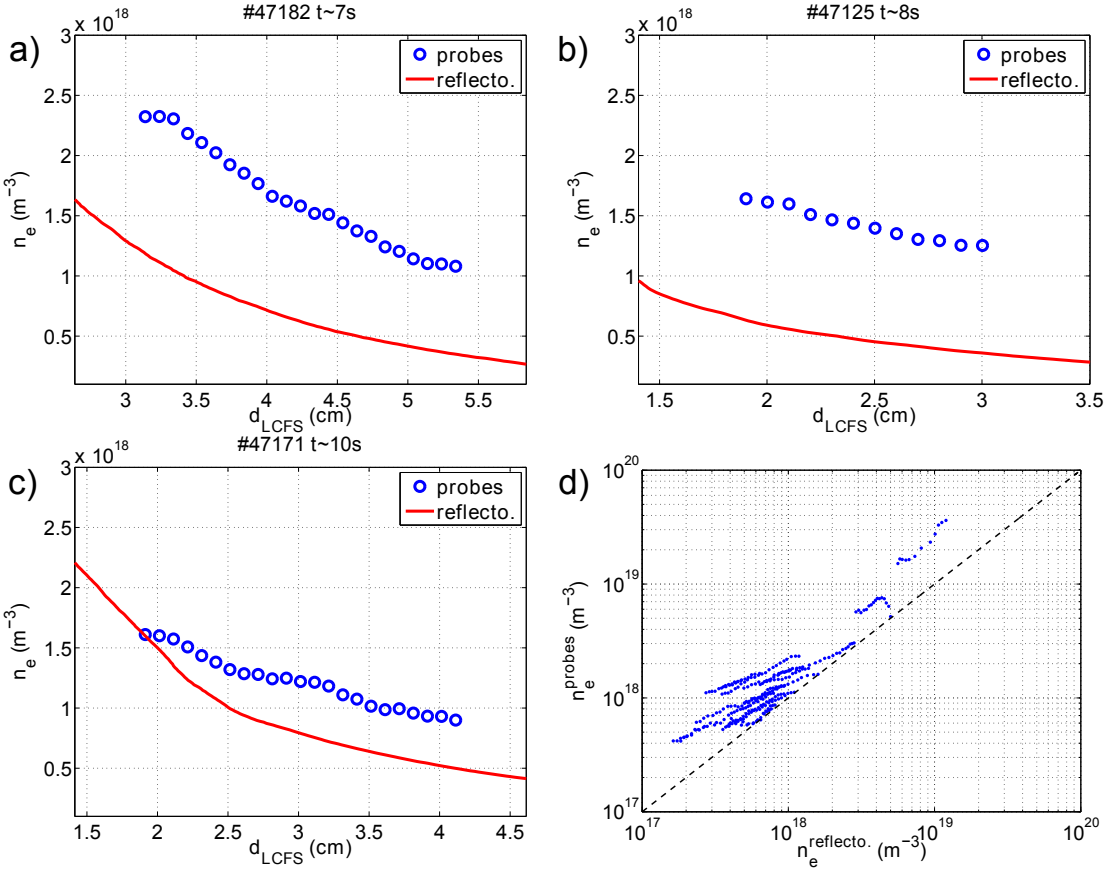

FIGURE 5.1: a)-c) Density profiles measured in the SOL region. d) Comparison of the densities measured by reflectometry and probe for the 16 datasets corresponding to 7 different Ohmic discharges. The bisectrix (black line) is also shown.

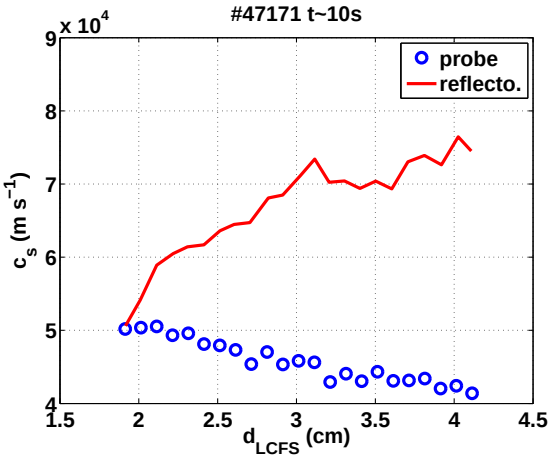

FIGURE 5.2: Radial evolution of the sound speed esimated from probe and reflectometry data

LPA position and uncertainties on the magnetic equilibrium reconstruction can seriously impact the densities estimated from the pecker probe and the reflectometer, respectively.

5.3 Comparison of the statistical properties

The previous section was dedicated to compare the average density profile, which is an equilibrium plasma quantity. In this section, the properties of the density fluctuations are compared. Statistical indicators are suitable to quantify the properties of SOL density fluctuations [59]. In this region, the turbulent activity is generally intermittent, which is traduced by a non-Gaussian and skewed PDF [60, 61]. The fluctuation level is here rather large and can reach tens of percent [62].

Before presenting the results of the comparison of the statistical properties, it is worth to explain how the densities fluctuations are extracted from the ion-saturation signal and the density profile obtained by reflectometry.

5.3.1 Extraction of the density fluctuations

The outcome of a measurement of plasma turbulence X(r,t) is assumed to be composed of an equilibrium part $X^0(r)$ and a fluctuating part $\tilde{X}(r,t)$,

$$X(r,t) = X^0(r) + \tilde{X}(r,t). \tag{5.1}$$

By definition, the equilibrium part is time independent and depends only on the spatial position. Using this representation, the fluctuating component can be extracted by subtracting the equilibrium part. The equilibrium part $X^0(r)$ is identified as the time average of the signal $\langle X(r)\rangle_t$.

Application to the probe signal

The pecker probe moves into the plasma while measuring the ion-saturation current. During a single plunge, it is consequently not possible to obtain an ensemble of measurements at a fixed radial position. This problem is overcome by assuming that the probe signal is stationary on a radial interval of small extent. For a given radial interval, the ion-saturation current is proportional to

$$I_{i,sat}(t) \propto (n_e^0 + \tilde{n}_e(t))(T_e^0 + \tilde{T}_e(t))^{1/2}. \tag{5.2}$$

If the effects of the electron temperature fluctuations on the ion saturation current are neglected in the SOL, the fluctuating component of the ion-saturation is proportional to the density fluctuations $I_{i,sat}(t) - \langle I_{i,sat} \rangle \propto \tilde{n}_e(t)$.

Comments on the probe collector asymmetries: As mentioned in Sec. 2.2.1; two collectors, located on both sides of the probe, measure $I_{i,sat}$. The collector A faces the high field side whereas the collector B faces the low field side. Fig. 5.3 shows a sketch of the probe as well as the raw ion saturation current $I_{i,sat}(t)$ measured by both collectors. The fluctuation amplitudes of the signal collected by B are larger than the fluctuation amplitudes on the signal collected by A. The comparison of the fluctuation level, defined as $\sigma_{I_{i,sat}}/\langle I_{i,sat} \rangle$, shows that the fluctuation level is significantly larger for $I^B_{i,sat}$ than for $I^A_{i,sat}$ (Fig. 5.3 b)), which corroborates the latter observation.

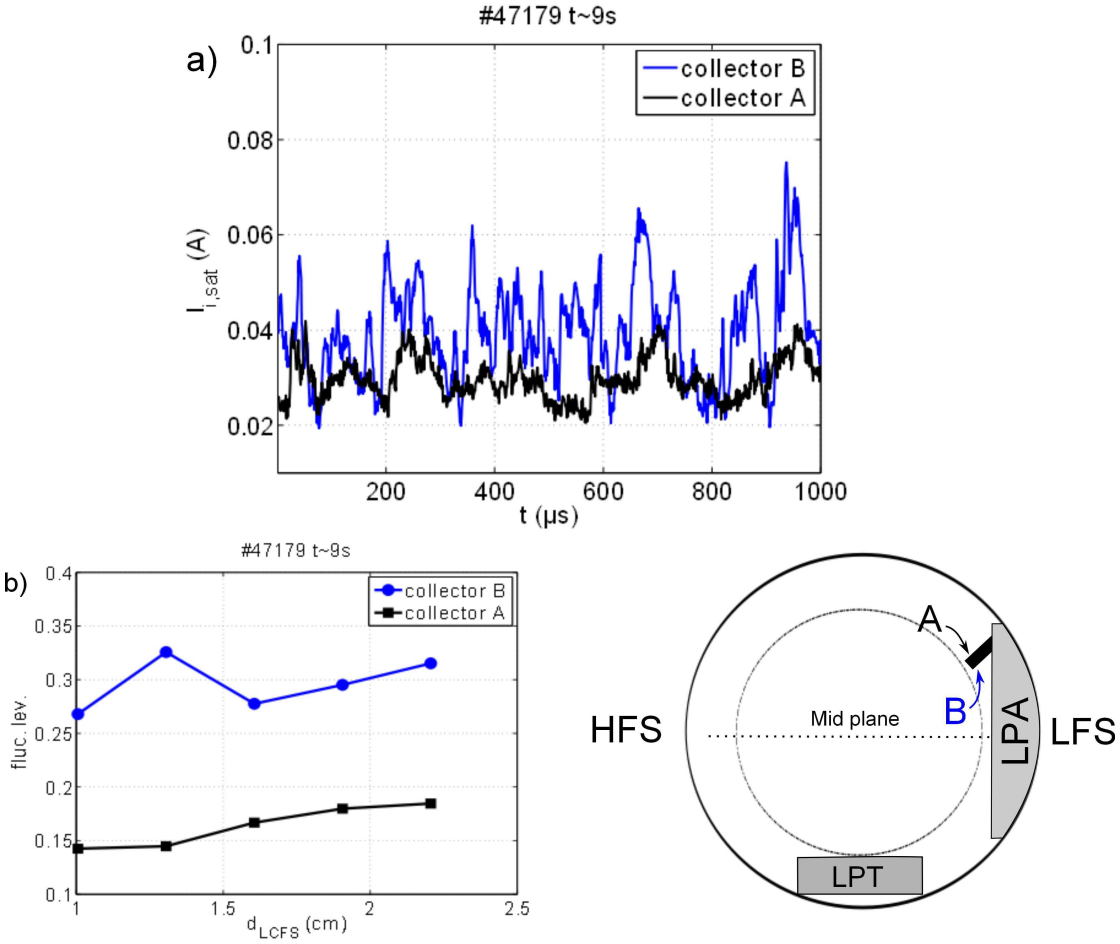

FIGURE 5.3: a) Comparison of the raw $I_{i,sat}$ measured 1 cm outside the LCFS by the collectors A and B. b) Comparison of the fluctuation levels. The fluctuation levels are computed on a radial interval of 3 mm extent.

This asymmetry is coherent with an interchange driven turbulence. Large density fluctuations are abundantly produced at the low field side mid plane, the most unstable region

with respect to the interchange instability. Due to fast parallel transport, the density fluctuations rapidly move along the field line connected to the collector B, resulting in a highly fluctuated signal. On the contrary, the collector A is connected to a more stable region which explains why fluctuations are less pronounced on this side of the probe. Similar asymmetries have also been observed with the rake probe [63] located at the top of the device (see Fig. 2.2). However, it is somehow surprising that A-B collector asymmetries are already present on the pecker probe although the probe is only 20° poloidally displaced with respect to the mid plane.

Given that the reflectometer is located in the mid plane, only the collector which faces the mid plane, namely the collector B, is used for the comparison of the electron density fluctuation properties.

Application to the reflectometer signal

The extraction of the density fluctuations from reflectometer measurements is direct because the B-C algorithm directly gives the reconstructed density. For a given radial interval, the density fluctuations are obtained through $\tilde{n}_e(t) = n_e(t) - \langle n_e \rangle_t$.

5.3.2 Comparison of the probability distribution functions

The PDFs have been estimated on radial intervals located between the deepest probe position r_{min}^{probe} and $r_{min}^{probe}+3$ mm. The number of measurement lying in the radial interval is significantly larger for reflectometry (between 2×10^4 and 1×10^5, depending on the discharge) than for the probe (around 8×10^3).

An *indicator* was constructed to quantify the similarity between PDFs from both diagnostics, defined as follows

$$\zeta_{PDF} = \sum_{j=1}^{N-1} |PDF^{reflecto.}(\tilde{n}_e^j < n_e \leq \tilde{n}_e^{j+1}) - PDF^{probe}(\tilde{n}_e^j < n_e \leq \tilde{n}_e^{j+1})|\Delta\tilde{n}. \quad (5.3)$$

N is the number of bins and $\Delta\tilde{n}$ is the bin size. Fig. 5.4 illustrates the indicator used to quantify the differences between two numerically generated PDFs. ζ_{PDF} is the absolute value of the area between the PDFs. The smaller is ζ_{PDF}, the more similar are the PDFs. In practice, $N = 50$ was chosen in order to ensure that a sufficiently large number of experimental points lie in each bin. Fig. 5.5 shows 4 of the PDFs. In general, the PDFs are positively skewed. For the analysed discharges, $\zeta_{PDF} = 0.08$ and $\zeta_{PDF} = 0.41$

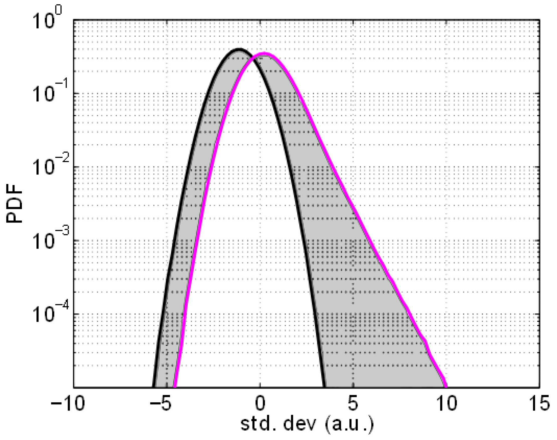

FIGURE 5.4: The shaded area between two PDFs corresponds to ζ_{PDF}.

are the minimum and maximum values of the ζ_{PDF} over the data set, respectively. As a rule of thumb, the agreement between PDFs is considered as good for $\zeta_{PDF} \leq 0.15$, acceptable for $0.15 < \zeta_{PDF} \leq 0.23$ and bad for $\zeta_{PDF} > 0.23$. Using this classification, 9 PDFs out of 16 are found to be in good agreement. 5 PDFs out of 16 agree acceptably well and 2 PDFs out of 16 do not agree.

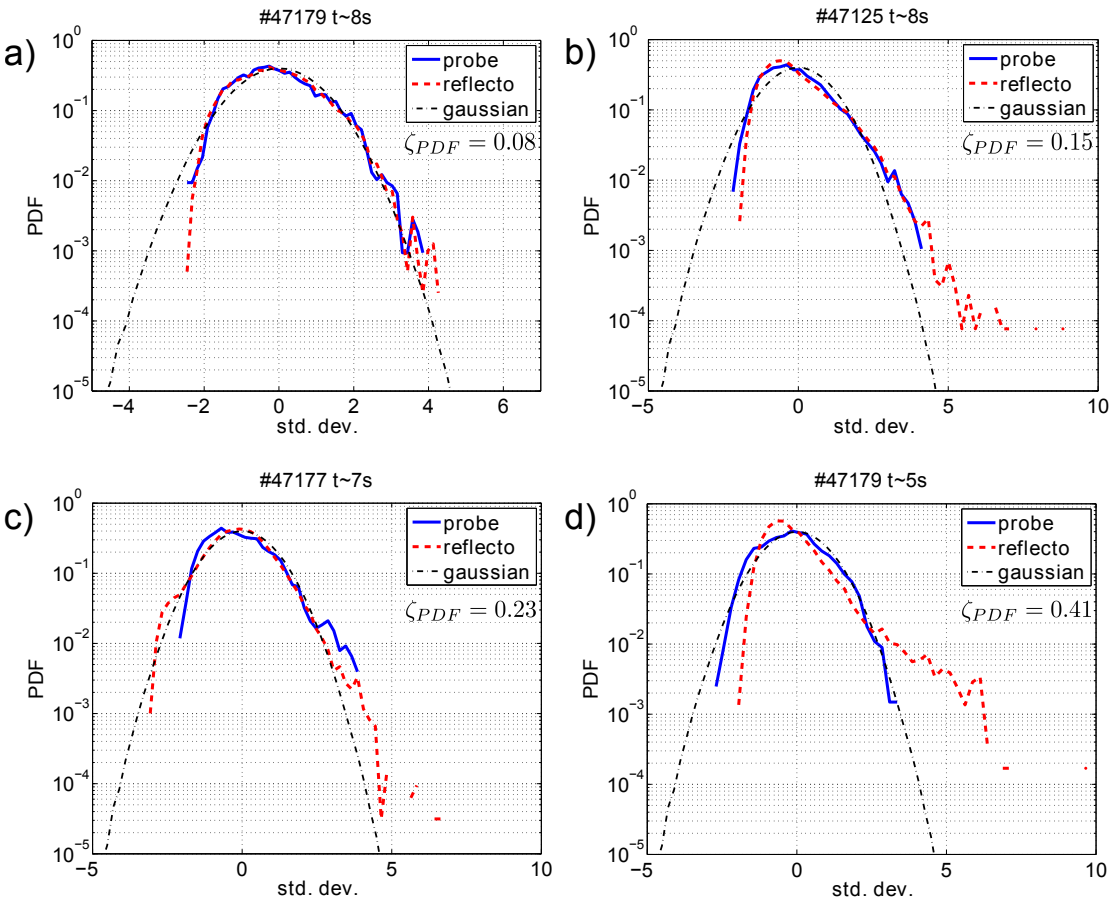

FIGURE 5.5: PDFs obtained on probe and reflectometer data measured around $d_{LCFS} \approx 1$, 1.8, 0.9 and 0.8 cm for a), b), c) and d), respectively. The PDFs are sorted in increasing order of ζ_{PDF} values.

5.3.3 Comparison of the fluctuation level profiles

The fluctuation level is defined as the ratio of the standard deviation to the mean value. In order to follow its radial evolution, the signals are windowed in intervals of 3 mm extent and the fluctuation level is computed on each interval. Fig. 5.6 shows the comparison of the fluctuation level profiles computed on probe and reflectometry data. Results have been sorted by their distances to the LCFS. The first case, a), corresponds to measurement for which d_{LCFS} is minimum, whereas the last case, p), corresponds to the case where d_{LCFS} is maximum. The fluctuation level values are about 30% percent. An overall good agreement is found between fluctuation levels measured by probe and reflectometry. No hierarchy has been identified between the probe and the reflectometer fluctuation level, i.e. the probe fluctuation level is not always larger nor smaller than that from the reflectometer.

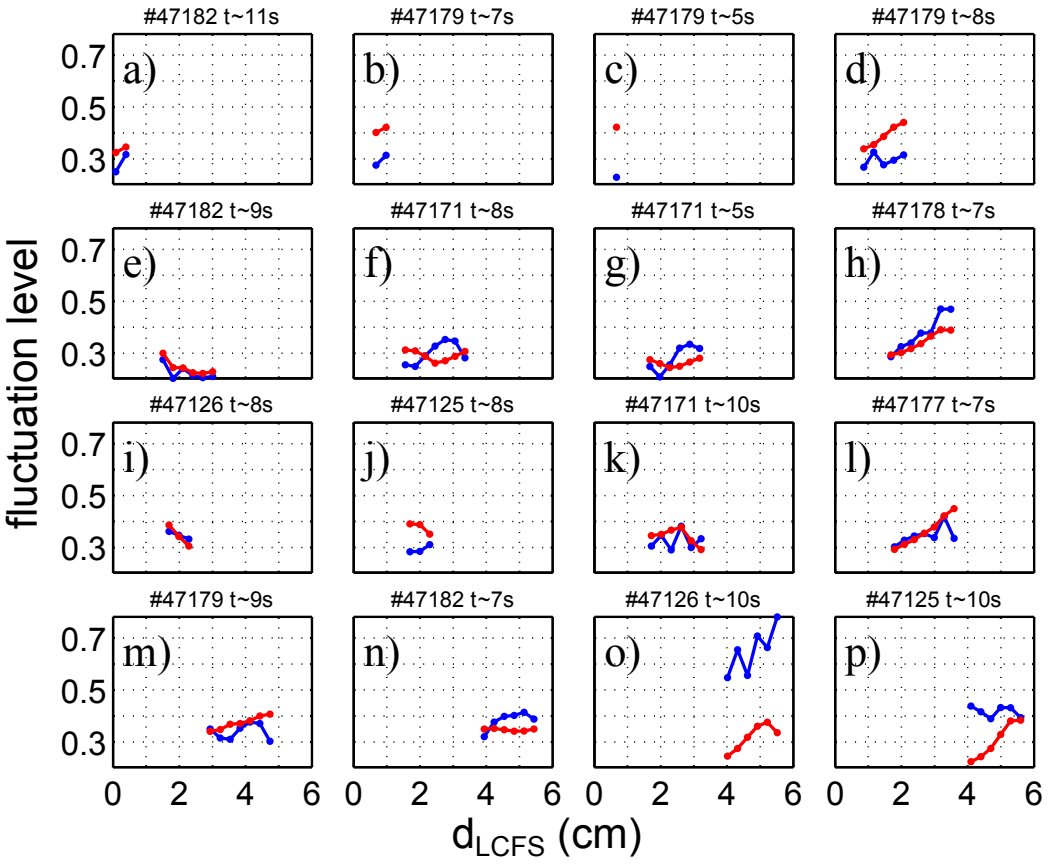

FIGURE 5.6: Radial profiles of the fluctuation level obtained from probe (blue curves) and reflectometry data (red curves). The results are sorted by their distance to the LCFS. Note that c) and p) are the datasets for which the PDFs do not agree.

5.3.4 Comparison of the skewness profiles

The skewness profiles have also been compared (Fig. 5.7). Again, results have been sorted by their distances to the LCFS. The skewness is a third order moment, subsequently the number of experimental points required for the convergence of the skewness can be substantially large. The statistical error on the skewness, due to a finite number of available experimental points, has been estimated for the probe data (see Appendix A). In spite of the limited length of the probe time series (around few thousands points), the statistical error is rather moderate and does not exceed 10% of the estimated skewness.

Even if several cases show qualitative discrepancies (e.g. Fig. 5.7 o)), the skewness measured by both diagnostics is in overall agreement, with positive values ranging between S≈0 and S≈2.

Numerous experimental works have reported an increase of the skewness with the distance to the LCFS [64–67]. The present results show similar trend on several single

discharges (Fig. 5.7 b), d) and j)-n)); however when considering the whole data set, no significant radial increase of the skewness is found.

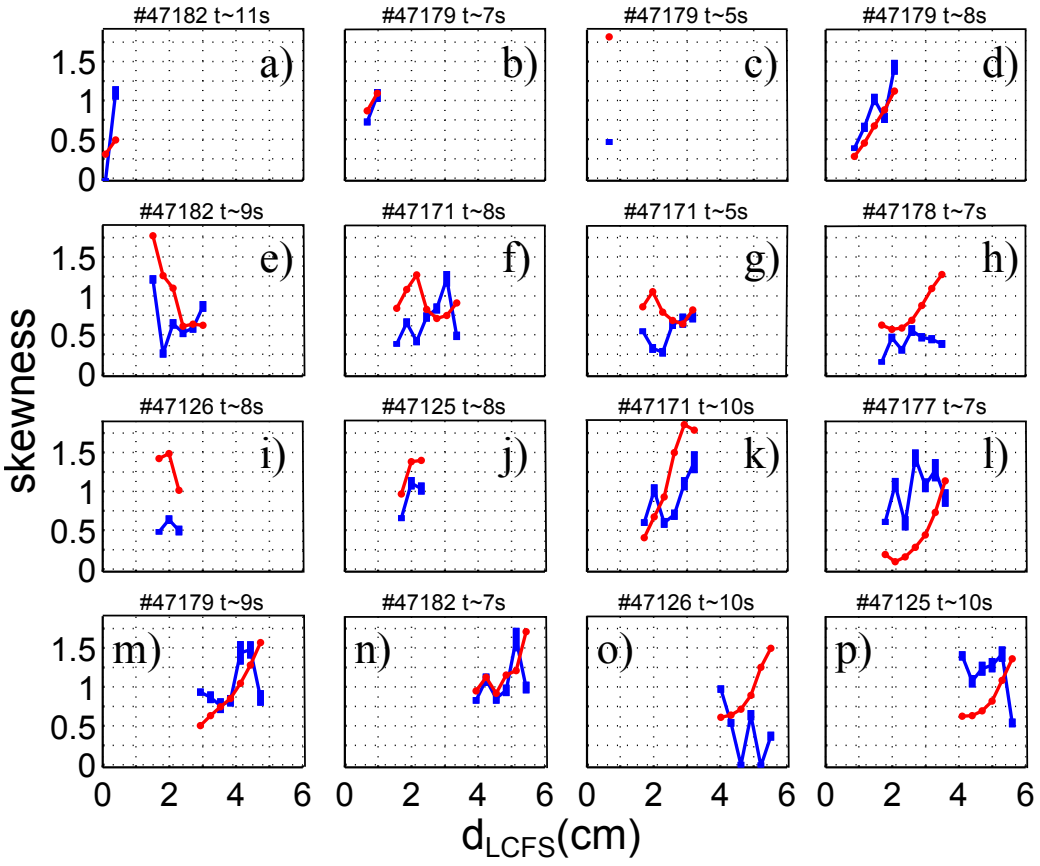

FIGURE 5.7: Radial profile of the skewness obtained from probe (blue curves) and reflectometry data (red curves). The results are sorted by their distance to the LCFS. Note that c) and p) are the datasets for which the PDFs do not agree.

5.3.5 Discussion

The statistical properties of the electron density fluctuations measured by the ultrafast sweeping reflectometer and the pecker probe are in good agreement. The non-Gaussian PDFs show an excess of positive values. This behavior is consistent with the paradigm of blobby transport for the SOL of a tokamak. The fluctuation levels agree remarkably well for all the dataset and each radial position. The estimated skewness was found to be positive on both the probe and reflectometer dataset. Nonetheless, the dispersion observed in the skewness values cannot be only explained by the finite length of the dataset.

The overall agreement of the statistical properties, which do not present any systematic shift of one diagnostic data with respect to the other, supports the idea of a weak impact of the temperature fluctuations on the ion saturation current fluctuations.

This idea can be easily understood if we consider the opposite case, i.e. a strong impact of the temperature fluctuations, and investigate its consequences on the fluctuation level. If $\tilde{n}_e$ and $\tilde{T}_e$ were in phase, then the fluctuation levels measured by the probe would be probably larger that than those measured by reflectometry. If $\tilde{n}_e$ and $\tilde{T}_e$ were out of phase, then the fluctuation levels would be likely lower than those measured by reflectometry.

5.4 Comparison of the temporal properties of the probe and reflectometer data

The analysis of the PDFs and the statistical moments is suitable to address the intermittency of the density fluctuations but does not contain information on the temporal dynamics of the turbulence. Consequently, the last step of this cross diagnostics investigation consists in estimating the characteristic time scales of the reflectometer and probe signals. This is done by analyzing the autocorrelation function (ACF), which is defined for an arbitrary time series $X(t)$ as

$$ACF_X(\Delta t) = \frac{\langle X(t)X(t-\Delta t)\rangle_t}{\sigma_X^2}. \tag{5.4}$$

5.4.1 Extraction of the time series

Ideally, the data used for the ACFs should be uniformly spaced in time and recorded at a fixed spatial position. Namely, the data should form a time series. This is not the case in practice but the data can be judiciously selected to approximately form a time series

Application to the probe data

The probe time series is straightforward to construct, it is the ion-saturation signal recorded between the deepest probe position r_{min}^{probe} and $r_{min}^{probe} + 3$ mm. Given that the probe signal is sampled at 1 MHz, 1 μs separates two successive probe measurements.

Application to the reflectometer data

The reflectometer time series are more tricky to build. First, it is worth to remind that the outputs of the reconstruction algorithm are $n_e(F,t)$ and $R(F,t)$. In order to obtain

data uniformly spaced in time, the frequency must be fixed. In this case, two successives data points are separated by 3 μs. However, as both $n_e(F,t)$ and $R(F,t)$ significantly evolve in time as discussed in Sec. 4.3 Fig. 4.7, successive data points can be separated by several centimeters. As the turbulence properties vary on a radial scale of the order of the centimeter in the SOL region, working at fixed frequency is problematic. It is wiser to work at fixed radial position even if the data are no longer uniformly spaced in time. To this end, the frequency index, for which the reconstructed radial position is the closest to a given radial position, is retained for each sweep. Concatenating the densities associated to the retained frequency index allows us to form the time series. With this method, the time interval between two successive data points can slightly vary. However, the time variation is of the order of 0.1 μs and will be neglected.

Fig. 5.8 shows examples of time series measured at $d_{LCFS} \sim 1.5$ cm. The time series have been normalized to facilitate the comparison.

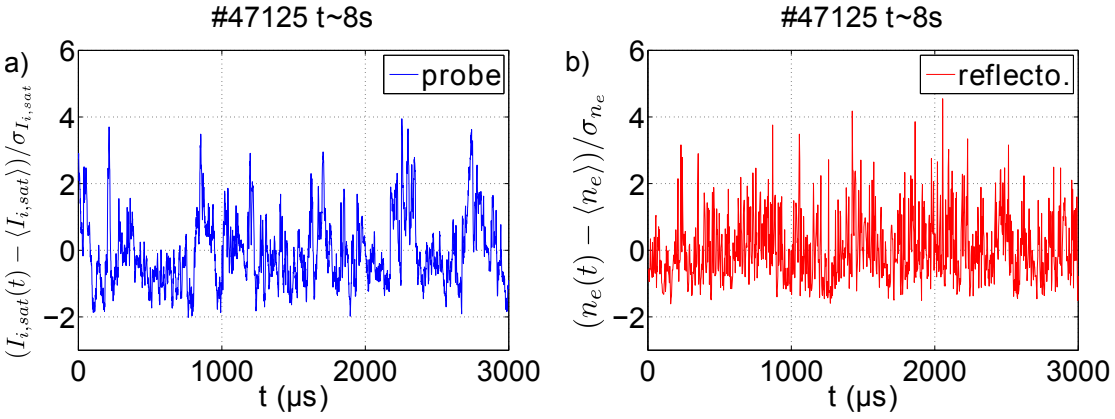

FIGURE 5.8: Example of probe and reflectometer time series obtained on #47125 at $t \sim 8$ s at the radial position $d_{LCFS} \sim 1.5$ cm.

The reflectometer time series oscillates much faster than the probe time series. A slower component is also observed on the reflectometer time series but its amplitude appears to be lower than the fast oscillating component.

5.4.2 Comparison of the autocorrelation functions

The ACF has been computed on the probe and reflectometer time series for each dataset. Fig. 5.9 shows 4 representative examples of ACFs obtained from probe and reflectometer data. The probe ACFs decrease much slower than the reflectometer ACF. This difference was observed on the whole dataset. The probe ACFs full width at half maximum (FWHM) ranges from around 20 μs to 50 μs whereas the reflectometer ACFs FWHM is always shorter than 6 μs.

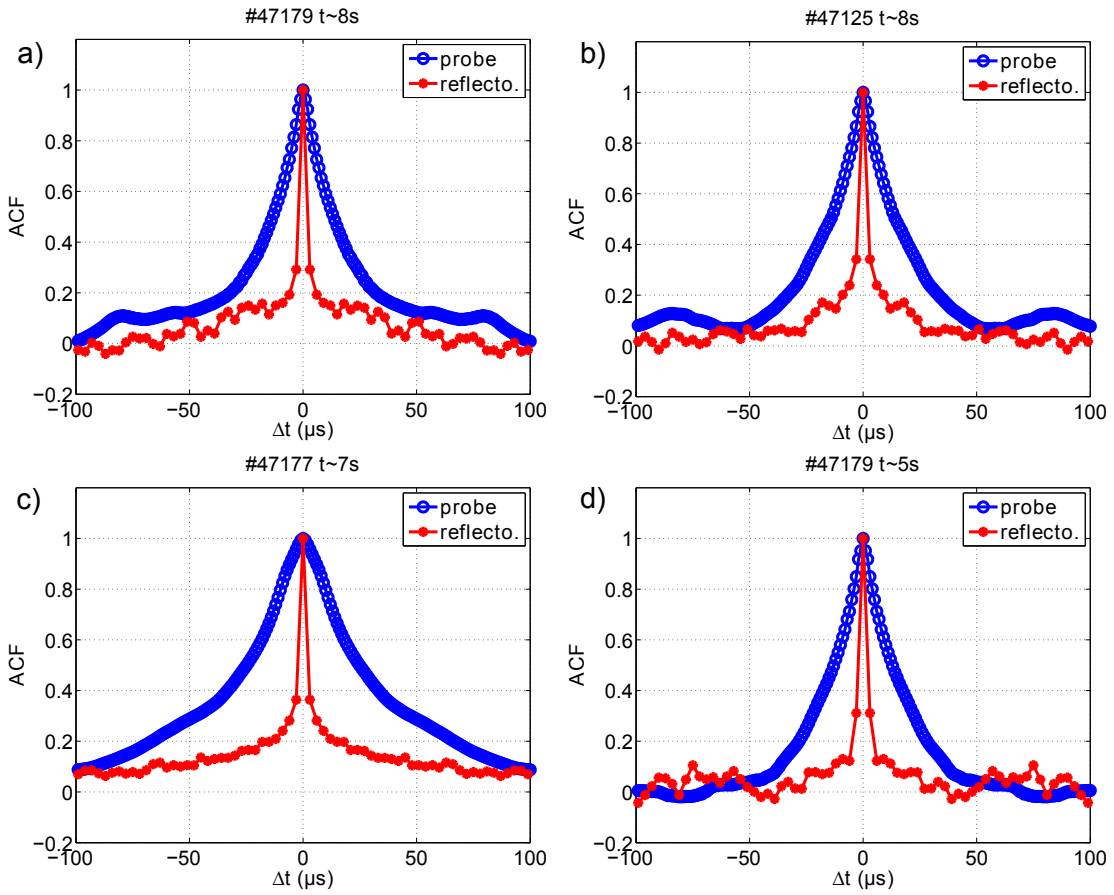

FIGURE 5.9: Examples of ACF obtained on probe and reflectometer data at $d_{LCFS} \sim$ 0.7 cm (a)), $d_{LCFS} \sim 1.5$ cm (b)), $d_{LCFS} \sim 0.7$ cm (c)) and $d_{LCFS} \sim 1.6$ cm (d)).

The probe ACFs decrease smoothly to zero while the reflectometer ACFs behave differently. The reflectometer ACFs drop sharply from 1 to low correlation values between $\Delta t = 0\ \mu s$ and $\Delta t = \pm 3\ \mu s$. Then, the reflectometer ACFs decrease slowly for increasing time lags. This behavior confirms the presence of two time scales mentioned in the last section. An uncoherent fast oscillating component might cause the Dirac-like central peak whereas slow variations of the signal may explain the smoother decrease of the ACF for larger time lags.

5.4.3 Discussion

In order to get an insight on the mechanism which might be liable for the fast fluctuations observed on the reflectometer data, it is worth to build a model for the reflectometer time series $X(t)$. The simplest model consists in expressing the time series as a coherent time series $S(t)$ corrupted by an additive incoherent white noise $\eta(t)$[2],

[2]Here, *noise* means all the components of the recorded signal that are not taken into account by our model. Given that the B-C algorithm uses a 1-D WKB description of the probing wave, phenomena such as multidimensional effects, Bragg backscattering, multi-reflections, instrumental errors, etc... enter in

$$X(t) = S(t) + \eta(t). \tag{5.5}$$

The ACF of X(t) is

$$ACF_X(\Delta t) = \frac{\langle (S(t) + \eta(t))(S(t + \Delta t) + \eta(t + \Delta t)) \rangle}{\sigma_X^2} \tag{5.6}$$

Assuming that $S(t)$ and $\eta(t)$ are independent variables and $\eta(t)$ has zero mean,

$$ACF_X(\Delta t) = \frac{\langle (S(t)S(t + \Delta t) \rangle + \langle \eta(t)\eta(t + \Delta t) \rangle}{\sigma_S^2 + \sigma_\eta^2}. \tag{5.7}$$

Finally, the ACF_X takes the form

$$ACF_X(\Delta t) = \frac{\sigma_S^2}{\sigma_S^2 + \sigma_\eta^2} ACF_S(\Delta t) + \frac{\sigma_\eta^2}{\sigma_S^2 + \sigma_\eta^2} ACF_\eta(\Delta t). \tag{5.8}$$

The ACF of the reflectometer time series is the pondered sum of the ACF of the coherent time series and that of the white noise. By definition, the white noise ACF equals unity for $\Delta t = 0$ and zero elsewhere.

This model is investigated numerically by generating the time series $S(t)$ and $\eta(t)$ with an exponential and a Dirac-like ACF, respectively [68]. The standard deviation of $S(t)$ and $\eta(t)$ have been set to σ_S=1 and $\sigma_\eta = \sqrt{3}$, respectively. Fig. 5.10 shows the ACFs computed on $S(t)$, $\eta(t)$ and $X(t) = S(t)+\eta(t)$. The ACF computed on the resulting time

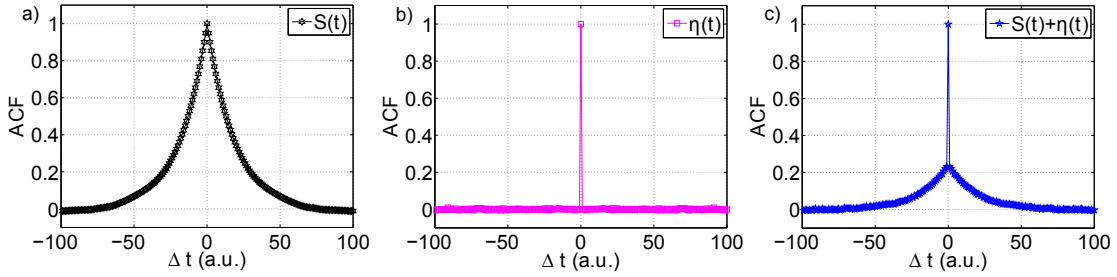

FIGURE 5.10: ACFs computed on numerically generated time series. a) coherent component ACF, b) white noise ACF and c) coherent component plus white noise ACF.

series $X(t)$ reproduces well the experimental features observed in Fig. 5.9. According to this model, the sharp decrease of the ACF computed on the reflectometer time series might be due to a white noise the amplitude of which is larger than the amplitude of the coherent time series ($\sigma_\eta > \sigma_S$).

the noise term. A priori, these parasitic phenomena are independent. According to the central limit theorem, it is then reasonable to model them with a Gaussian distribution.

Despite the simplicity of this model, it provides a possible scenario to explain the different time scales present on the reflectometer and the probe time series. Nevertheless, the properties of the scenario are highly dependent of the reflectometer signal decomposition.

The model can be refined by evaluating the PDF of the uncoherent component of the measured time series. To this end, the reflectometer signal is filtered to extract the coherent part of the signal. The parameters of the filter are choosen such as to obtain an ACF FWHM for the reflectometer signal similar to that of the probe signal.

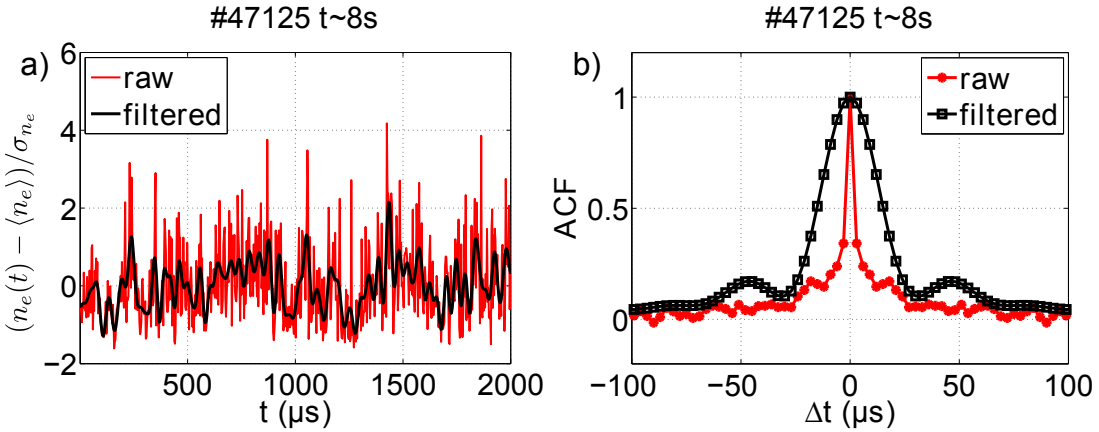

FIGURE 5.11: a) raw and filetred normalized density fluctuations time series obtained from reflectometry and b), the associated ACFs.

Fig. 5.11 shows a comparison of the raw and filtered reflectometer time series. Once the fast fluctuating component has been removed, the ACF significantly broadens. Interestingly, the filtered time series skewness is $S = 0.5$ whereas the original time series skewness is $S = 1.1$. By filtering the signal, the skewness is strongly reduced meaning that the fast fluctuating components should follow a positively skewed PDF in order to contribute significantly to the skewness of the time series.

The simplest decomposition was chosen, namely the reflectometer time series was separated into a fast and a slow component. However, others choices for the decomposition might lead to different scenarios. In summary, the underlying mechanism should have a signature η with the following properties

- a time scale much smaller than the density fluctuation time scale estimated from the probe time series,
- an amplitude of the order of the amplitude of the coherent component of the time series,
- a non-Gaussian positively skewed probability distribution.

A major assumption underlies the reflectometric reconstruction of the density profile. The reflectometer measurement is assumed to be well localized both radially and poloidally. This is partially true given that the reflectometer signal comes not only from the reflection of the probing waves at the cutoff layer but is also Bragg backscattered in front of the cutoff layer. In Appendix A, the poloidal size of the beam spot is estimated to 20 cm, which is larger than the characteristic size of the density fluctuations. Consequently, the reflectometer signal is not localized poloidally. On the contrary, the probe measurements are almost ponctual given that the size of the collectors is millimetric.

A plausible scenario can be built by associating the coherent and incoherent components of the time series to the localized (reflection at the cutoff layer) and unlocalized (back scattering and 2D effects) parts of the reflectometer signal, respectively. This scenario could explain why the fast fluctuations are observed on the reflectometer but not on the probe time series. The multidimensional effects might lead to a randomization of the reflectometer signal which is consistent with the very fast fluctuations of the time series. If the multidimensional effects are cumulative, the amplitude of the incoherent signal may be similar to the amplitude of the coherent signal. However, it is not clear why multidimensional effects should lead to a non-Gaussian positively skewed noise.

5.5 Summary

In order to validate the assumptions underlying the interpretation of reflectometer and probe measurements, the electron density profiles and its fluctuations obtained from both diagnostics have been compared. The comparison was performed on the basis of 16 independent datasets measured in the Tore Supra SOL during Ohmic discharges. The analysis has covered several properties of the electron density, namely the density profile, the statistical properties (PDFs, fluctuation level and skewness profiles) and the autocorrelation functions.

The density measured by the probe was found to be systematically larger than the density measured by reflectometry. The probe density evaluation requires an assumption on the ion temperature. The possibility of an underestimate of the ion temperature was explored but does not appear sufficient to explain the inconsistency between the density profiles measured by both diagnostics.

The analysis of the electron density fluctuations through the probe ion-saturation current fluctuations is based on the assumption of negligible electron temperature fluctuations. The good agreement between the statistical properties of $\tilde{I}_{i,sat}$ and $\tilde{n}_e^{reflecto.}$ tends to confirm the assumption that $\tilde{I}_{i,sat}$ is not significantly affected by $\tilde{T}_e$. A numerical and

experimental study performed with a gyrofluid turbulence code has reported similar conclusions [69].

The temporal properties of the probe and reflectometer data have been investigated using the autocorrelation functions. The reflectometer ACFs significantly differ from the probe ACFs. This difference was attributed to the presence of a fast fluctuating component on the reflectometer time series. The origin of the fast fluctuating component is possibly linked to multidimensional effects, which arise only on the reflectometer signal.

It is, somehow, challenging to conciliate the discrepancies of the temporal properties of $\tilde{I}_{i,sat}$ and $\tilde{n}_e^{reflecto.}$ and the good agreement of the statistical properties of the latter quantities. The arguments developed in this chapter were based on an idealized description of the interactions of the diagnostics and the SOL plasma turbulence. Consequently, only the leading order effects, which might explain the differences between both diagnostics, have been addressed. A more complete picture should emerge by inserting synthetic Langmuir probe and reflectometer diagnostics in a turbulence code. In order to validate the conclusions of this study, the turbulence code should describe, at least, the evolution of the electron density and temperature as well as the ion temperature in the tokamak SOL region on time scales relevant to experience, namely few milliseconds.

Chapter 6

Turbulence correlation properties measured on Tore Supra Ohmic discharges

In the first part of this work, attempts have been made to quantify the electron density fluctuation properties from the reconstructed density profiles. These attempts have been moderately successful. One of the main problems is related to the shifts of the profiles which make impossible to investigate the turbulence properties in the closed magnetic field lines region.

Consequently, a new approach is adopted here: the turbulence properties are investigated through a correlation analysis applied to the reflectometer raw signals.

The analysis of the correlation properties of reflectometer signals were generally done using two-frequencies reflectometry (correlation reflectometry) [70–76].
The sweeping reflectometry system allows us to obtain continuous radial correlation profiles during a single discharge whereas standard correlation reflectometry only provides discrete measurements. It has though to be noted that the sweeping reflectometry technique can be used as far as the turbulence is frozen during the sweeping time.

In this chapter, the temporal and spatial correlation properties of the raw fluctuating data have been analyzed from the far SOL to the core plasma region in Tore Supra Ohmic discharges. In particular, the correlation analysis was performed on each component of the reflectometer signals, namely the amplitude, phase, real and imaginary parts and the full complex signal. This part of the study aims at sheding some light on the actual debated question of which reflectometer signal better performs the turbulence correlation properties.

Previous experimental and numerical studies have addressed this issue. By comparing Langmuir probes and reflectometer data measured on the CCT tokamak in the presence of strong fluctuations [77], a close correspondence was obtained between the correlation length measured on the $Acos(\phi)$ signal and the ion saturation current. Numerically, turbulent cut-off layers have been modeled by broadband random fluctuations. In the first attempts, the wave-plasma interaction was described with simplified models, namely WKB approximation [78] and physical optics [79]. It was found that the $A\cos(\phi)$ signal better estimates the turbulence correlation length than the phase or the amplitude signals. More recently, a 2D full-wave code was used to simulate O-mode reflectometry [80]. The amplitude correlation length was there found to be in good agreement with the turbulence correlation length for low fluctuation levels (linear regime). At higher fluctuation levels, the correlation lengths appeared to be better estimated from the $A\cos(\phi)$ signal. Overall, the numerical studies have reported that the correlation lengths obtained from the reflectometer signals tend to underestimate the turbulence correlation length at high fluctuation level. This underestimate was also found analytically [81].

The chapter is divided as follows. First, the methods used for the determination of the fluctuations radial sizes, namely the cross-correlation and the coherency, are presented. Then, the correlation and the coherence length profiles computed on the different components of the signal are compared. The impact of MHD activity on the coherence length is also considered. Finally, the turbulence correlation properties measured in the edge and SOL regions are discussed in detail.

6.1 Signal analysis

We remind that the complex signal measured and recorded by the reflectometer at time t is expressed as:

$$S(F,t) = A(F,t)e^{i\phi(F,t)},$$

where A and ϕ are the amplitude and phase of the signal, respectively. F is the probing signal frequency.

The first step is to link the probing frequencies to the associated radial cut-off positions. To this end, the knowledge of the electron density profile is required. As largely detailed in Chap. 4, the electron density profile is reconstructed for each frequency sweep according to the B-C recursive algorithm [25, 82]. The radial dependence of the cut-off frequencies is given from the mean density profile which is obtained by averaging over the N sweeps acquired during a single burst. Then, the frequency dependence of the reflectometer signal is replaced by the radial dependence.

Each component of the reflected signal can be written as the sum of an unperturbed and a fluctuating part associated to the mean density profile and the plasma density fluctuations, respectively.

$$\delta X(r,t) = X(r,t) - \langle X(r)\rangle_t. \tag{6.1}$$

Here, $X(r,t)$ denote any component of the reflected signal, namely either the full complex signal, the real or imaginary part, the phase or the amplitude.

6.1.1 Cross-correlation

Quantitative properties of the signal fluctuations are extracted through a cross-correlation analysis. The cross-correlation function (CCF) evaluates the similarity between data measured at different positions and times. The $CCF(r,\Delta r,\Delta t)$ computed on two time series $X(r,t)$ and $X(r+\Delta r, t+\Delta t)$ measured at different positions reads:

$$CCF(r,\Delta r,\Delta t) = \frac{\langle [X(r,t) - \langle X(r)\rangle_t][X(r+\Delta r, t+\Delta t) - \langle X(r+\Delta r)\rangle_t]\rangle_t}{\sigma_{X(r)}\sigma_{X(r+\Delta r)}}, \tag{6.2}$$

$\langle X(r)\rangle_t$ and $\sigma_{X(r)}$ denote the mean and standard deviation, performed over the time series measured at the position r. The CCF is meaningful if the fluctuation time scale is much shorter than the time series length. The CCF computed for Δr=0 is the autocorrelation function (ACF). The correlation time t_{corr} is defined as the ACF FWHM. Reliable correlation times can be obtained only if there are at least 3 experimental points on the ACF above 0.5. Given that the time resolution is 3 μs, the lowest accessible correlation time is thus $t_c = 6\ \mu$s.
The radial correlation length is defined as the CCF FWHM for $\Delta t = 0$. In practice, the correlation time and length are calculated by linearly interpolating the CCF around 0.5. The relation between the correlation length and time is discussed in Sec. 6.3.

Fig. 6.1 shows an example of the CCF computed on the signal amplitude.

In this example, the CCF contour levels are positively tilted in the $(\Delta r, \Delta t)$ plane. This tilt is a consequence of radially outward propagating fluctuations. The time lag Δt for which the CCF peaks, satisfying $\Delta t \neq 0$ and $CCF(r,\Delta t,\Delta r) \geq 0.5$, is identified. If at least 10 experimental points fulfill the previous condition, a linear fit of the curve $\Delta r = V_{corr}\Delta t$ is performed to obtain the radial velocity V_{corr}. Fig. 6.2 illustrates the procedure used to estimate the radial velocity on the amplitude data.

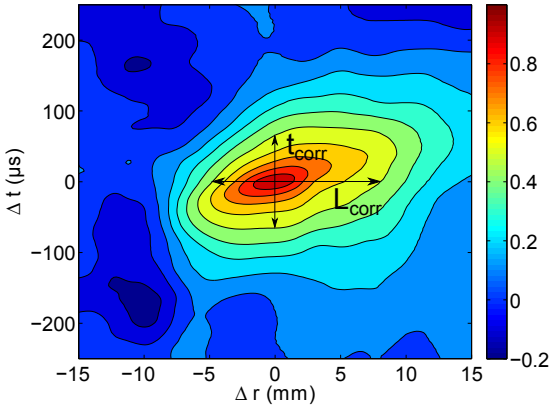

FIGURE 6.1: Contour plot of the amplitude cross-correlation function, for Tore Supra Ohmic shot #47170 measured 7 cm outside the LCFS. The correlation time t_{corr} and length L_{corr} are represented by arrows.

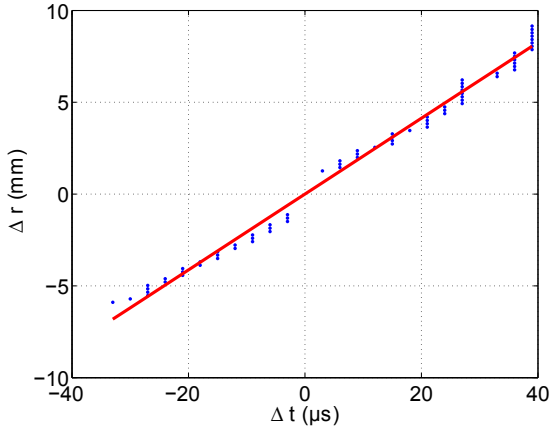

FIGURE 6.2: Position of the time lags (blue dots) where the amplitude CCF peaks, for Tore Supra shot #47170 measured 7 cm outside the LCFS. Only time lags verifying $\Delta t \neq 0$ and $CCF(r, \Delta t, \Delta r) \geq 0.5$ are kept. The red line is the linear fit from which the radial velocity is estimated.

6.1.2 Coherency

If X is a complex variable, it is more convenient to work with the Fourier transform of the $CCF(r, \Delta r, \Delta t)$ called coherency

$$\gamma(r, \Delta r, F) = \frac{\langle P_{X_r X_{r+\Delta r}} \rangle}{(\langle P_{X_r X_r} \rangle \langle P_{X_{r+\Delta r} X_{r+\Delta r}} \rangle)^{1/2}}. \tag{6.3}$$

Here $P_{X_r X_{r+\Delta r}}$, $P_{X_r X_r}$ and $P_{X_{r+\Delta r} X_{r+\Delta r}}$ are the cross and auto power spectra computed on the time series $X(r,t)$ and $X(r+\Delta r, t)$. The power spectra are computed with sliding FFTs on 128 points windows with 50 overlapping. Here, $\langle \cdot \rangle$ denotes the average performed over 40 spectra. The coherency gives information on the correlation of each

frequency included in the time series. Consequently, a radial coherence length defined as the coherency full width at half maximum can be calculated for each frequency. To avoid any confusion, the subscripts *coh* and *corr* are used when we refer to a quantity computed with the coherency and the CCF, respectively.

Fig. 6.3 shows an example of the coherency computed on the complex signal. On this example the coherence lengths are larger at low frequencies and decrease slightly when the frequency increases.

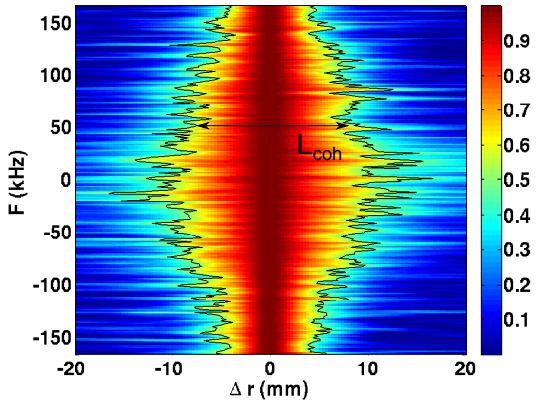

FIGURE 6.3: Contour plot of the coherency computed on the complex signal in the core plasma ($\rho \sim 0.4$) of the Tore Supra Ohmic shot #47475. The coherence length L_{coh} is represented by an arrow.

The coherence analysis has been applied to the full complex signal whereas correlation analysis has been applied to the amplitude A, phase ϕ and the real part of the reflectometer signal $Acos(\phi)$ (in the literature often referred to as the homodyne signal [78, 79]). Separate analysis of the amplitude and the phase has been performed as they contain different plasma fluctuation properties. The differences between the phase and amplitude signals can be though as follow: the amplitude better accounts for the 2D (two dimensional), i.e. poloidal and toroidal, mirror reflecting effects, while the phase accounts for the density profile deformation and mostly refers to a 1D radial effect. The complex and homodyne signals are sort of mixes of both phase and amplitude.

6.2 Application to Tore Supra Ohmic discharges

Correlation measurements obtained on Tore Supra Ohmic discharges are presented. First, we show how the fluctuation length profile can be computed over the whole radius. It is then highlighted how MHD activity could impact the determination of the coherence lengths. Finally, the correlation properties are analysed in detail in the edge and SOL plasma, over a discharge which provides better statistics.

In the following, core ($\rho < 0.7$) and edge ($0.7 \leq \rho < 1$) refer to closed magnetic field lines regions, whereas SOL ($\rho \geq 1$) refers to the region outside the LCFS. The radial position is labelled by the normalized toroidal flux coordinate ρ for data mostly obtained in the closed magnetic field lines region whereas the distance to the LCFS d_{LCFS} is used in the SOL.

6.2.1 Radial correlation length profile

Tore Supra shot #47475 is a low magnetic field ($B = 3$ T) Ohmic discharge. In these conditions, the accessibility of the reflectometer measurement can cover the plasma from about $\rho \approx 1.2$ to around $\rho \approx 0.3$ and provide a complete density profile from the far SOL to the core region (Fig. 6.4 a). Fig. 6.4 b) shows the complex signal power spectra at two different radial positions as well as the noise level, the latter being well above the plasma signals. In the core plasma at $\rho = 0.5$, the spectrum is dominated by frequencies in the range -50 kHz $\leq$ F $\leq$ 100 kHz and falls rapidly for higher frequencies. In the edge plasma, at $\rho = 0.8$, the spectrum is flatter. The flattening of the power spectrum might be related to the increase of the fluctuation level, which raises from around $\delta n_e/n_e \approx 0.8\%$ at $\rho = 0.5$ to about $\delta n_e/n_e \approx 2\%$ at $\rho = 0.8$ (Fig. 6.4 a), black curve). Here, the fluctuation level was computed as in [54].

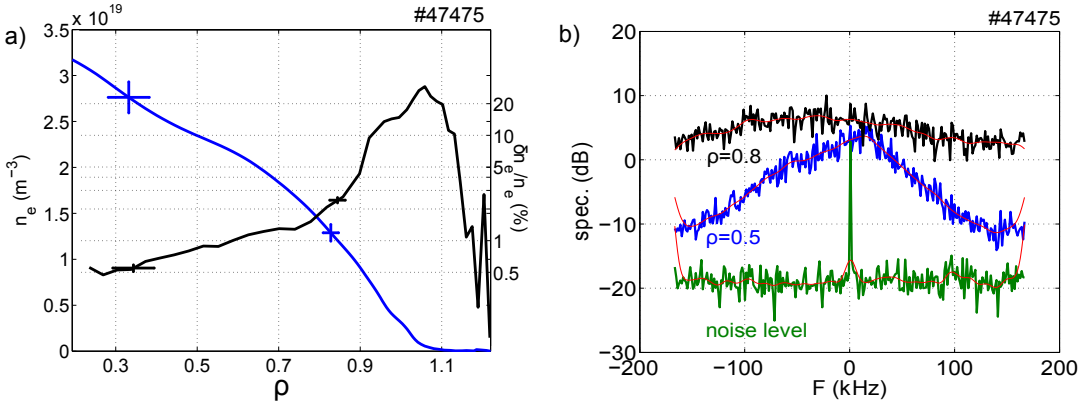

FIGURE 6.4: a) mean electron density profile. The fluctuation level is superposed in full black line. The uncertainties, quantified by the standard deviation, are shown for two radial positions. b) Complex signal power spectra computed at $\rho = 0.5$ (blue curve) and $\rho = 0.8$ (black curve). The spectral characteristics of noise are also shown (green curve).

3000 frequency sweeps were performed during a burst. During the acquisition, the mean electron density $< n_e >= 1.98 \times 10^{19}$ m^{-3}, the plasma current $Ip = 0.7$ MA and the magnetic field $B_0 = 3.08$ T were kept constant. Fig. 6.5 shows the radial and temporal dependence of the normalized A , ϕ and $Acos(\phi)$ signals measured around t=3 s. The

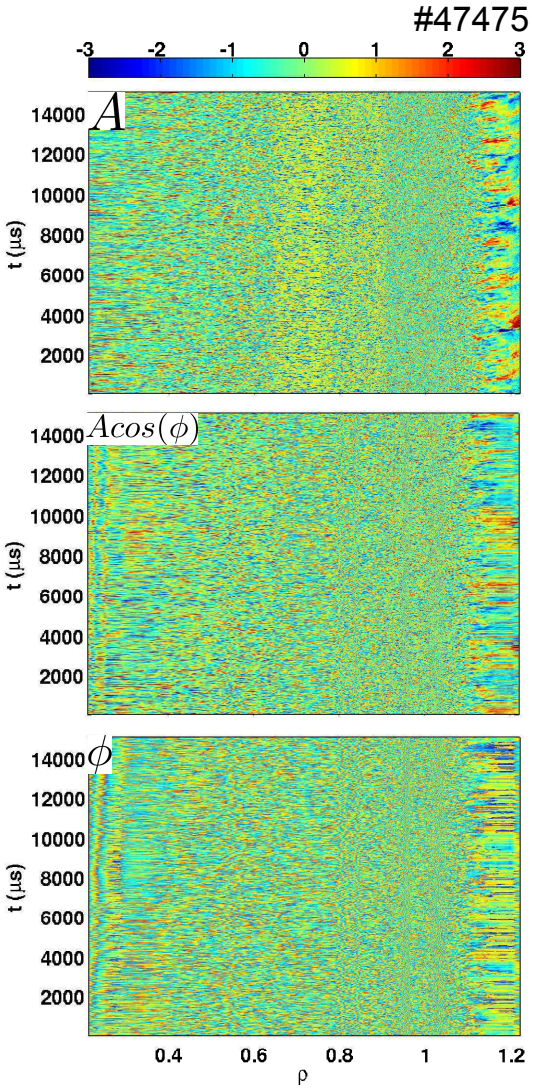

FIGURE 6.5: Normalized amplitude (top), real (middle) and phase (bottom) signals with respect to the normalized radial position and time.

signals have been normalized by subtracting the mean value and dividing by the standard deviation to weight the different plasma regions consistently. For this discharge, the connection between the V- and W-band signals occurs at about $\rho = 0.9$.
In the far SOL the data present large turbulent structures propagating outwards which are better seen on the amplitude rather than on the phase signal. On the opposite, in the plasma core an MHD tearing mode (the central q=1 rational surface is hardly covered by the reflectometer) has a stronger influence on the phase. The effect of MHD activity will be discussed more precisely in the following relating to another plasma discharge.

Fig. 6.6 shows a comparison of the radial evolution of the coherence and correlation lengths from the far SOL to the core plasma. The coherence lengths are measured on the full complex signal whereas the correlation lengths are measured on the amplitude

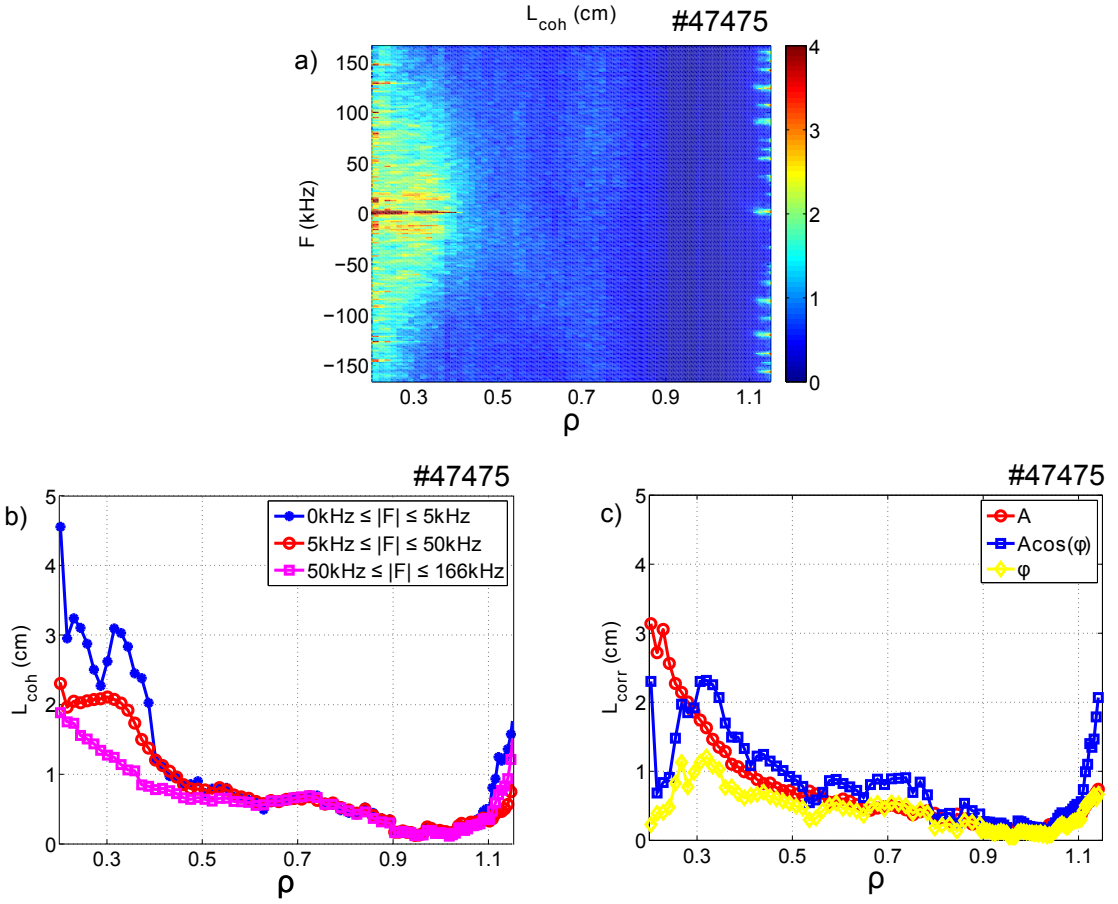

FIGURE 6.6: a) Coherence lengths with respect to the signal frequency and radial position. b) Radial profiles of the coherence lengths averaged on three distinct frequencies intervals. c) Radial profiles of the correlation lengths computed on the amplitude, real part and phase signal.

phase and real part of the signal. Both coherence and correlation lengths decrease from the centimeter range in the core plasma to millimetric at the LCFS and increase again in the SOL plasma. It is worth noting that the continuity between the reflectometer V and W bands is well recovered. The frequency dependence of the coherence lengths is depicted on Fig. 6.6 a). In between $\rho = 0.4$ and $\rho = 1.1$, no difference is observed on the coherence length for any frequency component. For $\rho \leq 0.4$, the coherence lengths associated to low frequency components are clearly larger than the coherence lengths associated to high frequencies. Fig. 6.6 b) shows the coherence lengths averaged on three distinct frequency intervals: $|F| = [0 : 5]$ kHz, $|F| = [5 : 50]$ and $|F| = [5 : 166]$ kHz. The radial profiles of the coherence and correlation length are in close agreement for $\rho > 0.4$, whereas reflect the presence of MHD modes in the inner region. In the latter region, the coherence analysis is more appropriate allowing to separate the contribution of the different frequency components as, it will be further investigated in the following subsection.

In the outer core, edge and SOL plasmas, coherence or correlation methods can be equivalently used for the estimate of the fluctuation characteristic scales.
A detailed analysis of the edge region is presented in subsection 6.2.3 taking advantage of a discharge where larger statistics and a comparison with fixed frequency reflectometer data are available. In the above an implicit assumption of locally frozen turbulence was used, which will also be proven on that same shot.

6.2.2 Effect of MHD activity on the correlation lengths in the core plasma

This section aims at investigating how the correlation lengths are affected by MHD modes.
As the MHD modes are active in the core region, we need to work with low density plasma in order to probe the plasma up to the central region. Tore Supra shot #47537 meets this specifications and was thus used here. 10.000 reflectometer sweeps were performed corresponding to 30 ms acquisition. During the sweep, the mean electron density $\langle n_e \rangle = 6.3 \times 10^{18}$ m^{-3}, the plasma current $Ip = 0.6$ MA and the magnetic field $B_0 = 3.38$ T were kept constant. Fig. 6.7 shows the radial dependence and temporal evolution of the normalized A , ϕ and $Acos(\phi)$ signals.

The core plasma, is often characterized by a substantial MHD activity related to tearing modes which is well recorded by the reflected signals [83, 84]. The q profile computed with the CRONOS integrated modelling suite code [85] has been superimposed to locate rational surfaces to give a complementary and necessary information about the position of rational surfaces. It is essential for their identification and the understanding of the perturbed reflectometry data.
The data around the $q = 1$ rational surface exhibit a complex radial and temporal evolution. Fast oscillating tearing modes at 2 kHz are clearly visible on both sides of the plasma center between 10 and 15 ms with an additional sawtooth crash just after 15 ms. A first sawtooth crash also occurred at the very beginning of the data acquisition, consistently to the electron cyclotron emission (ECE) signal from which a sawtooth period of approximately 15 ms is obtained. Moreover, the sawtooth crashes locally trigger an MHD activity at the neighbouring rational surfaces $q = 3/2$ and $q = 2$ as previously observed [86].
In order to separate the contribution of the MHD and microturbulence to the coherence lengths, those were computed on 2 frequency intervals $|F| = [0 : 5]$ kHz, $|F| = [5 : 166]$ kHz. Fig. 6.8 shows that the coherence lengths at low frequency, which are related to MHD are up to two times larger than those at higher frequencies. Interestingly, a reduction of the low and high frequencies coherence length profiles are observed around

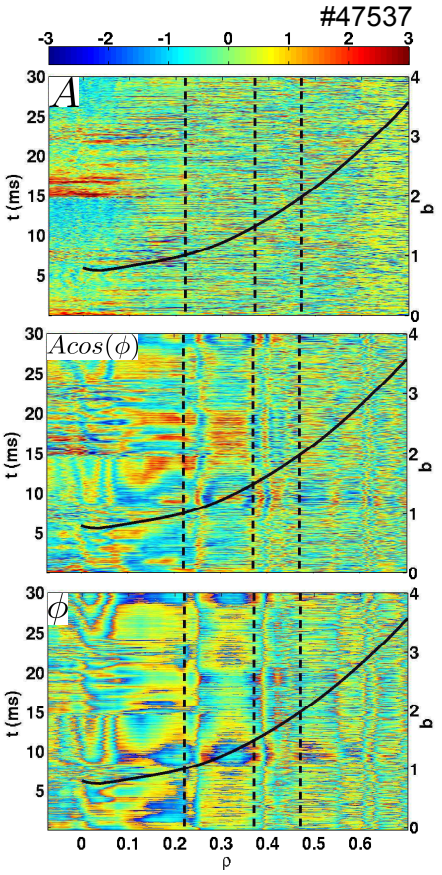

FIGURE 6.7: Normalized amplitude (top), real (middle) and phase (bottom) signals with respect to the normalized radial position and time in the core region. The q profile (black line) is also represented. The positions of q=1,3/2 and 2 rational surfaces are indicated by dashed-lines.

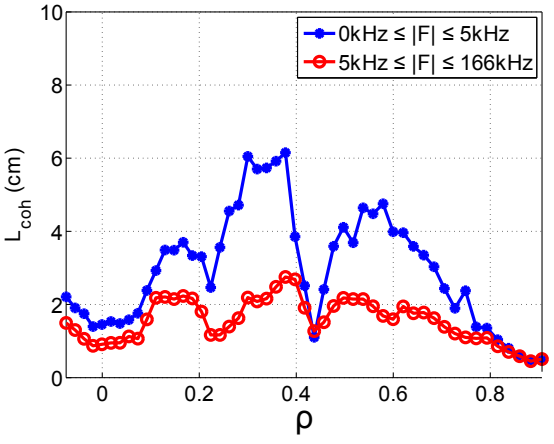

FIGURE 6.8: Coherence lengths computed on the complex signal for two distinct frequency intervals (#47537).

the rational surfaces $q = 1$ and $q = 2$. This might result from an interplay between turbulence and MHD activity which remains to be investigated in a future work.

6.2.3 Edge and SOL regions

In this subsection, special attention is paid to the edge and SOL region turbulence properties. This is done by analyzing data from the Tore Supra Ohmic discharge #47170. The plasma lasted 15 s and was in steady state from t=4 to t=12 s. During the steady state operation, the mean electron density $< n_e >= 2.1 \times 10^{19}$ m^{-3}, the plasma current $Ip = 1$ MA and the magnetic field $B_0 = 3.7$ T did not vary more than 5%. Three successive reflectometer bursts were realized at times t=5, 7.5 and 10 s which can thus provide an interesting set of separate and independent measurements for the statistical analysis. Fig. 6.9 shows the mean electron density profile. The fluctuation level profile

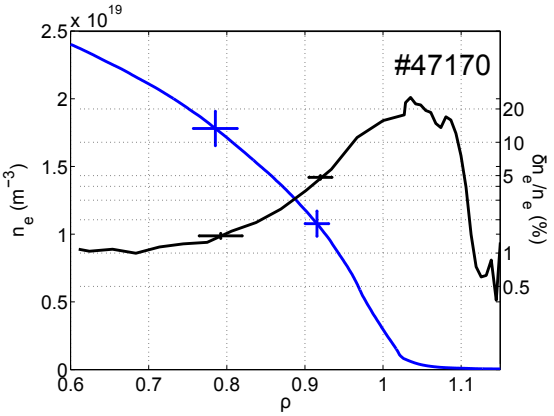

FIGURE 6.9: Mean electron density around t=5 s. The fluctuation level is superposed in full black line. The uncertainties, quantified by the standard deviation, are shown for two radial positions.

computed as in [54] is also shown and will be used for discussion.
Each burst has 3000 sweeps which corresponds to 9 ms of measurement time. For each burst at a given radial position, the CCF are independently computed on the 9 ms time series. Therefore, three L_{corr}, t_{corr} and V_{corr} measurements are available to quantify the variation of the results over the plasma radius.

Edge plasma

First the correlation time is studied in the edge plasma. Fig. 6.10 shows that the sweeping reflectometry ACF (black curve) computed at $\rho = 0.64$ drops very quickly to the noise level. It is interesting to compare this result with fixed frequency reflectometry data. The

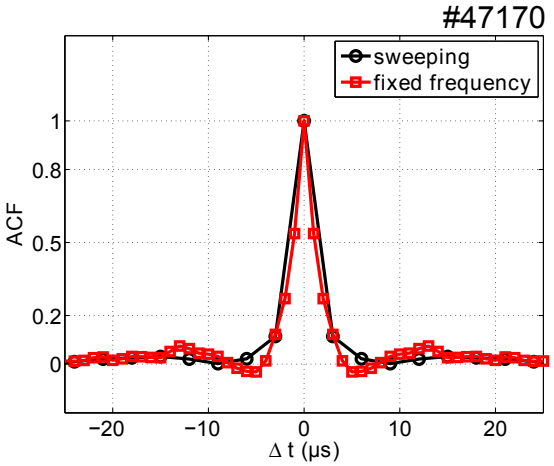

FIGURE 6.10: Comparison of the amplitude ACF function computed at $\rho = 0.64$ around t=7.5 s between sweeping reflectometry (3μs sampling time) and fixed frequency reflectometry (1 μs sampling time) data.

ACF measured with the fixed frequency reflectometer system (red curve) operating with a 1 MHz sampling rate shows only three experimental points before reaching the noise level. The correlation time obtained from fixed frequency reflectometry is $t_c = 2.3\ \mu$s. This comparison suggests that the Dirac-like ACF measured by ultrafast sweeping reflectometry does not result from a white noise signal but from an insufficient time resolution. Note that, contrary to the core plasma region in presence of MHD activity, the characteristic fluctuation time scale in the edge and SOL region is much shorter than the length of the time series; this stationary turbulence condition justifies the applicability of the cross-correlation technique to evaluate the correlation length.

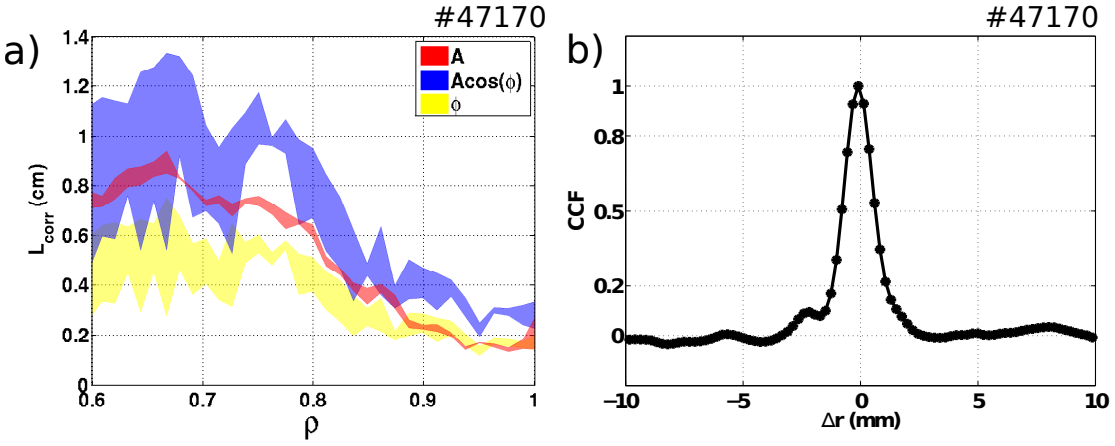

FIGURE 6.11: a) Correlation lengths computed in the edge region on the amplitude, real and phase signal. For each signal, the shaded area in between the maximum and minimum correlation length represents the dispersion of the results. b) Amplitude CCF computed at $\rho = 0.95$ around t=5 s.

Fig. 6.11 a) shows the radial dependence of the correlation lengths computed on A, $Acos(\phi)$ and ϕ. The turbulence must be locally frozen to measure reliable correlation lengths. A plasma region of 40 cm of radial extent is swept in 2 μs, the largest structures are therefore swept in 0.1 μs which is much shorter than the local correlation time.
As already observed in Sec. 6.2.1 , the amplitude, phase and real signal correlation lengths show similar behavior as they decrease from the edge to the LCFS. It is worth noting that at $\rho = 0.95$, where the correlation length is minimal, the CCF measured by the sweeping reflectometry is still resolved, as illustrated in Fig. 6.11 b).

The amplitude, real and phase correlation lengths rapidly decrease above $\rho = 0.8$ up to $\rho \approx 0.9$. The drop of the correlation length might originate from two distinct effects. On one hand, the estimated correlation lengths can be artificially reduced due to the high fluctuation level in the edge plasma (see Fig. 6.9, black curve) as discussed in the introduction. On the other hand, velocity shear can tear apart the turbulent structures, thus leading to a decrease of the correlation lengths. In order to investigate this latter effects , the perpendicular velocity measured by Doppler reflectometry (Sec. 2.2.2) is used and shown in Fig. 6.12. For $0.85 < \rho < 0.95$, the plasma rotates in the electron diamagnetic direction with a velocity of the order of 4 km.s^{-1}. Around $\rho \approx 0.95$, the perpendicular velocity drops by more than a factor two leading to a strong velocity shear. The location of the strong velocity shear is not consistent with that of the drop of the correlation length. Consequently, the velocity shear might have only little influence on the radial decrease of the correlation lengths, this is most probably due to an increase of the fluctuation level.

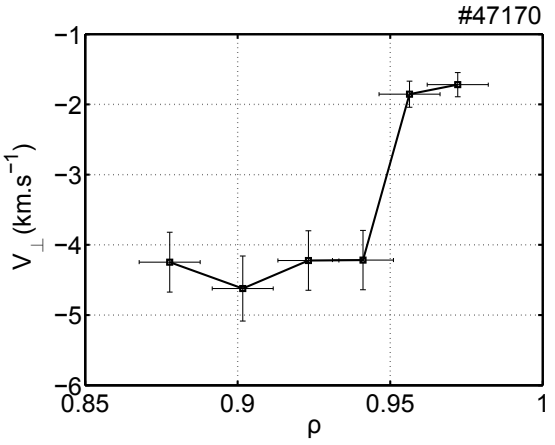

FIGURE 6.12: Radial profile of the perpendicular velocity measured by Doppler reflectometry.

SOL plasma

As mentioned above (Sec. 6.2.1), propagating structures in the SOL are better seen on the amplitude signal thus only this signal is used to characterize the fluctuation in the SOL. The correlation time is lower than 6 μs close to the LCFS and grows almost exponentially between $d_{LCFS} = 3$ to 7 cm (Fig. 6.13). Further outwards, t_{corr} stays almost constant with values around 100 μs.

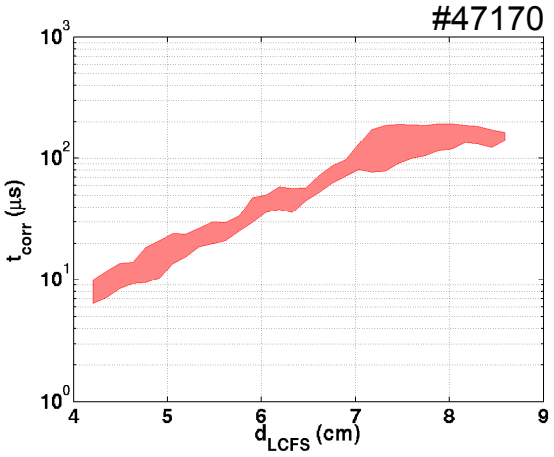

FIGURE 6.13: Amplitude correlation time in the SOL with respect to the distance to the LCFS (d_{LCFS}). The shaded area, in between the maximum and minimum correlation time, represents the variation of the results during the three bursts of sweeps.

Fig. 6.14 depicts the radial dependence of the correlation length of the amplitude signal, which increases from about 2 mm at d_{LCFS}= 2 cm to around 12 mm in the far SOL. At 6 cm from the LCFS a rapid increase of the correlation length is clearly identified and quantified.

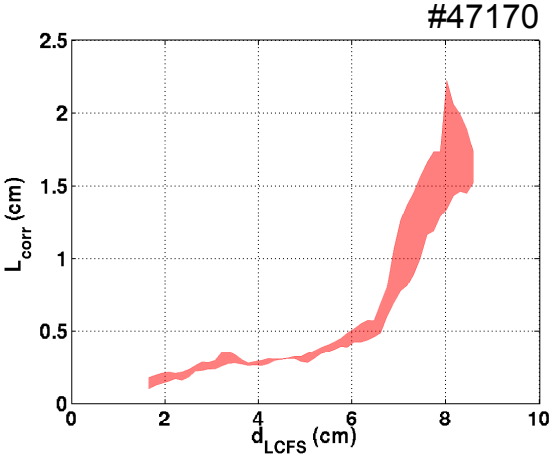

FIGURE 6.14: Amplitude correlation length in the SOL with respect to the distance to the LCFS (d_{LCFS}). The shaded area in between maximum and minimum the correlation length represents the variation of the results during the three bursts of sweeps.

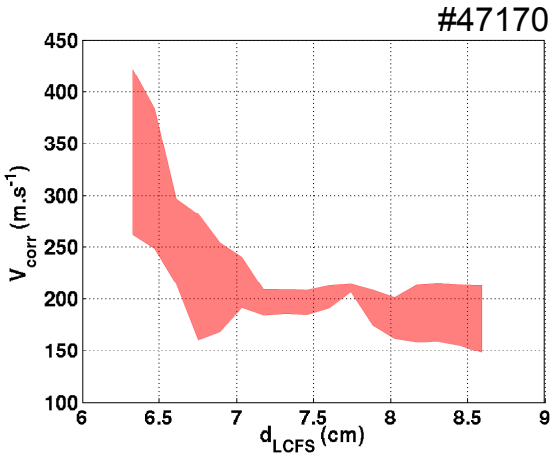

FIGURE 6.15: Radial velocity evaluated on the amplitude signal with respect to the distance to the LCFS (d_{LCFS}). The shaded area in between the maximum and minimum radial velocity represents the variation of the results.

The radial velocity has also been evaluated in the far SOL as shown in Fig. 6.15. Closer to the LCFS, the time lag for which the CCF peaks is zero, therefore the radial velocity cannot be properly inferred in this region with the cross correlation method. The radial velocity decreases rapidly from 6 to 7 cm away from the LCFS. Further outwards, the radial velocity decreases only slightly with values between 150 m s^{-1} and 220 m s^{-1}.

6.3 Summary and discussion

In this chapter, the correlation of raw signals from reflectometry has been measured on Tore Supra Ohmic discharges. The X-mode polarisation enabled to extend continuously the measurements from the plasma center up to the far SOL. It has been here evidenced that turbulence exhibits different characteristics, quantified in terms of coherence and correlation length, correlation times and propagation velocity, depending on its radial location.

Correlations have been evaluated on each component of the reflectometer signal, amplitude, phase and real part, so-called "homodyne" signal, as those account for different plasma fluctuation properties. The question of which reflectometer signal performs the more reliably the turbulence correlation length is still debated.

In all the plasma discharges we studied, the measured correlation length is observed to decrease with increasing radius, with values ranging from few centimeters in the core region down to few millimeters towards the LCFS. The three signal components present the same trend but quantitatively different values, except close to the LCFS where they do not differ much. In the surroundings of the LCFS, our measured correlation lengths

might though be artificially reduced as a consequence of high fluctuation level (see Fig. 6.9), coherently to the numerical predictions [80]. We observe nonetheless that the radial dependence and values of the correlation length from our measurements are very similar to those obtained on ASDEX Upgrade with Doppler reflectometry [87].

In the plasma center, where the fluctuation level is low ($\delta n/n < 1\%$) , the determination of the correlation length can also be challenging. Thanks to the fast sweep technique, MHD tearing modes, often particularly active in this region, are clearly identified and their radial extension is accessible. The contribution of the different frequencies to the fluctuations size was separated with the coherence analysis. The low frequencies coherence lengths were found to be two times larger than those at higher frequency. This observation indeed provides a better understanding that the correlation lengths can be dominated by these modes rather than by the microturbulence.

The correlation time was estimated at $\rho = 0.64$ in the edge plasma, around 2 to 3 μs with the fixed frequency reflectometer measurements and is too short to be effectively measured by our ultrafast sweeping reflectometer. The correlation time measures how long the signature of the turbulence on the reflectometer signals remains unchanged. If we assume that a small variation on the perturbed cut-off layer produces a small variation on the recorded signals, then the respective fluctuation timescales are similar. In the edge plasma, as the poloidal velocity is dominant with respect to the radial velocity, the correlation time should approximately scale as $t_c \approx L_c/V_\theta$, where L_c is the turbulence characteristic length. Assuming that turbulence structures have circular shapes in the $r-\theta$ plane [88], $L_c \approx L_\theta \approx L_{corr}$, and using the calculated correlation lengths ranging within 1 cm and 1 mm the poloidal velocity should range between few thousands to few hundreds m s^{-1}. This estimate is coherent with Doppler reflectometry measurements on Tore Supra [89].

Large scale propagating structures in the far SOL have been observed for the first time using ultrafast sweeping reflectometry. In the case of SOL-like turbulence [90], we have considered the amplitude signal to be the most appropriate to estimate the turbulence correlation characteristics, as coherent structures and their dynamics are there better defined. The correlation time is found to increase radially towards the far SOL, in agreement with measurements performed with Langmuir probes on Tore Supra [91].

It has been recently highlighted that the shape of turbulent structures can play a significant role when determining velocities from cross-correlation analysis [92] our calculation gives an estimate of $\sim$ 150-200 m s^{-1} for SOL structures radial velocities.

Chapter 7

Effects of macroscopic plasma parameters on the turbulence properties

In this chapter, the effects of several macroscopic plasma parameters on the turbulence properties are investigated. The first part focuses on the variation of the turbulence properties observed during a scan of the electron line averaged density and plasma current in the edge region[1]. The effect of the latter parameters on the turbulence are quantified through the correlation lengths, fluctuation levels and frequency spectra. The results are discussed in light of the main instabilities which might occur in the Tore Supra edge plasma, namely the ITG and TEM instabilities.

In the second part, the effect of the electron line averaged density on the far SOL turbulence are presented. The experimental results are compared with those obtained in numerical simulation from the 2D fluid turbulence code Tokam. A possible mechanism is proposed which may explain the observed behaviors of the turbulence correlation lengths, times and radial velocities with varying average density.

7.1 Parametric dependences of the turbulence properties in the edge plasma

A parametric study of the turbulence properties is ideally performed by comparing discharges during which only the parameter of interest is tuned. In practice, this is generally

[1]The edge region corresponds to the outer part of the confined region, i.e $0.6 \lesssim r/a \lesssim 1$.

difficult to achieve given that the plasma parameters are often interdependent. Nevertheless, the discharges analyzed here have been carefully selected in order to approach the ideal situation (i.e. only one parameter varies) as close as possible.

7.1.1 Effects of the electron density on the turbulence properties

Parameters of the discharges

9 ohmic discharges (#47169:47174 and #48100:48102) are used during which the following parameters have been kept constant $Ip = 1\ MA$, $B_0 = 3.7\ T$, $R_0 = 2.38 \pm 0.01\ m$, $a = 0.71 \pm 0.01\ m$ and $q_a = 4.5 \pm 0.1$ (q_a is the edge safety factor). Fig. 7.1 a) shows

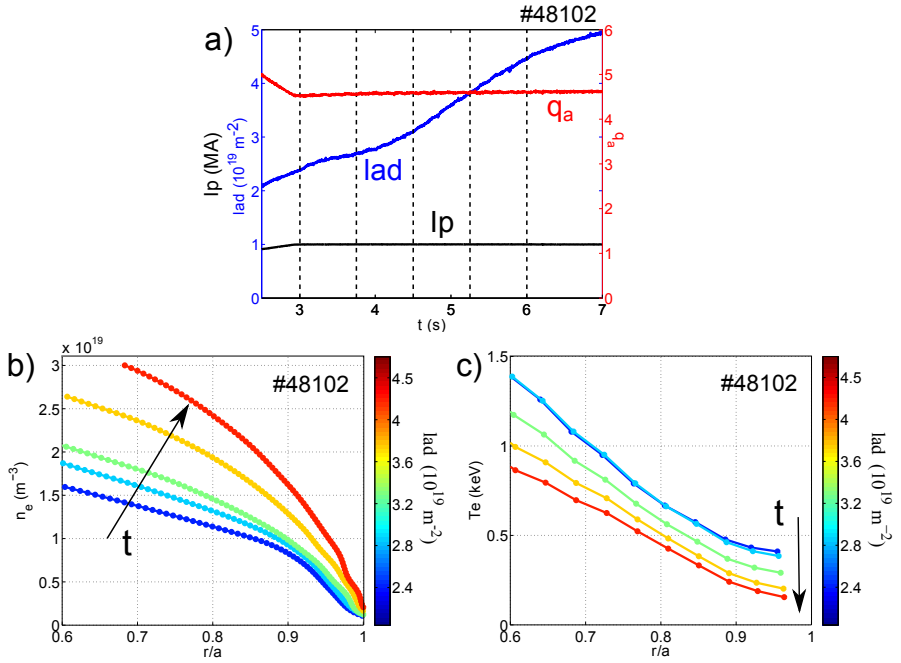

FIGURE 7.1: a) Time evolutions of the line averaged electron density (lad, blue line), plasma current (Ip, black line) and edge safety factor (q_a, red line). The vertical dashed lines denote the time of the reflectometer acquisitions. Evolution of the electron density b) and temperature profiles during the density ramp c).

the plasma scenario for the discharge #48102 which is representative of the analyzed discharges. Several reflectometer bursts (represented by the vertical black dashed lines) were performed during the density ramp. As the electron line average density (lad) is ramped up, the electron density profile measured by ultrafast sweeping reflectometry steepens (Fig. 7.1 b)). The density raise engenders a cooling of the plasma, as it is observed on the electron temperature profile measured by ECE [93] (Fig. 7.1 c)).

Radial evolution of the fluctuation level and correlation lengths

Fig. 7.2 shows the time and radial evolution of the normalized amplitude signal measured on the discharge #48102 for the lowest and highest electron density. At the first sight, the

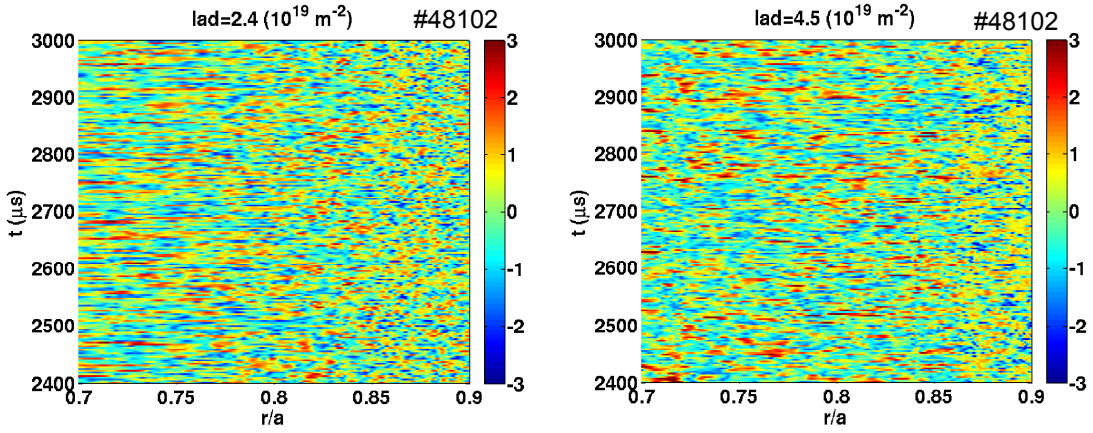

FIGURE 7.2: Time and radial evolution of the normalized amplitude signal for the lowest (left) and highest (right) line averaged electron density (lad).

signals appear very similar independently of the electron density. However, significant differences are revealed by the analysis of the radial evolution of the fluctuation levels, the correlation lengths and the frequency spectra.

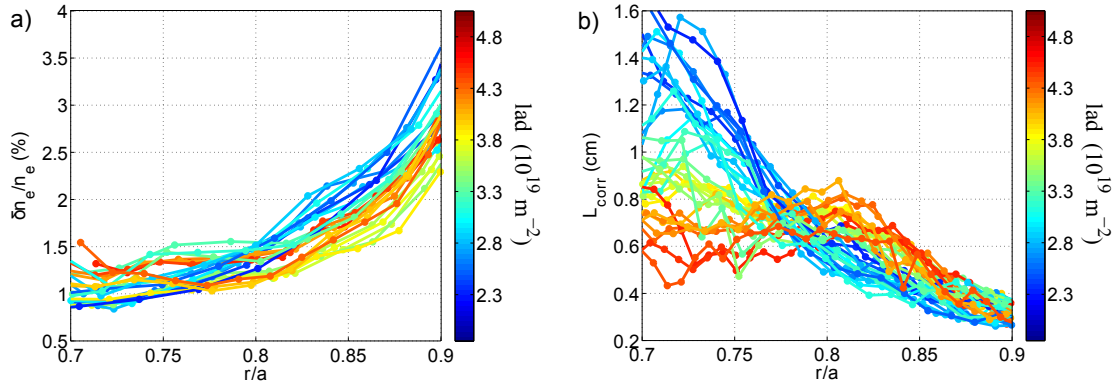

FIGURE 7.3: Radial evolution of the fluctuation levels a) and the amplitude correlation lengths b) with respect to the electron line averaged density (lad). Results obtained on 9 discharges (#47169:47174 and #48100:48102) are displayed here.

Fig. 7.3 a) shows the fluctuation level radial profiles computed as in [54] with respect to the electron density. In the region $0.7 < r/a < 0.8$, the fluctuation level increases moderately with values about $\delta n_e/n_e \approx 1 - 1.5\%$ and is not impacted significantly by the electron density raise. For $r/a > 0.8$, the fluctuation level increases more rapidly and reaches values up to $\delta n_e/n_e \approx 3.5\%$. The fluctuation level is barely larger for the low density cases than for the high density cases. Fig. 7.2 b) shows the evolution of

the correlation length radial profiles computed on the amplitude signals. The correlation lengths have a different behavior with respect to the density values. For the low density cases, the correlation lengths decreases continuously from $r/a \approx 0.7$ to $r/a \approx 0.9$. In between $r/a \approx 0.8 - 0.9$, the higher density profiles show the same radial dependency than the low density correlation lengths but with slightly larger values. In the inner edge region $r/a < 0.8$, the high density correlation lengths profiles are flatter than those obtained in the lower density cases.

Given that the fluctuation level plays a role on the error affecting the estimation of the turbulence correlation lengths, as explained in Sec. 6.3, it only makes sense to compare L_{corr} between the low and high density cases when the corresponding fluctuation levels are similar, i.e. for radial positions lying in the interval $0.7 \leq r/a \leq 0.8$.

Radial evolution of the frequency spectra

Thanks to its ultrafast sweeping capabilities, the continuous radial evolution of the frequency spectra can be traced with the reflectometer data. The frequency spectra are computed for the complex signal at constant probing frequency. The frequency spectra are estimated using the Welch's periodogram method. The complex signal is divided in 64 points time windows with 50 % overlapping. Then, a 128 points spectrum is computed on each time window. The final spectrum results from the averaging of the spectra obtained on each time window.

Fig. 7.4 shows the radial evolution of the frequency spectra obtained on discharge #48102 for increasing density. These spectra are representative of those obtained in the other discharges. The spectra have been normalized to their maximum values to facilitate the comparison among the different cases.

For different density cases and radial ranges, the frequency spectra are significantly asymmetric with respect to $F = 0$ kHz. The asymmetries are probably related to Doppler effects. However, it is not clear how the plasma motion might generate the observed asymmetries. Consequently, we only report here the observed asymmetry but no attempt is made to interpret it. Possible explanations of the Doppler shift are exposed in Appendix C.

In the inner edge ($r/a < 0.75$) at the lowest density ($lad = 2.4 \times 10^{19} m^{-2}$), the frequency spectrum is clearly dominated by frequencies in the range 50-100 kHz. This leads to a characteristic *'M-shaped'* spectrum. When the density increases, the dominant frequencies are lower. The spectra evolve gradually from the *M-shape* to spectra peaking at low frequencies and decreasing towards the high frequencies. The shape of the spectra varies

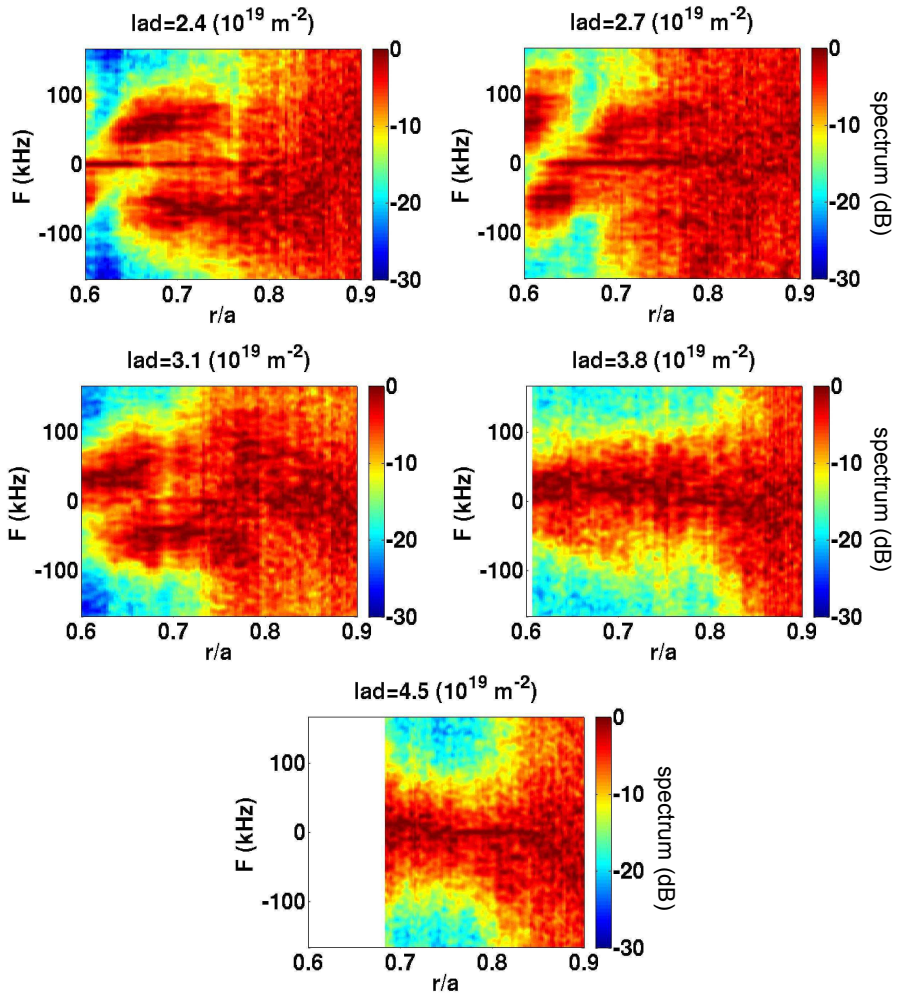

FIGURE 7.4: Radial evolution of the complex signal frequency spectra with respect to the density computed for the discharge #48102 (the density increases from left to right and top to bottom)

.

significantly for densities above lad=3.1 $\times 10^{19}\ m^{-2}$. At this specific density, the spectrum is asymmetric towards positive frequencies at $r/a \approx 0.6$ whereas the asymmetry seems to reverse around r/a=0.7.

The frequency spectra flatten for the low density cases above $r/a \approx 0.75 - 0.82$ whereas the flattening occurs at slightly larger radial positions for the higher density cases ($lad \gtrsim 3.1 \times 10^{19}\ m^{-2}$) . In the outer edge ($r/a > 0.82$) and independently of the electron density, the frequency spectra are almost flat.

At lad=3.8 $\times 10^{19}\ m^{-2}$, the spectra are shifted toward positive frequencies for $0.6 < r/a < 0.8$ whereas the lad=4.5 $\times 10^{19}\ m^{-2}$ spectra are almost symmetric around F=0 kHz.

7.1.2 Effects of the plasma current on the turbulence properties

Parameters of the discharges

6 ohmic discharges (#47670:47675) are used with the following parameters $2.5 \times 10^{19} m^{-2} <$ lad $< 2.8 \times 10^{19}\ m^{-2}$ and the same B_0, R and a as in the density scan. For each discharge, 4 reflectometer acquisitions were performed during successive Ip plateaus (Fig. 7.5 a). Contrary to the electron line averaged density which varies only slightly with the plasma current, the edge safety factor varies from $q_a \approx 4.1$ to $q_a \approx 9.5$ when the plasma current decreases from $Ip = 1.1$ MA to $Ip = 0.4$ (MA). Fig. 7.5 b) shows the evolution of the electron temperature profile with respect to the plasma current. The decrease of the plasma current causes a decrease of the ohmic heating and consequently a decrease of the electron temperature.

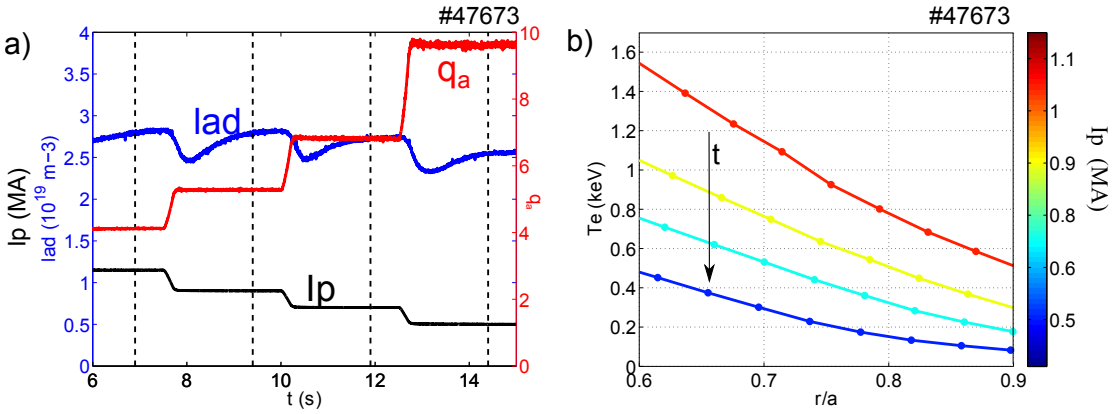

FIGURE 7.5: a) Time evolutions of the line averaged electron density (lad, blue line), plasma current (Ip, black line) and edge safety factor (q_a, red line). b) Evolution of the electron temperature profiles during the plasma current scan.

Radial evolution of the fluctuation level and correlation lengths

The effects of the plasma current on the turbulence properties are first investigated by analyzing the fluctuation level and correlation lengths and then by discussing the properties of the frequency spectra, as for the density scan.

Fig. 7.6 a) and b) show the radial evolution of the fluctuation level and correlation lengths with respect to the plasma current, respectively. The fluctuation level, computed as in [54], is almost constant in the inner plasma ($r/a < 0.75$) with values about $\delta n_e/n_e \approx 1\%$. In this region, it appears independent of the plasma current. In the outer edge ($r/a > 0.8$), the fluctuation level increases more rapidly with the minor radius. The fluctuation levels are significantly larger for low plasma current discharges than for high plasma current discharges.

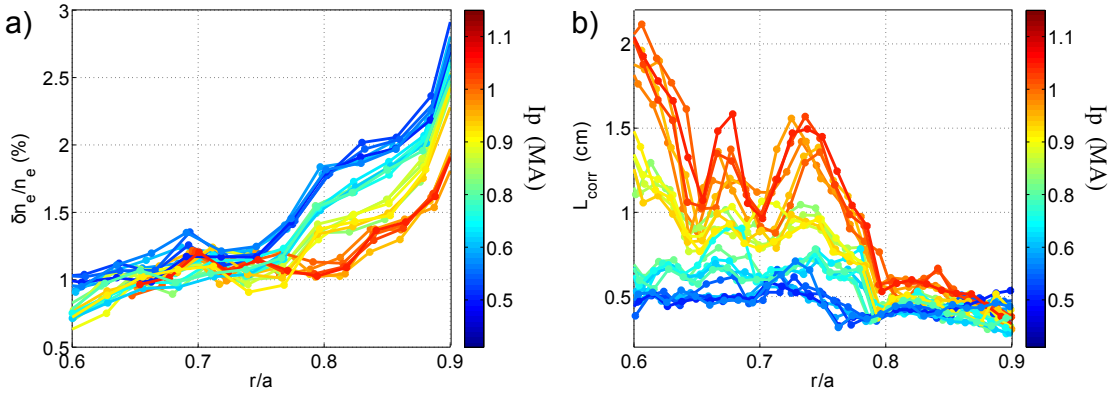

FIGURE 7.6: Radial evolution of the fluctuation levels a) and the amplitude correlation lengths b) with respect to the plasma current. Results obtained on 6 discharges (#47670 : 47675) are displayed here.

The correlation lengths show distinct behaviors depending on the radial region and the plasma current. In the outer edge ($r/a > 0.8$), correlation lengths are very similar for all plasma current with values about $L_r \approx 0.5$ cm although the corresponding fluctuation levels differ by 30%. This observation suggests that the impact of nonlinearities on the determination of the correlation length may be weaker than foreseen.
In the inner edge ($r/a < 0.8$), L_{corr} increases for smaller radii in the higher Ip discharges. The higher is the plasma current, the steeper are the correlation length profiles. In $Ip \approx 1.1$ MA discharges, two salient oscillations of the correlations lengths are observed. These oscillations are still observable in the $Ip \approx 0.9$ MA discharges but are less evident. In the lower plasma current discharges, the variation of the correlation lengths with the minor radius is less pronounced. For $Ip \approx 0.5$ MA, the correlation length is about $L_r \approx 0.5$ cm over the whole radial region.

Radial evolution of the frequency spectra

Fig. 7.7 shows the radial evolution of the frequency spectra for increasing Ip.

The characteristics of the spectra gradually change with the plasma current. At $Ip = 0.5$ MA, the spectrum is decreasing from low to high frequencies. The spectrum slightly broadens at larger radius. The spectra appear to be shifted towards the negative frequencies independently of the radial position. At $Ip = 0.7$ MA and for $r/a < 0.78$, the spectrum is narrower than that at $Ip = 0.5$. Here, the broadening of the spectrum starts around $r/a \approx 0.78$. The Doppler shift observed on the $Ip = 0.9$ MA spectrum continuously varies from negative frequencies for $r/a < 0.7$ towards positive frequencies for $0.7 < r/a < 0.8$. Above $r/a > 0.8$, the spectrum flattens. At the highest plasma current $Ip = 1.1$ MA, the spectrum exhibits specific features for $r/a < 0.8$. Around

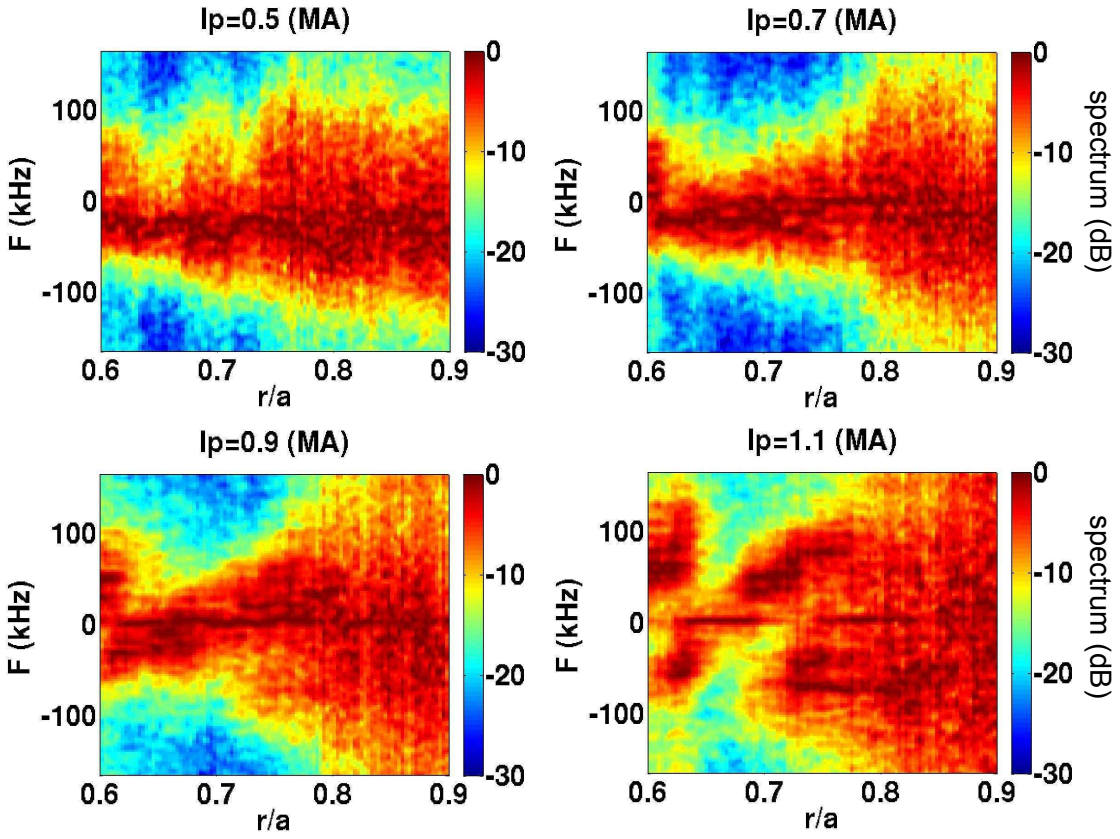

FIGURE 7.7: Radial evolution of the complex signals frequency spectra with respect to the plasma current computed for the discharge #47670 (the plasma current increases from left to right and top to bottom).

$r/a \approx 0.6$, the spectra is *M-shaped* and peaks around $F = 50 - 100$ kHz, similarly to what is observed for low density. In between $r/a > 0.63$ and $r/a < 0.68$, the higher frequencies are strongly damped. For $0.68 < r/a < 0.8$, the spectra are again *M-shaped* with dominant frequencies around $F = 50 - 100$ kHz although the asymmetry is less pronounced than that observed at $r/a \approx 0.6$. In the outer edge region ($r/a > 0.8$), the spectrum is flat.

7.1.3 Discussion

The variation of the average electron density and the plasma current strongly impacts the turbulence properties. In this section, an attempt is made to explain the abundant observations described above in the light of turbulence and transport models. First, the scaling of the correlation lengths with the drift-scale parameter ρ_s (ion sound Larmor radius) is investigated. Then, a possible interpretation of the observed frequency spectra modifications as a function of the collisionality is proposed in terms of a turbulence dominated by trapped electrons.

Scaling of the turbulence correlation lengths with ρ_s

A well known prediction of gyro-Bohm transport theory is the linear scaling of the turbulence structure size with the ion sound Larmor radius $\rho_s = \sqrt{m_i T_e}/eB$ [94]. This scaling was investigated experimentally during the last decade.

Brief review of previous results

An increase of the turbulence correlation length with ρ_s was observed in the low temperature plasma device TJ-K [95]. Nevertheless, it was found that the measured correlation length scale with $\rho_s^{1/2}$ [96], which is a weaker dependence than that predicted by gyro-Bohm theory. More recently, a systematic analysis of turbulence measurements from several plasma devices with different magnetic geometries confirmed that the correlation lengths scale sublinearly with ρ_s [97]. It is important to underline that those aforementioned studies were performed with Langmuir probes.

The possible scaling of the radial correlation length with the turbulent eddy size was studied by Rhodes *et al.* with correlation reflectometry on D-IIID Tokamak [98]. In this study, theoretical scalings of the eddy size predicted by several slab and toroidal ITG models were confronted to the measured correlation lengths. Each model leads to a linear scaling of the turbulent structure size Δr with the drift parameter ρ_s, $\Delta r = \rho_s f(R/L_n, R/L_T, R/L_S)$, but the dependence of the function f with the density (L_n), temperature (L_T) and magnetic shear (L_S) gradient scale length differs depending on the model. It was found that the measured correlation lengths are in the rough range $L_{corr} \approx 5 - 10\ \rho_s$. It was also found that all the models predict a decrease of the structures size with the plasma radius, consistently with the radial dependence of the measured correlation lengths, however only the slab ITG eddies sizes computed according to Ref. [99] were numerically close to the experimental results.

Results obtained in this work

The ρ_s scaling of the radial correlation length measured with ultrafast sweeping reflectometry on Tore Supra is investigated and presented hereafter. ρ_s is indirectly tuned through the variation of the electron temperature, i.e. ρ_s decreases (resp. increases) with the increase of the electron density (resp. the plasma current). Fig. 7.8 shows the evolution of the radial correlation lengths L_{corr} with respect to the local ρ_s value for the density (left) and current scan (right). L_{corr} varies from around 5 ρ_s at low ρ_s (which corresponds to the outer edge region $r/a \approx 0.9$) to about 10 ρ_s at large ρ_s (which corresponds to the inner edge region $r/a \approx 0.6$).

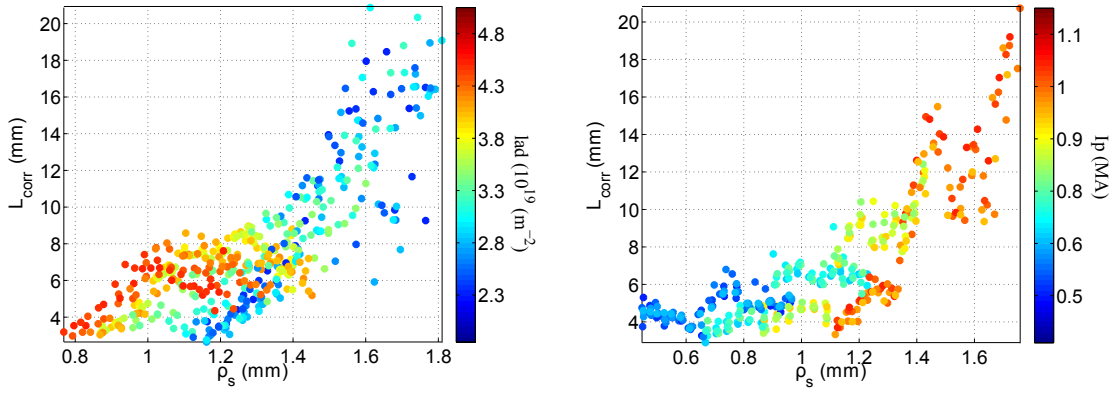

FIGURE 7.8: Evolution of the radial correlation lengths with ρ_s during the electron density (left) and plasma current (right) scan.

Attempts to fit $L_{corr} = f(\rho_s)$ with linear, power law and exponential fitting functions were made. When the whole data set is considered, the fitting functions which minimize the least-square residues are exponential with slopes around 1.5 mm^{-1} and 1.09 mm^{-1} for the density and current scan, respectively. To our knowledge, there is no theoretical model which predicts that the turbulent structures sizes scale as $\propto e^{\alpha\rho_s}$. However, the data points were widely scattered around the fitting functions. It also has to be stressed that the use of exponential fitting functions is questionable given that ρ_s and L_{corr} only vary within less than one order of magnitude. If only the low density ($lad \lesssim 3\times10^{19}m^{-2}$) and high Ip ($Ip \gtrsim 1MA$) cases are considered, the correlation lengths scale linearly with ρ_s with slopes about 22 and 20, respectively.

The ρ_s scaling of our results seems inconsistent with those obtained in previous studies with Langmuir probe measurements. Nonetheless, it is worth to mention that the measurements presented here were not obtained in a dedicated experiments during which efforts are made to keep constant the other plasma parameters. During a density or current scan, the density gradient scale length or the magnetic safety factor (and many other parameters) inevitably vary. These variations may be better accounted for using the approach follow by Rhodes where Δr depends mainly on ion related quantities such as the ion temperature or the ion temperature gradient scale length. Unfortunately, the ion temperature is scarcely measured on Tore Supra. Ion temperature measurements were only available for the discharge #48102 (density scan). Consequently, the ITG scalings *'a la Rhodes'* were tested on this discharge but unsuccessfully.
Note that the scaling of reflectometer correlation lengths with the width of an alternative type of instability, namely the resistive ballooning mode (RBM), was explored in the edge of ASDEX Upgrade [100]. This scaling was not investigated in this work given that the RBM are unstable for electron temperatures below 50 eV in Tore Supra [101]

which is significantly lower than the electron temperatures involved in this study (see Figs. 7.1 and 7.5).

Implications of the frequency spectra variation during the electron density and plasma current scan

In the following discussion, we focus on the $r/a < 0.8$ region, given that in the outer edge the frequency spectra are flat and cannot provide any useful information. The spectra asymmetries, which are still not well understood, are not considered.

A salient feature of the measured frequency spectra is the presence of bumps around F$\approx \pm$ 50-100 kHz. These bumps are only observed at low density and high plasma current. Frequency spectra with similar shapes have been observed in T-10 [102] and TEXTOR [103] tokamaks. In the latter studies, these bumps are referred to as quasi-coherent modes (QC modes). It was suggested that the QC modes could originate from ITG instabilities. Here, we explore the possibility that the QC modes are due to trapped electron modes [104] (TEM), rather than ITG instabilities. The main argument is that, contrary to ITG instabilities, TEM are stabilized at high collisionality ($\nu_{ee} \propto n_e T_e^{3/2}$). Consequently, TEM are affected by the variation of the electron density and the plasma current (through ohmic heating) and thus might be responsible for the observed evolution of the frequency spectra during the parametric scan.

In the limit of a large effective collision frequency of the trapped electron, $\nu_{eff} >> w_{*e}$, a simplified dispersion relation obtained from bounce averaged drift equation gives the TEM growth rate [105]

$$\gamma_{TEM} = \epsilon^{3/2} \frac{w_{*e}^2}{\nu_{ee}} \eta_e \tag{7.1}$$

with ϵ the inverse aspect ratio, w_{*e} the electron diamagnetic frequency, ν_{ee} the electron-electron collisionality and $\eta_e = L_{n_e}/L_{T_e}$ the ratio of the electron density and the electron temperature gradient scale lengths. The growth rate formula shows clearly that the density stabilizes the TEM through the collisionality but also through the η_e term. The density gradient scale length tends to decrease with increasing density leading to a reduction of the TEM growth rate. The TEM growth rate expression (Eq. 7.1) supports the hypothesis that the QC modes observed on the frequency spectra at low density (high plasma current) might originate from TEMs, the growth rate of which decreases at high density (low plasma current) by effect of the increased ν_{ee} and decreased density scale length, this resulting in the disappearance of the QC mode. It has to be mentioned

that a damping of the QC modes with the increase of plasma density was also reported on T-10 [106] but this observation retained low attention.

Interpretation of the results, in terms of ITG/TEM instabilities

Various approaches have been explored in order to build a coherent scenario able to explain the joint evolution of the frequency spectra, correlation lengths and fluctuation level measured by reflectometry during the parametric scans.

We first analysed the plasma linear stability for one of the density ramp discharges, #48102, by means of local simulations using the fast quasi-linear gyrokinetic code Qualikiz [107]. Qualikiz solves the local electrostatic gyrokinetic dispersion relation accounting for both passing and trapped particles, thus providing growth rates, mode frequencies and wavenumbers of all present instabilities, namely ITG, TEM or ETG. Simulations were performed at radii $r/a = 0.2 - 0.8$ using the experimental local parameters from the considered discharge, first processed by the CRONOS integrated modelling transport code [85], which further provides the ion density and temperature profiles as well as the safety factor profile needed as input to Qualikiz. Fig. 7.9 shows the normalized growth rates and frequencies computed by Qualikiz for the lowest (left) and highest (right) density cases. At low density Qualikiz predicts both ITG and TEM instabilities, the first in the inner region, with frequency around 10 kHz (not shown), and the latter dominating for $r/a > 0.75$. At high density, only the ITG is present, peaking at $r/a \approx 0.75$; the

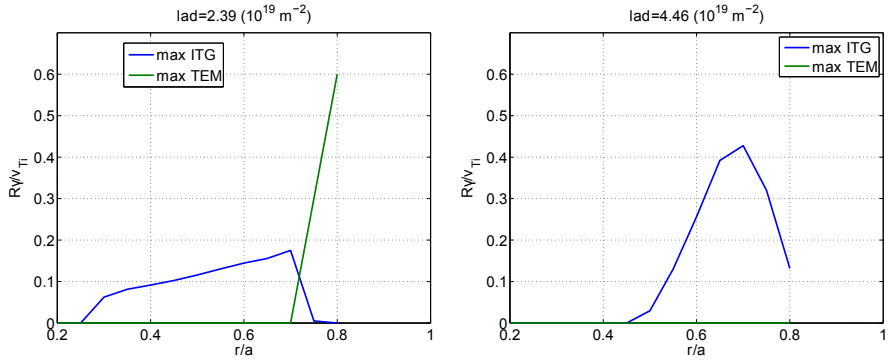

FIGURE 7.9: Radial profile of the linear growth rates of ITGs and TEMs computed by Qualikiz at low (left) and high (right) density for the reference discharge #48102.

TEM became stable.

This linear analysis shows indeed the presence of a TEM peaking at frequencies about 50 kHz at low density (Fig. 7.10, left panel), which is then stabilized at high density. However, the presence of an ITG which would become even more unstable at high density, peaking at frequency around 50 KHz (Fig. 7.10, right panel), seems contradicting the

experimental observations. At high density, on the one side the measured power spectrum presents a reduction around $F \sim 50$ kHz and on the other the correlation length decreases, whereas ITG eddies size is actually found numerically larger than TEM eddies size [108].

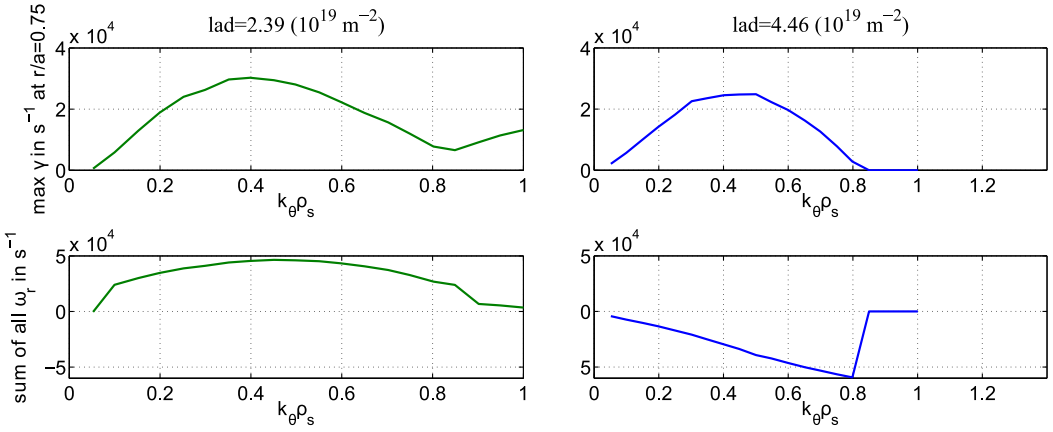

FIGURE 7.10: Growth rates and corresponding frequencies computed by Qualikiz at $r/a = 0/75$ at low (left) and high (right) density for the reference discharge #48102. Positive and negative frequencies correspond to a rotation in the electron and ion diamagnetic direction, respectively.

One should take into account that for the measured level of fluctuations (Fig. 7.3 and 7.6 a) the plasma is indeed in a non-linear turbulent regime so that the linear scenario depicted above might not be realistic. The non-linear effects have various impacts on the linear instabilities: first, the critical ion temperature gradient threshold for the ITG instability is non-linearly up-shifted to an effective critical gradient (*Dimits shift* [109]); second, the non-linear coupling induces the generation of *zonal flows*, low-frequency finite k_r, $n = m = 0$ localized flows, which on their turn have a stabilizing effect by shearing the ambient turbulence [110]; third, non-linear mode coupling induces a radial spreading of the unstable region.

Given the above considerations, one could infer that due to the Dimits shift and the damping by zonal flows, which is more effective on ITG than TEM due to their larger eddie size, ITGs could actually be non-linearly marginally stable, at least at low density. Concerning the radial localization of TEM which in the linear simulation does not match the observed QC modes localization ($r/a \geq 0.6$), turbulence spreading might be invoked. Considering now the effect of the increased density, the observed modification of the experimental spectra towards dominating lower frequencies, might be explained by a saturation of TEM, which mainly occurs via anisotropic energy transfer towards low frequency and low k zonal modes, as proposed in [111]. However, at the same time, ion-ion collisions also affect the turbulence saturation via the damping of the zonal flows [112],

which would lead again to a rise of turbulence level, which is though not observed. Considering that the transfer rate to zonal modes is significantly larger than that to other modes, one might suspect that zonal flows dominate the saturation, keeping the ITG to marginality.
The whole observed spectra behaviour could thus be understood in terms of TEM instability and saturation.
It though needs to be mentioned that the proposed mechanism is not able to account for the experimentally observed correlation length reduction with increasing collisionality.
Evidently non-linear simulations should be performed to consistently take into account the complex interplay of all the above elements, which leads to the observed stationary turbulent state.

7.2 Effects of a density scan on the turbulence properties in the far SOL

The SOL is the open field line plasma region extending up to the first walls where therefore the plasma wall interactions takes place. The issues related to plasma wall interaction, and consequently SOL physics, are of primary importance for future devices like ITER. The experimental efforts currently undertaken, as the ITER-like wall program in JET [113] or the forthcoming installation of a tungsten divertor in Tore Supra, reflect the importance of these questions.

The properties of the core plasma are also affected by SOL physics. A critical density for reactor operation, called the Greenwald density [114], above which the plasma disrupts, is though to be a consequence of SOL physics [115]. Therefore, significant efforts have been devoted to characterize the SOL properties under different density regimes. Those were primary done by focusing on macroscopic plasma quantities as the SOL density and electron temperature profiles or effective transport coefficients. The impact of the average density on SOL turbulence was studied only more recently [64, 116, 117].

In this section, the SOL turbulence properties are studied during a density scan. First the parameters of the analyzed discharges are introduced. The turbulence properties measured by reflectometry during different density plateaus are presented and followed by a discussion of the results in light of observations reported on different devices.
The possibility to interpret our measurements as the signature of individual blobs is also examined. Finally, the reflectometry measurements are compared to simulations results from a code based on a simplified SOL fluid turbulence model. From this comparison,

a possible scenario is formulated in order to interpret the modification of the turbulence properties as the density is varied.

7.2.1 Parameters of the analyzed discharges

6 Tore Supra ohmic discharges (#47680:47685) have been used to investigate the effects of the line averaged density in the far SOL. During each discharge, 4 reflectometer bursts were performed at different line averaged densities as depicted in Fig. 7.11 a). The other parameters were kept constant, namely B_0= 3.8 T, Ip=0.9 MA and q_a=5.26. The electron temperatures measured by ECE at the LCFS are about 350 eV and 10 eV, for the lowest and highest density cases, respectively.

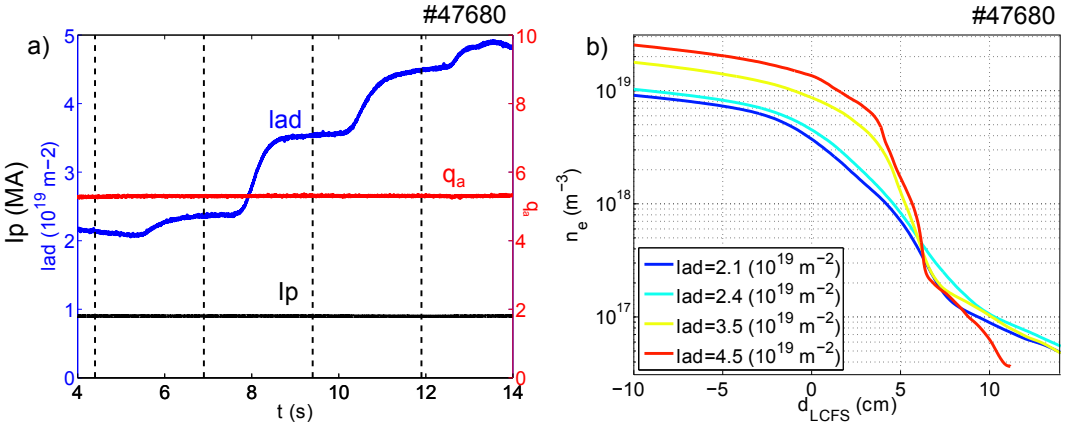

FIGURE 7.11: a) Time evolutions of the line averaged density (*lad*, blue line), plasma current (*Ip*, black line) and edge safety factor (q_a, red line). The vertical dashed lines denote the times of the reflectometer acquisitions. b) shows the evolution of the electron density profiles measured by reflectometry during the density scan.

The evolution of the electron density profiles during the density scan (Fig. 7.11 b) shows interesting features. Around $d_{LCFS} \approx 5$ cm, the density profile associated to $lad = 3.5 \times 10^{19}\ m^{-2}$ and $4.5 \times 10^{19}\ m^{-2}$ are significantly steeper than the profiles associated to $lad = 2.4 \times 10^{19}\ m^{-2}$ and $2.1 \times 10^{19}\ m^{-2}$ On the other hand, the density profiles do not differ much in the region $d_{LCFS} \geq 6$ cm if the associated line averaged density does not exceed $3.5 \times 10^{19}\ m^{-2}$. By contrast, the density profile associated to $lad = 4.5 \times 10^{19}\ m^{-2}$ decreases steeply for $d_{LCFS} \geq 6$ cm.

7.2.2 Effects on the density on the turbulence correlation properties and radial velocities

Fig. 7.12 shows a representative example of the radial and temporal evolution of the normalized amplitude signals for low (left) and high (right) density cases. Note that the

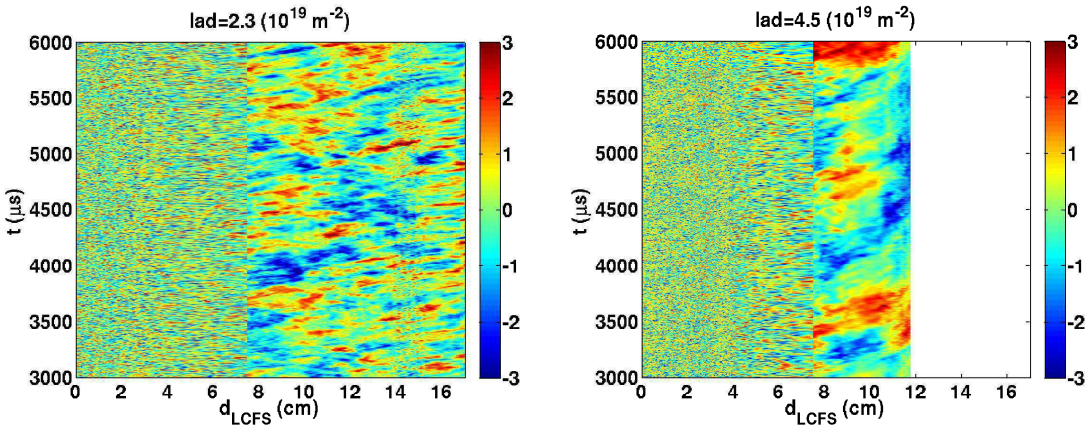

FIGURE 7.12: Radial and temporal evolution of the normalized amplitude signals for low (left) and high (right) line averaged densities measured on #47681.

plasma is detected closer to the LCFS at high density, consistently with the shape of the density profiles. At first sight, there is no obvious difference between the two different density cases for $d_{LCFS} < 6$ cm. For both cases, an abrupt transition[2] is observed around $d_{LCFS} \approx 7$ cm. In the inner SOL the amplitude fluctuations have small scales whereas in the far SOL, the fluctuations last longer and have larger sizes. In the latter region, marked differences are observed between low and high densities, namely the structures appear to have larger time and spatial scales in the high density case. Consequently a special attention is paid to the far SOL where the amplitude fluctuations properties are quantified in terms of correlation lengths, times and radial velocities.

Fig. 7.13 a), b) and c) show the radial evolution of the correlation lengths, times and radial velocities with respect to the line averaged density. The qualitative differences observed on the 2D plots (Fig. 7.12) are confirmed.

The correlation lengths tend to increase with line averaged density. At low and moderate densities, the correlation lengths are not affected by the density, and are rather constant radially ($L_{corr} \approx 1$ cm). For the highest density cases ($lad \geq 4 \times \times 10^{19}\ m^{-2}$), the correlation lengths are around 1.5-2 cm, thus substantially larger than those obtained at lower densities.

The correlation times clearly increase with the density. For low density ($lad \lesssim 3 \times 10^{19} m^{-2}$), t_{corr} is about 30-100 μs and slightly decreases with the radial position whereas for $3 \times 10^{19}\ m^{-2} \lesssim lad \lesssim 4 \times 10^{19}\ m^{-2}$, t_{corr} is around 50-200 μs and slightly increases with the radial position. At the highest density ($lad \gtrsim 4 \times 10^{19}\ m^{-2}$), t_{corr} increases rapidly with the radial position and reaches values up to 500-1000 μs.

[2]Such an abrupt transition is partially due to an imperfect matching of the V and W frequency bands (see Sec. 2.3)

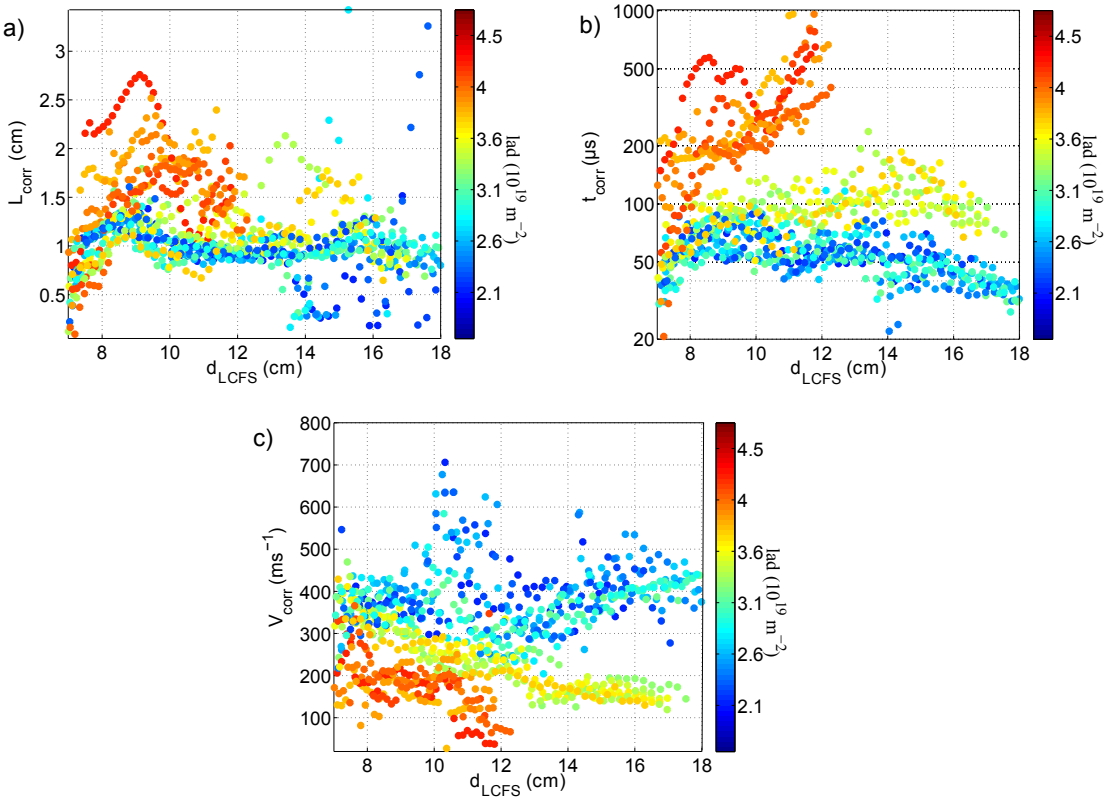

FIGURE 7.13: Effects of the line averaged density on the radial evolution of the correlation lengths (a), times (b) and radial velocities (c) in the far SOL.

The last quantity analyzed here is the radial velocity, which tends to decrease with the line averaged density. For low density cases, the radial velocities are about 300-500 m.s^{-1} and almost constant radially. For $lad \approx 3.5 \times 10^{19}$ m^{-2} , the radial velocities are about 300-400 m.s^{-1} at $d_{LCFS} \approx 7$ cm and decrease down to 100-200 m.s^{-1} around $d_{LCFS} \approx 17$ cm. At high density, the radial velocities are around 200 m.s^{-1} in the region 7 cm $\lesssim d_{LCFS} \lesssim$ 10 cm and then, decrease rapidly.

7.2.3 Discussion

The results here presented show that in Tore Supra the density profile in the SOL strongly steepens when the line averaged density increases ($lad \geq 3 \times 10^{19}\ m^{-2}$). In contrast, a flattening of the SOL electron density profiles has been reported on several tokamaks, including C-MOD [118], DIII-D [119] and TCV [64]. There, the observed flattening was, at least partially, explained in terms of an enhanced recycling occurring at high averaged density. This regime, often referred to as *main recycling regime* [120], seems to

solely apply to diverted tokamaks. The apparent inconsistency of Tore Supra measurements compared to other machines might thus be related to the limiter versus diverted configuration.

Before discussing the effects of density on the SOL turbulence properties in light of the results reported in the literature, a point should be clarified. Most of the existing works have investigated the effects of density on individual turbulent structures called *blobs*. A question arises then naturally, can we consider that reflectometer signal fluctuations are signatures of indiviudal blobs even if the beam spot size[3] is much larger than the blob characteristic scales? This question is addressed by estimating the number of blobs illuminated by the beam spot at a given time. 2 consecutive blobs are approximately separated poloidally by a distance $\Delta L_\theta \sim V_\theta \Delta t$, where Δt is the time between two blobs or waiting time. The waiting time distribution measured with probes in Tore Supra peaks around 100-250 μs [59]. Taking $V_\theta \sim V_r \sim 50 - 500\, m.s^{-1}$ leads to 5 mm $\leq \Delta L_\theta \leq$ 12.5 cm. Given that the poloidal spot size is about 20 cm, the number of illuminated blobs ranges from unity to few dozens. Consequently, the reflectometer signal fluctuations may result from a kind of poloidal average over the blob turbulence.

Existing results on the effect of density on the SOL turbulence are contrasted. In MAST [116], midplane probe measurements have revealed that the blob radial velocity first increases and then saturates when the density is increased. In contrast, the blobs durations and radial length scales were found to continuously increases with the density. In C-MOD [117], a continuous increase of the radial velocity with the density was observed with gas puff imaging. On TCV [64], an effective radial velocity deduced from transport measurements was found to increase with the density, as well as the burst durations. Note that the increase of bursts duration with the density on MAST and TCV is much weaker than the increase of the correlation time observed in Tore Supra.

It is rather challenging to conciliate the observations obtained on the different devices with those obtained on Tore Supra in order to build a general model aiming at explaining the effects of density on the turbulence properties. The effect of density seems to depend on the device geometry. The analysis technique used to infer the turbulence properties might also play an important role.

The collisionality is a key parameter in the blob analytical models [121], thus experiments on density are very convenient for testing these models. Blobs models predict that the radial velocity should scale differently with the blobs sizes depending on the collisionality. At low and high collisionalities, the dynamics of an individual blob can be described with the sheath connected [22] and inertial regimes [122], respectively. The sheath connected regime leads to $\hat{v} \propto 1/\hat{\delta}^2$, whereas the inertial regime leads to $\hat{v} \propto \sqrt{\hat{\delta}}$, where, $\hat{\delta}$ and $\hat{v}$

[3]The beam spot size is analyzed in detail in Appendix B

are normalized blobs sizes and radial velocities , respectively. The normalization factors depend mainly on the local electron temperature. Fig. 7.14 shows the relation between the radial velocities and correlation lengths measured by reflectometry during the density scan. The radial velocities are negatively correlated with the correlation lengths, namely

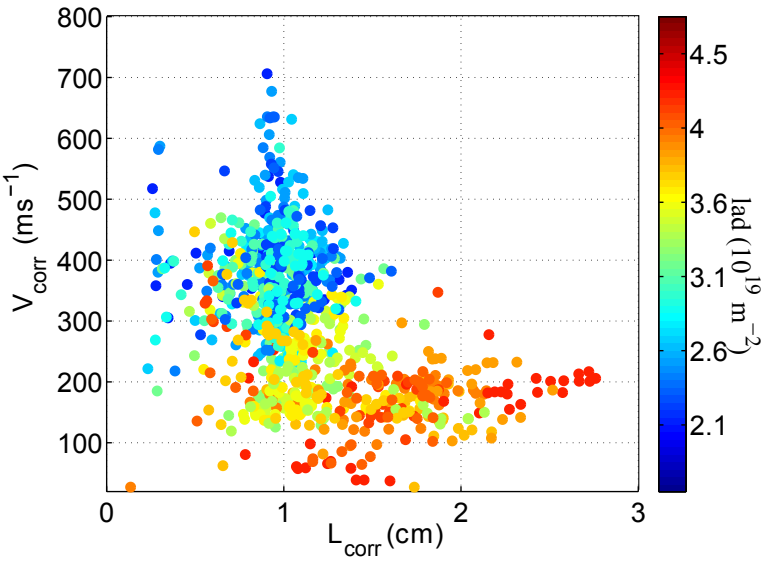

FIGURE 7.14: Relation between the radial velocities and correlations lengths for different line averaged densities.

the radial velocities decrease when the correlation lengths increase. It is tempting to conclude that the sheath connected regime is relevant in Tore Supra plasmas regardless of the density regime. However, important ingredients, such as electron temperature measurements, are missing in order to qualitatively compare our measurements to the sheath connected model predictions. Moreover, we recall that reflectometer measurements do not provide information on isolated blobs whereas blobs analytical models only apply to individual blobs. Consequently, reflectometer measurements will not be further compared to the blob models. As an alternative, the interpretation of the reflectometer measurements with the help of a SOL turbulence code is attempted in the following section.

7.2.4 Comparison with Tokam 2D SOL turbulence code

By comparing the results of the Tokam code with the measurements, this section aims at establishing the impact of collisionality on the SOL turbulence. As it will be shown below, the Tokam turbulence model is too simple to attempt a quantitative comparison with the experiments. Consequently, the Tokam parameters are not necessarily chosen such as to match the experimental parameters. Our goal is solely to check if the turbulent

properties, measured experimentally and computed numerically, follow the same trend when the collisionality is varied.

Brief description of Tokam

The Tokam fluid turbulence 2D SOL code is extensively detailed in Ref. [123, 124], only a brief description is given here.

Tokam solves the conservation equations for density and charge with cold ions and constant electron temperature. The system is reduced to 2 dimensions by performing a field line average. Fluctuations are assumed to have flute characteristics. Plasma-wall interaction is accounted for via Bohm conditions imposed at both ends of the field lines. The 2 directions correspond to radius and the poloidal angle along the poloidal gard limiters.

$$\begin{cases} \partial_t n + [\phi, n] - D\Delta n = -\sigma n e^{\Lambda-\phi} + \overbrace{S}^{source} \\ \partial_t W + \underbrace{[\phi, W]}_{E\times B advection} - \underbrace{\nu\Delta W}_{diffusion} + \underbrace{g\partial_y log(n)}_{drive\ (curvature+\nabla B)} = \underbrace{\sigma(1-e^{\Lambda-\phi})}_{sinks}. \end{cases} \tag{7.2}$$

The space and time coordinates are normalized to the Larmor radius ρ_s and the ion cyclotron frequency Ω_i, respectively. The densities and potential are normalized as follows, $n = n/n_0$, $\phi = e\phi/T_e$ where n_0 and T_e represent an arbitrary density and electron temperature, respectively. The density and the vorticity ($W = \Delta\phi$) conservation equations are non-linearly coupled through the Poisson brackets and the parallel loss terms due to the sheath boundary conditions. The Poisson brackets terms represent the $E \times B$ advection. The system becomes unstable due to the effect of g, the magnetic curvature term, which drives interchange type instabilities. D and ν are coefficients accounting for the collisional particle diffusion and viscosity, respectively. The latter coefficients are normalized to the Bohm diffusion coefficient $D_{Bohm} = \rho_s v_{th}$, with v_{th} the thermal velocity. Finally the right hand sides of the equations stand for the source and sink terms. The source term S is defined as a Gaussian. The sink terms represent the losses along the magnetic field lines. The sink terms can be seen as the boundary conditions in the parallel direction. They are obtained by using jointly the flute assumption and the Bohm sheath criterion. σ and Λ denote the conductivity and the floating potential, respectively.

Both strength and weakness of Tokam reside in the simplicity of the model. Numerous phenomena relevant to tokamak SOL physics are not modeled by Tokam, consequently it is unreasonable to attempt to compare quantitatively experimental results and Tokam

outputs. However, Tokam was found to reproduce well the statistical properties of probe signals [125]. This qualitative agreement is a strong indication that Tokam captures the dominant physics at play for SOL turbulence. In the following, Tokam is used as a *toy model* in order to interpret the SOL turbulence modifications via the density.

A possible scenario to explain the effects of density on SOL turbulence

The parameter of interest for the comparison is the collisionality. In Tokam, the increase of collisionality is accounted for by increasing the viscosity parameter ν, whereas experimentally, the increase of collisionality is achieved by increasing the density. For the sake of clarity, experimental measurements obtained at high (resp. low) density and numerical results computed for large (resp. low) viscosity will be referred to as high (resp. low) collisionality cases.

Fig. 7.16 shows snapshots of the density computed by Tokam for the low and high collisionality cases. The x and y coordinates represent the radial and poloidal directions, respectively. Biperiodic boundary conditions are used. The parameters used for the simulations leads to a gyroradius $\rho_s \approx 0.6$ mm, and thus a simulation box size of about 15.3 cm. The particle injection takes place around $x = 0$. The analysis of the turbulence properties is therefore restricted to $50 \leq x/\rho_s \leq 200$.

At first sight, obvious differences can be noticed between the low and high collisionality cases. The turbulent structures appear more radially elongated in the high collisionality case than in the low collisionality case.

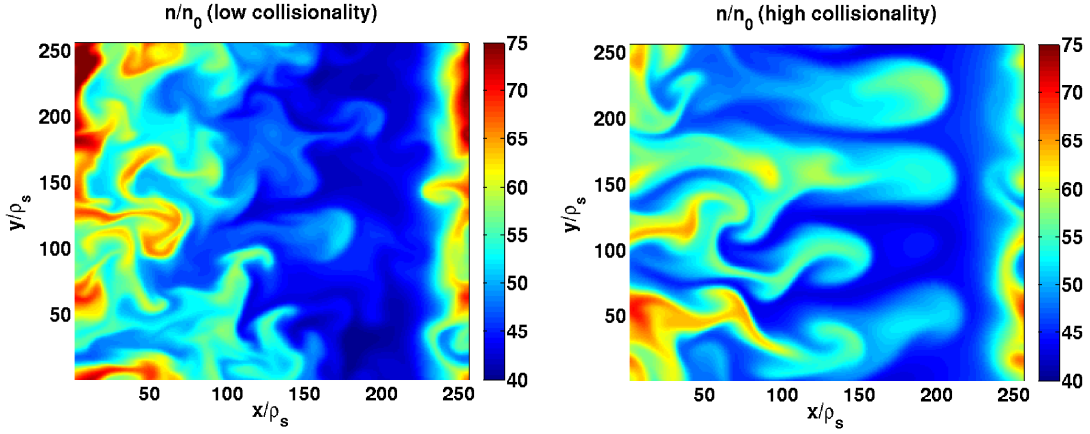

FIGURE 7.15: Snapshots of the density computed by Tokam in the stationary state of the simulation, for low (left) and high (right) collisionality cases.

The turbulence properties are quantified with the same procedure as for the experimental data. First the density is averaged poloidally in order to account for the effects of the

finite beam spot size. As a result, density time series n(x,t) are obtained for each radial position. Then, the correlation analysis applied on the time series gives the correlation times, lengths and radial velocities.

Fig. 7.16 shows the radial and temporal evolution of the poloidally averaged densities. The density have been normalized for clarity as $((n-\langle n\rangle_t)/\sigma_n)$. The similarities between the patterns observed numerically on the normalized density and experimentally in the far SOL on the normalized amplitude signals are striking (see Fig.7.12).

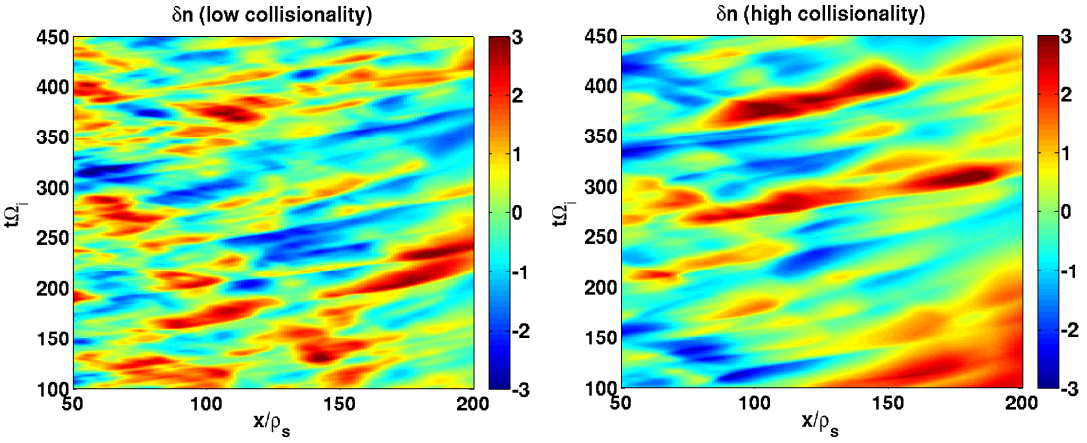

FIGURE 7.16: Radial and temporal evolution of the poloidally averaged density computed by Tokam for low (left) and high (right) collisionality cases.

The turbulence correlation properties estimated on Tokam and on reflectometer data at low and high collisionality are depicted on Fig. 7.17.

The effects of collisionality on the turbulence properties observed experimentally are qualitatively reproduced numerically, namely the increase of collisionality leads to an increase of the correlation times and lengths but also to a decrease of the radial velocity. The qualitative agreement between experiment and simulation allows us to suggest a possible mechanism to interpret the observations.

When the density (or collisionality) increases, the plasma becomes more viscous. Consequently, the interaction of the coherent structures with the background plasma is enhanced. The background plasma acts as a drag force which slows down the coherent structures. This mechanism leads to the decrease of the radial velocity observed experimentally. Moreover, the viscous term in the Tokam equation is proportionnal to the square of the laplacian of the potential $\propto \Delta^2\phi$. By expanding the potential in Fourier series $\phi(\vec{r},t) = \sum_k \phi_k e^{i(\vec{k}\vec{r}-wt)}$, one finds that the viscous damping is proportional to k^4. Consequently, the small spatial scales are damped much more rapidly than the large spatial scales. The fast damping of the small scales at high collisionality might explain why the turbulence correlation times and lengths increase with the density.

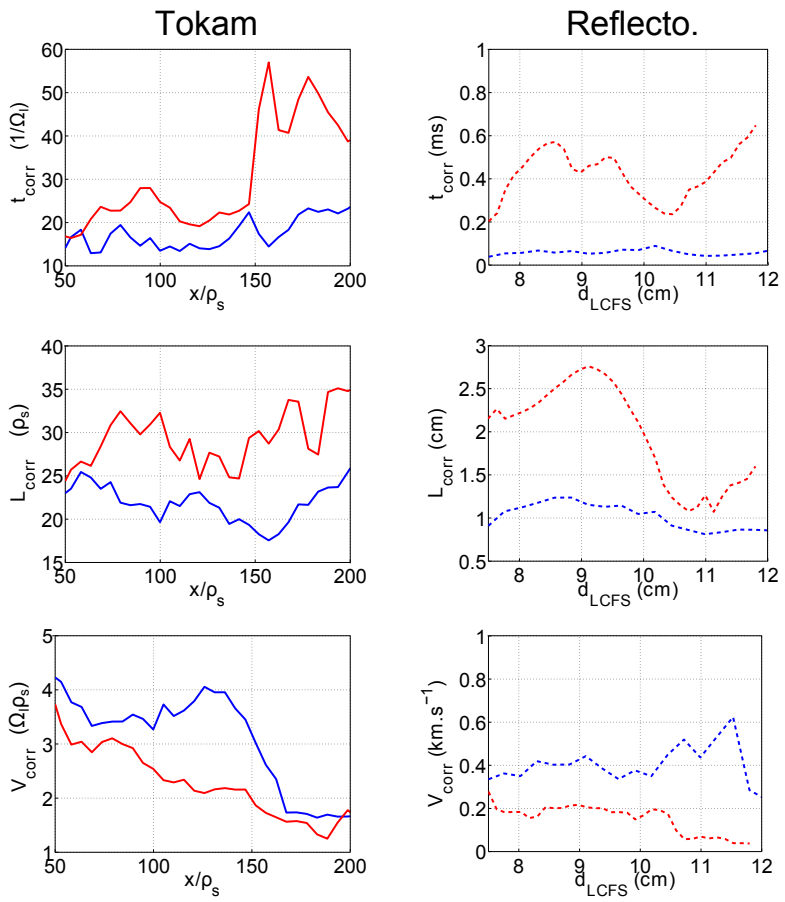

FIGURE 7.17: Effects of the collisionality on the turbulence correlation properties measured on Tokam density (left panel, solid lines) and reflectometer signals (right panel, dashed lines). The blue and red lines represents the low and high collisionality cases, respectively. The experimental data presented here were measured on the ohmic discharge #47682. The line averaged density was varied from lad=2.3 $\times 10^{19}\, m^{-2}$ (low collisionality) to lad=4.5 $\times 10^{19}\, m^{-2}$ (high collisionality).

7.3 Summary

In this chapter, the effects of different plasma parameters on the turbulence properties measured by reflectometry have been investigated. In the closed field line region, the turbulence properties have been characterized with the frequency spectra, correlation lengths and fluctuation levels whereas in the SOL plasma, the correlation lengths and times and the radial velocities have been used.

The evolution of the reflectometer signals during the electron density and current scan was attributed to the variation of the plasma collisionality. An increase of the collisionality, indifferently achieved through the increase of density or the decrease of plasma current, produces similar effects on the spectra and correlation lengths. The correlation length was observed to decrease while increasing the collisionality in the plasma edge. In the region $0.6 \leq r/a \leq 0.75$, the spectra was dominated by quasi-coherent (QC) modes

with frequencies around 50-100 kHz in the low collisional plasma. The QC modes are no more visible on the spectra at high collisionality. In this case, the spectra are dominated by low frequencies and decrease towards the high frequencies. We strongly suspect that the QC modes are a signature of TEM modes, a type of instability which may be damped by collisionality.
Attempts have been made to interpret the local variation of the turbulence properties. A coherent scenario was proposed in terms of TEM instability which can account for the observed frequency spectra modifications. It was though difficult to explain the joint evolution of the spectra, correlation lengths and fluctuations levels. Fully nonlinear simulations would be needed to shed some light on the mechanisms leading to the observed turbulence modifications.

In the second part of the chapter, the effects of plasma density on the turbulence properties were investigated in the far SOL. A significant reduction of the radial velocity was observed while increasing the density. On the other hand, the correlation times and lengths were found to increase with the density. We think that the key parameter which causes these variations is again the collisionality.
As it is now widely accepted that the far SOL turbulence is dominated by blobs, the possibility to compare our measurements to blob analytical models was considered. However, such a comparison is difficult due to a main incompatibility between the experimental and the theoretical approaches. Namely, the latter always considers a single blob whereas the reflectometer signal accounts for all blobs in the illuminated area. As an alternative, the SOL turbulence code Tokam was used and provided a satisfactory interpretation of the experimental measurements. By increasing the collisionality, the SOL plasma becomes more viscous. In Tokam simulations, it was found that the viscosity enhances the interaction between the propagating structures and the background plasma. This leads to the observed reduction of the radial velocities. Moreover, the small scales structures are faster damped at high collisionality explaining the increase of the correlation lengths and times.

Chapter 8

Effects of ICRH heating on the turbulence properties in the far SOL

On Tore Supra, the heating is mainly achieved by radio waves in the range of the ion cyclotron frequencies (ICRH heating). An increase of the ion temperature in the core plasma, and thus a steepening of the ion temperature profile, results from the injection of ICRH power. As the ion temperature gradient is a major drive of the turbulence, the application of ICRH heating possibly modifies the turbulent state of the core plasma.

In the selected database used in this work, ICRH power was limited to 2 MW due to technical problems during the last experimental campaign. No significant modifications of the turbulence properties in the core plasma were observed during ICRH heating. This might be due to the insufficient ICRH power.

On the other hand, number of works have shown interest in the modification of the SOL properties in ICRH heated plasma. Antenna erosion [126], hot spots [127, 128], enhanced sputtering [129, 130] and disruptions [131] are among the undesirable effects caused by ICRH heating. More recently, strong modifications of the turbulence properties, including a decrease of the fluctuation level and a flattening of the frequency spectra, have been measured by Langmuir probes on ASDEX-Upgrade [132] and Tore Supra [133]. In this chapter, the modifications of the turbulence properties as observed by ultrafast sweeping reflectometry are presented. First the parameters of the ICRH discharges are described. Then, the turbulence properties during ICRH heating are analysed and compared to those obtained in ohmic discharges. Finally, mechanisms potentially able to account for the reflectometer measurements are discussed.

8.1 Parameters of the ICRH discharges

The data used here were acquired during 7 discharges (# 46996:47002) where different ICRH antennas were successively switched on. The heating scheme is summarized in Fig. 8.1 a). Reflectometry acquisitions were performed during the initial ohmic phase, in the ICRH phases and in between two successive ICRH phases which are separated by around 30 ms. The injected power varies from about 0.5 MW to around 2 MW depending on the discharge and the active antenna. Nonetheless, the modifications of the turbulence properties were found to be independent of the injected power.

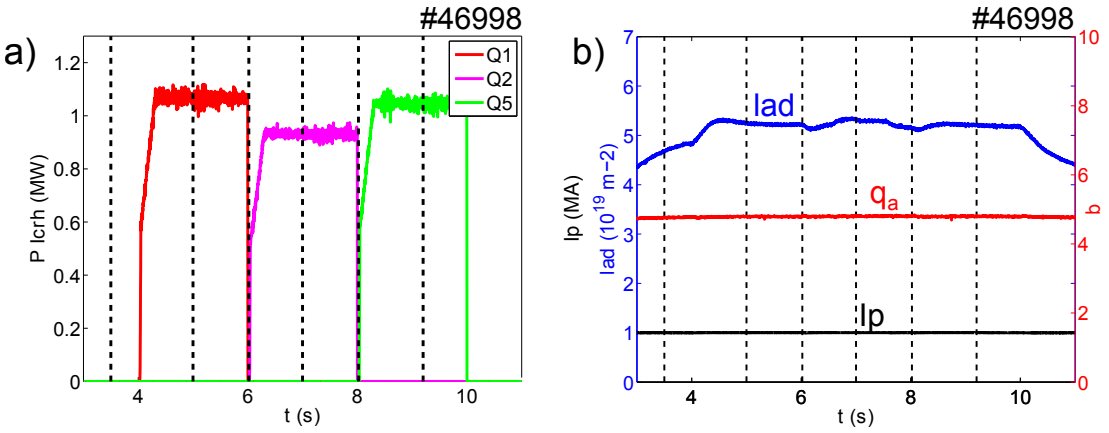

FIGURE 8.1: a) Heating scenario: the ICRH power was injected with 3 distinct antennas (Q1, Q2 and Q5) after an initial ohmic phase. b) Time evolutions of the line averaged density (lad, blue line), plasma current (Ip, black line) and edge safety factor (q_a, red line). The vertical dashed lines denote the time of the reflectometer acquisition.

Fig. 8.1 b) shows that the plasma parameters are almost constant over a discharge. The plasma parameters vary moderately among the analyzed discharges, with values Ip=0.9-1MA, q_a=4.8-5.4, B=3.84 T and lad=4-5.4 $\times 10^{19}\, m^{-2}$. Note that the density is generally lower during the ohmic phase. The electron temperature measured by ECE at r/a=0.8 varies from about 0.3 KeV to around 0.5 Kev during the ohmic and ICRH phases, respectively.

As it will be shown below, the turbulence properties strongly depend on the active ICRH antenna, it is thus worth to remind the locations of the ICRH antennas with respect to the reflectometer port. Fig. 8.2 shows an illustration of the torus wall unwrapped along the toroidal direction. It is important to notice that the reflectometer is located in the same port that the antenna protection (LPA). As the LPA is radially closer to the LCFS than the ICRH antennas, the LPA acts as a solid boundary. The $\varphi = 0$ reference position is therefore taken as the LPA toroidal position. While moving along the toroidal direction, Q5 is the closest antenna with respect to the reflectometer, followed by Q1 and

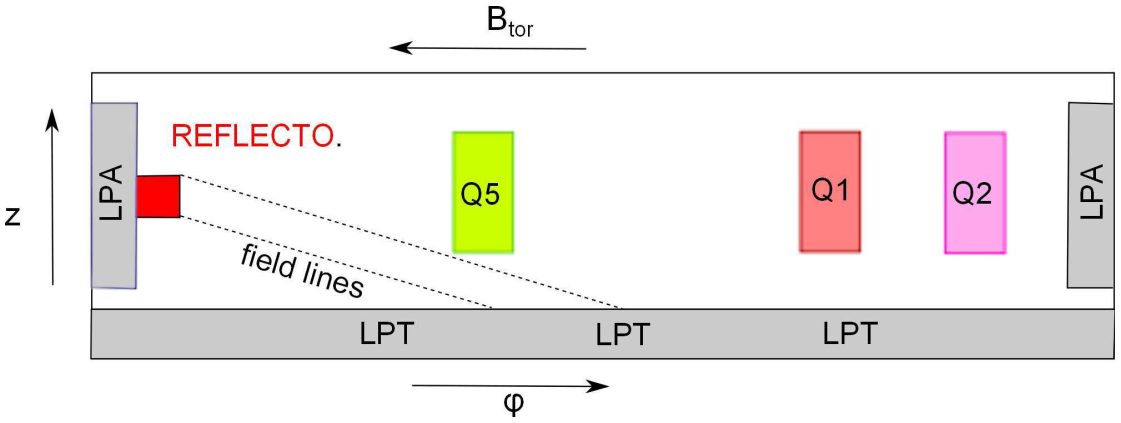

FIGURE 8.2: Schematics of the ICRH antennas toroidal locations in Tore Supra, with respect to the reflectometer. Q5, Q1 and Q2 label the ICRH antennas. LPA and LPT refer to the antenna limiter and toroidal limiter, respectively. The magnetic connections of the reflectometer are also shown.

finally Q2. The reflectometer is generally magnetically connected to the toroidal limiter (LPT). The fieldlines intersect the LPT below the ICRH antenna Q5.

8.2 Modifications of the turbulence properties during ICRH heating

The comparison of the amplitude signals recorded during ohmic and ICRH phases reveals strong differences. These differences are more or less pronounced depending on the active antenna as shown in Fig. 8.3. As soon as ICRH is on, the plasma tends to expand radially outwards in the far SOL. During the ohmic phase, the plasma is first detected about 10 cm outside the LCFS. When Q1 or Q2 are powered, the plasma is detected around 16 cm outside the LCFS. When Q5 is switched on, the plasma expands as far as 22 cm beyond the LCFS. Clearly, the modifications of the reflectometer signals induced by ICRH are much stronger when Q5 fires rather than when Q1 or Q2 are powered. These modifications are better quantified when comparing the usual correlation properties of the reflectometer signal.

Fig. 8.4 a), b) and c) show the profiles of the correlation times, lengths and radial velocities, respectively. Here data obtained during the 7 discharges are shown. The expansion of the plasma during the ICRH phase, which is especially marked when Q5 is active, is confirmed.

In ohmically heated plasma, the correlation times increase sharply from around 60 μs at d_{LCFS}=6 cm up to 1 ms at d_{LCFS}=10 cm. When Q1 or Q2 are active, the correlation time profiles are very similar. In those cases, t_{corr} increases radially in between d_{LCFS} =

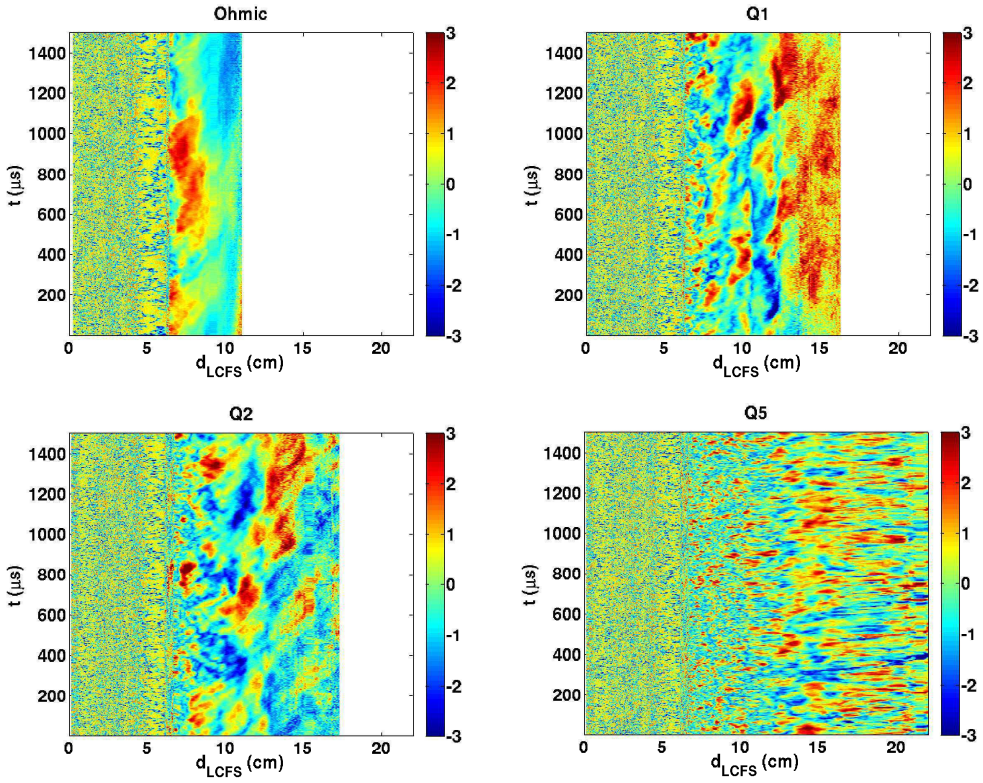

FIGURE 8.3: Time and Radial evolution of the normalized amplitude signals with respect to the active ICRH antenna. The ohmic data were acquired before the first ICRH phase. These signals were recorded on the discharge #46998.

$5cm$ and d_{LCFS} = 10 cm and then saturates with values around 60-110 μs. The profile of t_{corr} in Q5-heated plasma exhibits salient differences: t_{corr} increases from 8-20 μs at d_{LCFS}=6 cm to 60-70 μs at d_{LCFS}=25 cm. An oscillation is clearly visible on nearly all the discharges presented here. The crest of the oscillation is located at d_{LCFS} ≈14 cm.

The correlation lengths is the quantity for which the differences between each case are the less pronounced. During the ohmic phase, most of the correlation lengths lie in the range 1.5-2.5 cm. Again, L_{corr} does not differ much between Q1 and Q2 plasma with values around 1.5-2.5 for 7 cm $\leq d_{LCFS} \leq$ 13 cm. Nevertheless, a significant dispersion of the correlation lengths is observed for $d_{LCFS} >$ 13 cm. There, L_{corr} varies between 2 mm to 4 cm. When Q5 fires, the correlation lengths increase smoothly from d_{LCFS} = 5 cm to d_{LCFS} = 12 cm with values ranging from 2 mm to 1 cm, then L_{corr} saturates before decreasing in the very far SOL.

The last quantity of interest is the radial velocity V_{corr}. During the ohmic phase, V_{corr} values are around few hundreds $m.s^{-1}$ and decrease suddenly to few tens $m.s^{-1}$ when approaching $d_{LCFS} \approx$ 13 cm. When Q1 or Q2 fire, the estimated velocities are rather radially constant with values just above those found during the ohmic phases. Q5 firings lead to major differences on the radial velocities. First, note that the correlation method

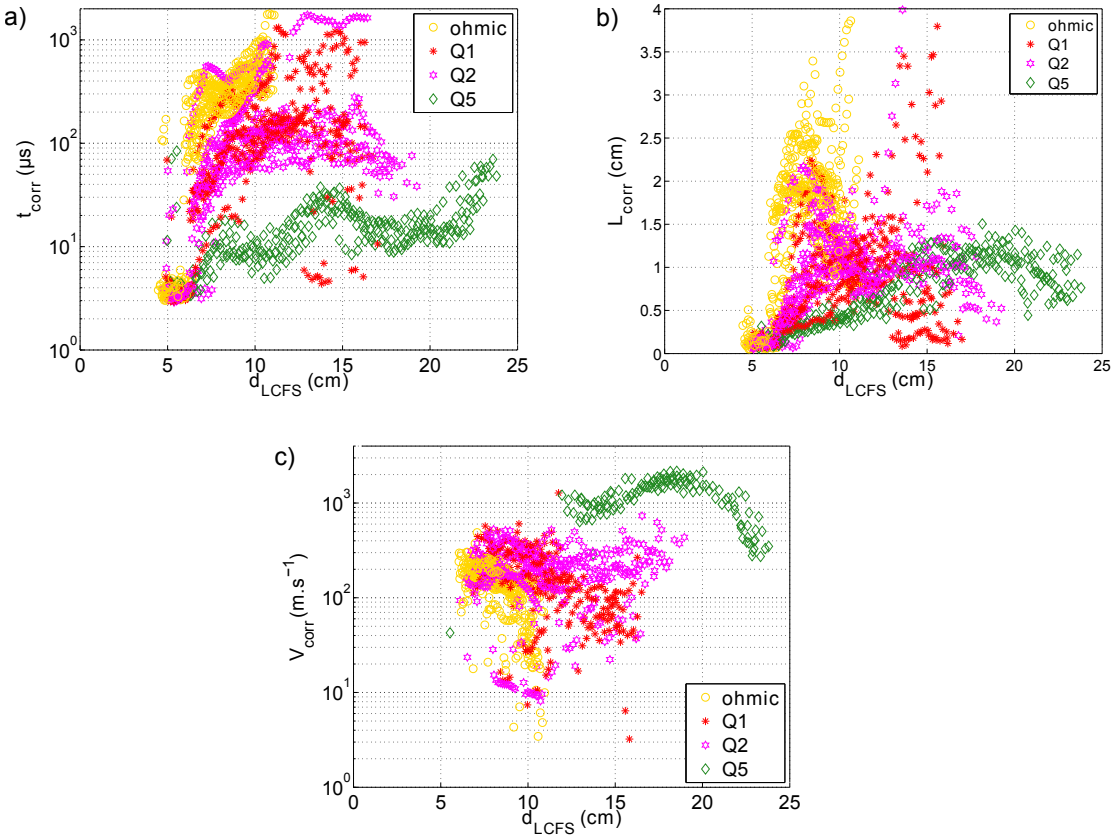

FIGURE 8.4: Far SOL profiles of the correlation times a), lengths b) and radial velocities c) during ohmic and ICRH heating.

can not provide radial velocities estimates in the region $d_{LCFS} \leq 12$ cm when Q5 is on. The underlying reasons are not very clear. A possible explanation might be that the poloidal velocities are locally much larger than the radial velocities, in this case, the radial displacement of the turbulent structures while crossing the beam spot is to small too be detected by the reflectometer. For $d_{LCFS} > 12$ cm, a specific and reproducible trend is observed on the radial velocitiy profiles. V_{corr} increases from 1 km.s^{-1} at $d_{LCFS} \approx 12$ cm, peaks at $d_{LCFS} \approx 17$ cm with values around 2 km.s^{-1}, and then decrease down to 300 m.s^{-1} in the furthest part of the SOL.

8.2.1 Considerations on the role of the active antenna

The role played by the active antenna during ICRH heating was previously investigated by Antar *et al.* [133]. Turbulence modifications were observed with Langmuir probes which are spatially close to the powered antenna but not necessary magnetically connected it. When the probes are located far from the active antenna, almost no modifications were recorded on the probes signals. As shown in the last section, the effects of ICRH on turbulence properties measured by reflectometry are the most pronounced

when Q5 fires. Given that Q5 is the antenna which is the closest to the reflectometer, our observations are consistent with the probe measurements.

The condition of toroidal vicinity is rather important because it restricts the number of phenomena potentially responsible for the turbulence modification. It is rather unlikely that the mechanism which causes the turbulence modification takes place in the closed field lines region. In this case, the turbulence would be affected globally due to the very fast parallel transport. What is needed to be invoked is an ICRH-induced phenomenon specific to the SOL region. This phenomenon shall also account for the combined modifications of the turbulence correlation properties, namely an increase of the radial velocities and a decrease of the correlation times.

8.2.2 Impact of the Faraday screen design

As it will be shown below, the modification of the turbulent properties depends on the design of the metallic screens equipping the ICRH antennas and aiming at filtering the parasitic waves modes, called Faraday screens. Consequently, the study of the turbulence with different screen configurations is worth because it may bring new information on the mechanism which causes the turbulent modifications.

The results presented so far were obtained with the *new* Faraday screen [134] installed

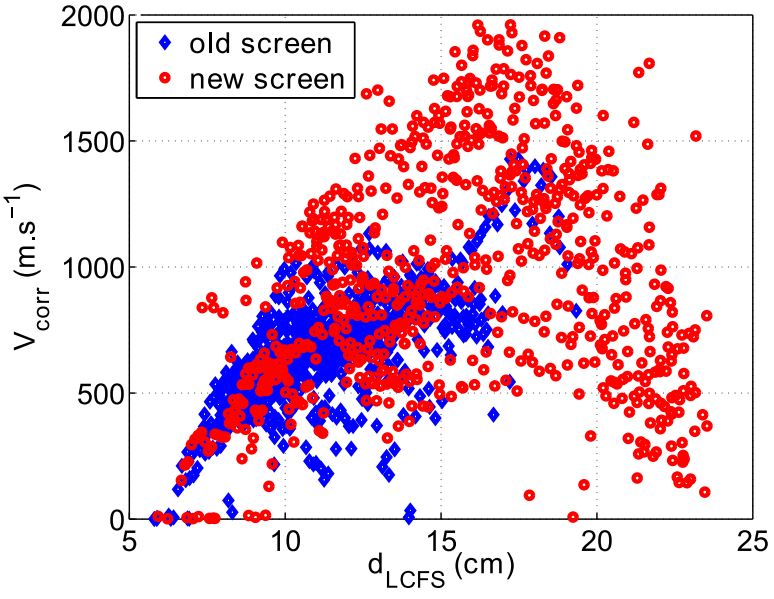

FIGURE 8.5: Comparison of the radial velocity profiles measured in Q5 heated plasma for the old (discharges #46590 : 46599) and new (discharges #47151 : 47155 – 47159 : 47162) Faraday screen.

on the Q5 antenna since 2011. In Fig. 8.5, the radial velocities profiles measured with

the old and new screen are compared[1]. The radial velocities measured with the old Q5 configuration are well above those obtained when Q1 or Q2 are powered (Fig. 8.4). This finding confirms that the mechanism, which impacts the turbulent structures, takes place in the vicinity of the active antenna. Moreover, the radial velocities obtained with the old and new Q5 configurations are very similar. The new screen appears to simply enforce the observed modifications.
It has to be stressed that the new screen was primarly designed to mitigate an ICRH-induced phenomena called radio frequency (RF) rectified potential. Surprisingly, probe measurements reported that instead of being reduced, the potentials are enhanced by the new screen [135]. These potentials are therefore excellent candidates to account for the Q5 induced modification and are thoroughly discussed in the following section.

8.3 Effects of the radio frequency rectified potentials on the turbulence properties

Sheath rectified potentials localized on the antenna side limiters are well-known consequences of ICRH heating [136]. These phenomena have been thoroughly studied both experimentally and theoretically. The rectified potentials can be basically explained as follows. The parallel component of the heating wave electric field produces a fast oscillating radio frequency potential at the boundaries between the plasma wall and the magnetic field lines. As a reaction, the field lines get biased at a DC potential which is generally much larger than the usual Bohm sheath potential. The detailed description of the interaction of ICRH waves and plasma boundaries is outside the scope of the present work but a comprehensive review can be found in [137].

On Tore Supra, rectified potentials have been measured on the Q5 antenna by means of Langmuir probes. A 2D mapping of the potential structures [138] is shown in Fig. 8.6. Rectified potentials exhibit strong up-down asymmetries. The potentials are much larger at the bottom of the antenna. More attention will be paid to the bottom potential given that the projection of the reflectometer location along the field line is close to the bottom of the antenna (see Fig. 8.2). The bottom potential reaches values up to 180 V and peaks poloidally around 25 cm below the midplane and radially around 5 cm outside the LCFS. Note that the potential is elongated along the poloidal direction leading to an electric field in the radial direction.

These potentials give rise to an electric field and consequently to an $E \times B$ convection. The $E \times B$ convection will interact with the turbulence and modify the turbulence

[1]The discharges presented here were not necessarily performed with similar plasma parameters which may explain the large dispersion of the data points.

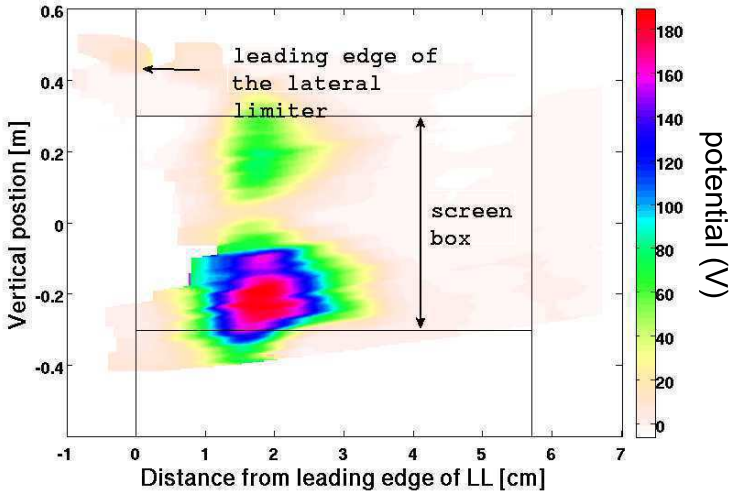

FIGURE 8.6: Rectified potentials measured by Langmuir probes on the lateral limiter (LL) of the Q5 antenna. The leading edge is located 3 cm outside the LCFS. The figure is adapted from [138].

properties. In the following, the effect of rectified potentials on the turbulence properties is investigated by means of Tokam simulations. Specific questions are addressed in detail: what is the impact of the potential on the turbulence correlation properties? Does the potential lead to an expansion of the plasma as observed experimentally?

8.3.1 Modeling of the rectified potentials with the Tokam code

Before describing the implementation of the potential in the code, preliminary remarks have to be formulated. As explained in Sec 7.2.4, Tokam is considered here as a *toy model*. There is no attempt to compare quantitatively the experimental results with the outputs of the code. The effects of the potential on the turbulence will be studied only qualitatively. Consequently, the values of Tokam parameters are not chosen to perfectly match the experimental values.

The rectified potential is numerically reproduced by biasing the sheath boundary electric potential within a limited domain in the (x,y) plane [139]. The floating potential Λ in Eq. 7.2 is then modified in a limited 2D region. The size of the biased domain is chosen such to be much larger than the turbulent structure sizes in order to qualitatively reproduce the features of the rectified potential. Fig. 8.7 a) shows a snapshot of the Tokam potential with an external biasing. Here, the plasma was simulated for approximately 3 ms with ρ_s about 0.6 mm. The biased domain is centered at $(x_0, y_0) = (200, 256)$. To ensure the continuity between the biased and unbiased domains, the floating potential is modeled

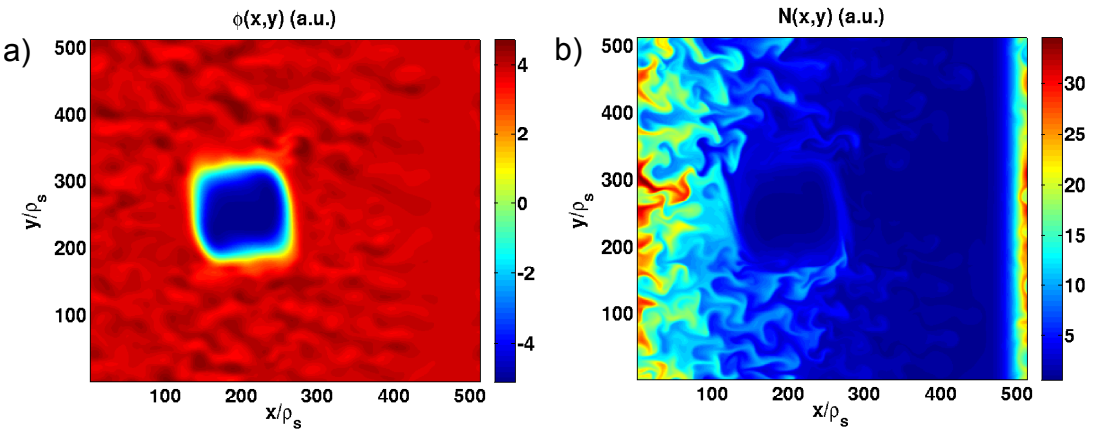

FIGURE 8.7: Snapshots of the biased potential a) and the corresponding density in Tokam b).

as a hyperbolic tangent function,

$$\Lambda(x,y) = \begin{cases} \Lambda_0 + \Lambda_p(1+\tanh(\frac{x-x_l}{L_x}, \frac{y-y_d}{L_y})) & \text{if} \quad x \leq x_0,\ y \leq y_0 \\ \Lambda_0 + \Lambda_p(1+\tanh(\frac{x_r-x}{L_x}, \frac{y-y_d}{L_y})) & \text{if} \quad x > x_0,\ y \leq y_0 \\ \Lambda_0 + \Lambda_p(1+\tanh(\frac{x-x_l}{L_x}, \frac{y_u-y}{L_y})) & \text{if} \quad x \leq x_0,\ y > y_0 \\ \Lambda_0 + \Lambda_p(1+\tanh(\frac{x_r-x}{L_x}, \frac{y_u-y}{L_y})) & \text{if} \quad x > x_0, y > y_0. \end{cases} \tag{8.1}$$

The sizes of the biased domain in the x and y directions are $x_r - x_l = y_u - y_d = 128\rho_s$ ($\sim 7.7\,cm$). $L_x = 2\,\rho_s$ and $L_y = 20\,\rho_s$ are the characteristic gradient scale lengths chosen in order to obtain a stronger gradient along the x direction. $\Lambda_0 = 4$ is the usual Bohm sheath potential. Note that $\Lambda_p = -9$ is chosen negative in order to guarantee the numerical stability of the code[2]. For T_e=100 eV, Λ_p is equal to 900 V in S.I. units.

Fig. 8.7 b) shows a snapshot of the density computed by Tokam. On the biased domain, a density depletion can be observed as well as the absence of turbulent structures. The effect of the polarization on the time averaged density profiles can be studied by comparing the density with and without external biaising. This is done on Fig. 8.8 where $\Delta N(x,y) = [\langle N(x,y)^{bias}\rangle_t - \langle N(x,y)^{no\,bias}\rangle_t]/\langle N(x)^{nobias}\rangle_{t,y}$ is depicted, $\langle N(x,y)^{no\,bias}\rangle_t$ and $\langle N(x,y)^{bias}\rangle_t$ being the local time averaged density with and without biasing, respectively. $\langle N(x)^{nobias}\rangle_{t,y}$ is the unbiased density averaged both in time and along the y direction. Note that the normalization and the colorbar have been chosen such to reveal the density variations related to the effects of the polarization. In fact, the time averaged density can vary poloidally up to 30%.

[2] $\Lambda_p > 0$ might cause the code to diverge because of the exponential form of the sheath boundary condition (Eq. 7.2)

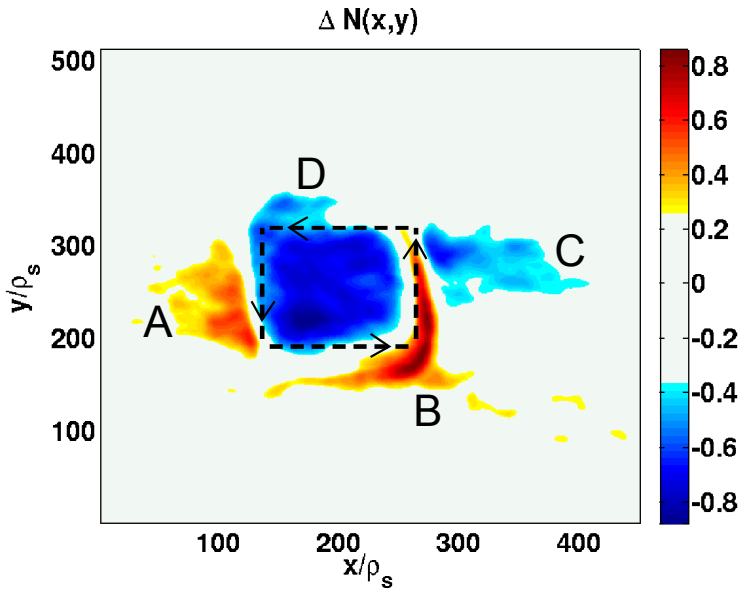

FIGURE 8.8: Effects of the external biasing on the time averaged density. The depicted quantity is $\Delta N(x,y) = [\langle N(x,y)^{bias}\rangle_t - \langle N(x,y)^{no\,bias}\rangle_t]/\langle N(x)^{nobiais}\rangle_{t,y}$, where $N(x,y)^{no\,bias}$ and $N(x,y)^{bias}$ are the local time averaged density with and without biasing, respectively. $\langle N(x)^{nobias}\rangle_{t,y}$ is the unbiased density averaged both in time and along the y direction. The boundaries of the polarized domain are indicated with dotted lines. The direction of the E×B convection is indicated by arrows.

The figure shows interesting and informative patterns. First, a net accumulation of density is observed in front of the polarized domain (region A). This accumulation results from the strong potential gradient which takes place at the boundary of the polarized domain. The potential acts as a local transport barrier [140] which stops the turbulent structures and consequently causes the density depletion observed inside the polarized domain. The counter clockwise $E \times B$ advection explains why the region B is denser than the unbiased case whereas the region D is less dense than the unbiased case. A vast area ,labeled C, is depleted in density.

The effect of macroscopic potentials on the plasma density was also studied using an advection-diffusion model in [141]. In this approach, the advection term accounts for the E×B convection caused by the potential whereas turbulent transport is modeled via a diffusive coefficient. Consistently to the finding presented here, the advection-diffusion model leads to a density depletion inside the polarized domain. It was also found that, for large enough potential $V_0 \geq 50V$, the density significantly increases behind the polarized domain , which is not observed on Tokam simulations.

Only the effect of polarization on the time averaged density has been studied so far. We analyze now the turbulence properties in presence of external baising. Fig. 8.9 a), b) and c) show the spatial dependence of the correlation times, lengths and the radial velocities, respectively. Two general comments can be formulated. The potential affects

the turbulence correlation properties only locally. Far from the polarized domain, the correlation properties have similar values to those obtained without external biasing. As the turbulent activity is strongly damped inside the polarized domain, the density does not fluctuate making the correlation analysis not meaningful.

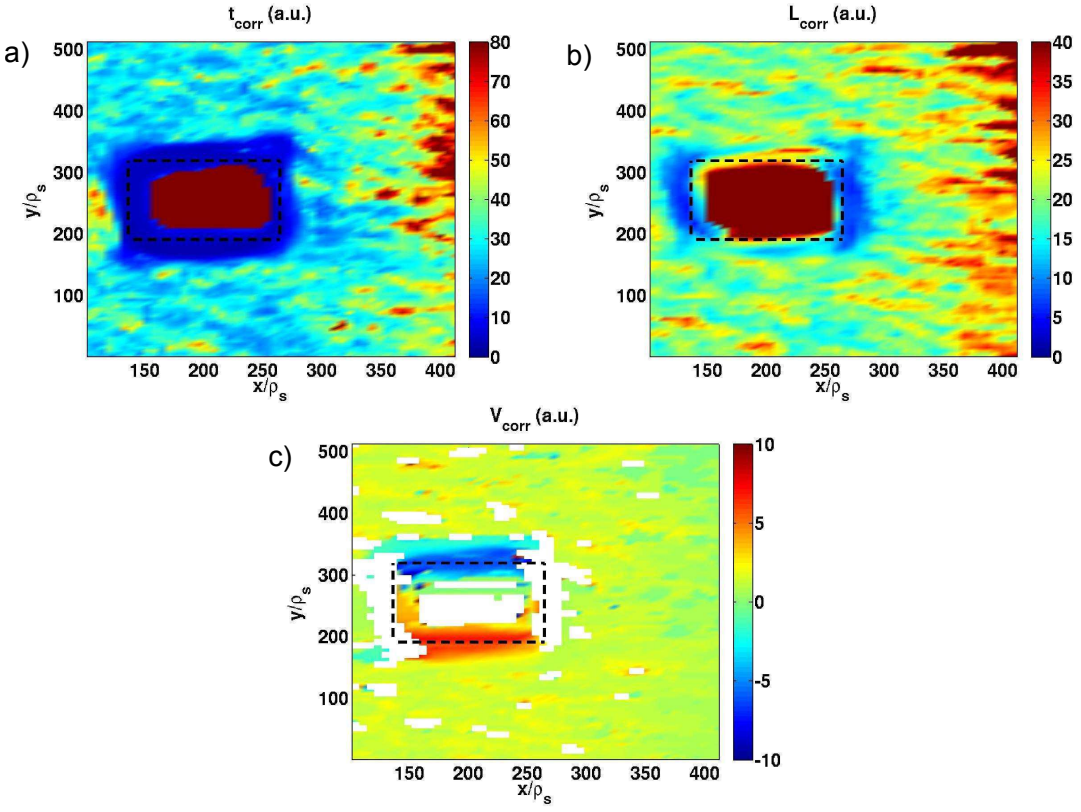

FIGURE 8.9: Turbulence correlation properties in presence of external biasing. a), b) and c) depict the correlation times and lengths and the radial velocities, respectively. A positive radial velocity corresponds to a outwards motion.

The spatial variation of the velocities is first described because the spatial dependences of the correlation lengths and times can be easily understood in the light of the velocity field. The spatial variation of the radial velocity is trivial to understand by taking into account the E×B velocity induced by the polarized domain. The radial velocity is enhanced at the bottom of the polarized domain whereas the direction of the radial velocity is reversed at the top of the polarized domain. Void regions correspond to the positions where there is no time delay with respect to the adjacent radial positions, consequently V_{corr} can not be estimated at these specific positions. This mainly happens inside the polarized domain where almost no fluctuations remain. This also happens at the left and right sides of the polarized domain where the velocity is mainly along the y direction.

As explained previously, t_{corr} is not an intrinsic property of the density fluctuations but depends on the local velocity field. Thus, it is easy to understand why t_{corr} is strongly reduced in the region of steep potential gradient, i.e where the E×B velocity is large.

The decrease of the correlation lengths observed on the right and left parts of the polarized domain might be a consequence of a shearing of the turbulent structures. Far from the polarized domain, the turbulent structure velocity is mainly along the radial direction. When approaching the right or left boundaries of the polarized domain, an important poloidal component adds to the initial velocity. The turbulent structures are torn apart by the local variation of the velocity field leading to a reduction of the radial correlation lengths.

8.3.2 Discussion

The first goal of this section was to qualitatively reproduce the modifications observed during ICRH heating, namely a decrease of the correlation time and an increase of the radial velocity.

The experimental observations were numerically reproduced in a biased plasma only in the potential gradient region. Far from the polarized domain, the turbulence properties remain unchanged with respect to the unbiased case. Given that the rectified potential peaks around 5 cm outside the LCFS and is about 2 cm large, it can not explain the increase (resp. decrease) of the radial velocities (resp. correlation times) measured as far as 20 cm outside the LCFS.

Moreover, the plasma expansion, probably traducing an increase of density in the far SOL, observed when Q5 is powered was not reproduced numerically. Finally, the attentive reader might have already noticed that the direction of the E×B motion at the bottom of the antenna is directed radially inwards, i.e opposite to the radial velocity measured by reflectometry. It has to be noted that the inferred direction of the E×B advection does not only rely on the probes measurement as shown in Fig. 8.6 but also on the postmortem analysis of the antenna limiter [142]: the erosion of the antenna limiter was found to be more pronounced at the midplane consistently with a clockwise E×B advection. The latter argument is very robust and allows us to exclude that the modifications of the turbulence properties originate from the local antenna rectified potential.

8.3.3 Alternative scenarios proposed to explain the ICRH induced SOL modifications

Alternative scenarios have been very recently explored in order to explain the ICRH-induced SOL modifications.

Following the observation of the frequency spectra flattening in ICRH plasma on Tore Supra [133], a bicoherence analysis was performed on probe signals with a very high sampling rate [143]. The bicoherency revealed a possible wave coupling. The ranges of frequencies involved are those of ICRH waves (57 MHz), sound waves (1.7 MHz) and blobby turbulence ($\leq$ 100 kHz). It was suggested that sound waves, excited by ICRH, damp the large turbulent structures. This mechanism might not explain the reflectometer measurements because it does not directly predict an increase of the turbulent structure velocities.

On C-mod, modifications of the SOL properties have been observed far from the powered ICRH antenna [144]. It was proposed that the SOL modifications were indeed due to rectified potentials. Nevertheless, there is a major difference with the rectified potential discussed in the last section. In that case, the rectified potentials result from a partial absorption of the heating wave. A certain amount of ICRH power is reflected from the bulk plasma towards the wall and the rectified potentials build-up where the ICRH waves hit the wall. This scenario was also investigated numerically and and found to agree reasonably well with the experimental data [145].

Assuming that the turbulent modifications observed by reflectometry on Tore supra are, in fact, due to potentials generated by a partial reflection of the ICRH wave, then the electric field at play can be estimated from the measured radial velocity. The measured radial velocity is assumed to be dominated by the $E \times B$ velocity: $V_r = E_\theta / B$ when Q5 is on. The poloidal component of the electric field is therefore easily calculated and is depicted on Fig. 8.10. Evidently, the poloidal electric field peaks at the same

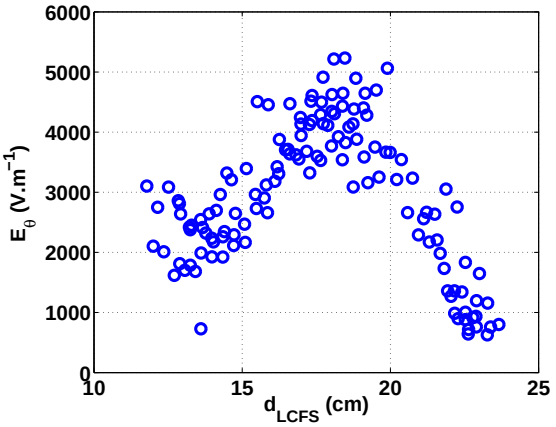

FIGURE 8.10: Poloidal electric field estimated from the measured radial velocities when Q5 is on (new screen, discharges #46996 : 47002). We remind that the leading edge of the antenna limiter is located 3 cm outside the LCFS.

position than the radial velocities, namely around $d_{LCFS} \approx 17$ cm. The poloidal electric field varies between 1000 V.m^{-1} and 5000 V.m^{-1}. These values are larger than those

found with probes on the Q5 antenna (peaking around 1000 V.m^{-1}). This difference suggests that the potentials which cause the modification of the reflectometer signals have different shape than the Q5 lateral limiter potentials (see Fig. 8.6). They might be radially elongated and rather thin along the poloidal direction.

8.4 Summary

In the present chapter, the investigation of turbulence properties in ICRH heated plasma was reported. No significant modification of the turbulence properties was observed in the confined plasma. The analysis was therefore restricted to the SOL region. In ICRH heated plasma, the radial velocities increase with respect to the ohmic case whereas the correlation lengths and times are reduced. These modifications are much more pronounced when the Q5 antenna is powered. Given that Q5 is the closest antenna to the reflectometer, we suspected local mechanisms to be responsible for the turbulence modifications.

The possibility that rectified potentials, generated on the lateral limiter of Q5, would cause the modifications has been explored. To this end, the influence of macroscopic potentials on the turbulence properties have been investigated with the Tokam code. The potentials were found to only impact the turbulence in the vicinity of the biased domain, inconsistently with the experimental observations. Moreover, the direction of the turbulent structure motion induced by the Q5 rectified potentials is opposed to that observed by reflectometry. This last finding evidences that there is no direct causal relation between the modifications of the reflectometer signals in ICRH heated plasma and the rectified potentials measured on the side limiter of the Q5 antenna. Other mechanisms should be invoked to account for the observations, and were briefly presented.

Chapter 9

Conclusion and perspectives

In this work, ultrafast sweeping reflectometry has been used to investigate the fine scale plasma turbulence in Tore Supra tokamak. The sweeping system provides a probing of the plasma from the SOL to the core. By repeating sweeps, the evolution of the electron density and its fluctuations are followed with a fine temporal ($3\mu s$) and relative spatial resolution in the millimeter range. All over this work we demonstrated that the ultrafast sweeping reflectometer, which was updated to such an unprecedented temporal resolution so to provide access to microturbulence scales, is a suitable diagnostics for the characterization and study of turbulence dynamics even though the interpretation of the reflectometer signal remains challenging.

9.1 Main findings

We first attempted to quantify the fluctuation properties via the reconstructed fluctuating density profiles. This attempt was shown to be moderately successful partly due to unexpected signal perturbation at the edge and to the reconstruction algorithm in the frame of the WKB approximation. This results in the reconstructed fluctuation density profiles of artificial radial shifts, which besides lead to unrealistically large correlation lengths in the confined plasma. We were thus confronted to the evidence that with the present treatment, the reconstructed density profiles could not be used to properly infer the density fluctuations properties both in the far SOL and confined region. The reconstructed density profiles though appear not to be affected by the problems mentioned above in the region close to the LCFS. In this specific region, Langmuir probe data were also available to investigate the electron density fluctuations.
The comparison of probe and reflectometer signals was proposed as an indirect reciprocal

validation of those diagnostics, namely regarding the assumptions underlying the respective density fluctuation reconstruction. A good agreement was found between the PDFs, fluctuation levels and skewness measured by both diagnostics. This tends to validate the assumption of negligible temperature fluctuations, on which the evaluation of density fluctuations from probe measurements is based.
The fluctuation time scales of the probe and reflectometer signals were also compared. The reflectometer signals fluctuate systematically faster than the probe signals. This discrepancy might be related to multidimensional effects arising from the relatively large spot size of the reflectometer beam.

Due to the difficulties inherent to the reconstruction of fluctuating density profiles, the properties of the turbulent fluctuations in ohmically heated plasma were therefore investigated on the raw reflectometer signals, as it is presented in Chapter 6. The interpretation of the results became therefore more challenging. Each component of the reflectometer signal, namely the amplitude, phase, real and imaginary part as well as the full complex signal, was analyzed separately as those contain *a priori* different information.

In absence of MHD activity, the fluctuation radial characteristic lengths computed on the diffrent signal components are very similar. They are in the centimetric range in the confined region and the far SOL, while milimetric close to the LCFS. When MHD modes are active, their contributions to the characteristic lengths can be conveniently filtered out by using a coherency analysis to the full complex signal.
It was first assumed that the turbulence properties could directly be deduced from the signal fluctuation properties. Nonetheless, recent numerical simulations (see references cited in section 6.3) have shown that this assumption is not correct, particularly close to the LCFS, where the fluctuation level is large. In these conditions non-linear effects can affect the probing wave response, leading to an underestimate of the correlation length. Consequently, the very small radial correlation lengths observed at the transition between the closed and open field line region are doubtful The correlation time of the fluctuating signals was also investigated. The timescale of the signal can be understood as the time spent by the structure to cross the reflectometer beam spot. In the edge and near SOL plasma, the observed short time scale ($\leq 6\mu s$) was thus possibly attributed due to a large poloidal velocity ($\sim$ km.s^{-1}).
For the first time, the fluctuation properties in the far SOL plasma were characterized with reflectometry as it offers the possibility to probe plasmas with density as low as 10^{16} m^{-3}. Few centimeters outside the LCFS, the fluctuation timescale was observed to increase rapidly up to few hundred μs. There, turbulent structures appear to move radially outwards with a radial velocity of about 200 m.s^{-1}.

The influence of macroscopic plasma parameters on turbulent fluctuations was than studied, as it is presented in the Chapter 7 of the manuscript.
In the confined plasma, the modifications of the signal fluctuation properties observed during a density and current scan were attributed to the underlying variation of electron-electron collisionality. An increase of the collisionality leads to a decrease of the fluctuation radial correlation length. Also, quasi-coherent modes with frequency around 50-100 kHz, are observed within $0.6 \leq r/a \leq 0.75$ at low collisionality, which disappear with an increase of the collisionality. A possible interpretation of the latter observation was proposed in terms of TEM, which stabilize with collisionality, and investigated by a linear stability analysis with the code Qualikiz. This shows an unstable TEM at low collisionality, absent at high. The quasi-coherent modes are thus thought to account for the presence of TEM. A more complete modelling of the observed behaviour would require thorough non-linear simulations including both ions and electron dynamics.
In the far SOL, the radial velocity is observed to decrease when the line average density is ramped up, whereas the correlation length and time are increasing. Simulations with the 2D fluid turbulence code, TOKAM, were performed to understand the effects of density, or equivalently, the collisionality, in the SOL plasma. From this modelling we could infer that the radial velocity is reduced and the small scales are damped, respectively, due to the increase of viscous forces and the broadening of the dissipative range while increasing the collisionality.
Finally, the effect of additional heating was analyzed. In ICRH heated plasmas, an increase of the radial velocity accompanied by a strong decrease of the fluctuation correlation time were observed in the far SOL. Interestingly, these modifications depend on the active antenna and were much more pronounced when the antenna Q5, which is the closer connected to the reflectometer port, was powered. It was first suspected that rectified potentials arising on the Q5 antenna limiter could cause the observed local modifications. However, combined information from probe measurements and numerical simulations with TOKAM, tend to invalidate the locality of the perturbation. Others mechanisms should be invoked to account for these observations.

9.2 Future directions

In previous studies on sweeping reflectometry [27, 28, 46], it was shown that this system could provide information such as the density profiles, the density fluctuation profiles and the wavenumber spectra. This work has extended the possibilities to the radial correlation length, radial velocities and the frequency spectra, up to 160 kHz.
All the analysis techniques mentioned above are now routinely available.
The Doppler shifts observed on the frequency spectra have not been deeply studied but

will surely might bring new information on the plasma rotation and structure of the turbulence.
However, because of reduced experimental campaign, due to a premature interruption of the tokamak Tore Supra, our studies have been restricted to mainly ohmic plasmas and low additional (ICRH) power L-mode plasmas. More systematic analysis in dedicated experiments will be necessary to highlight the parametric dependences of the turbulence. The Tore Supra upgrade (WEST project) with a divertor configuration and new tungsten wall is now undertaken and will provide long duration H-mode discharges by the end of 2015.
In the meantime, measurements are foreseen on the ASDEX Upgrade tokamak in 2014. Hardware upgrades are also planned. The D-band (110-150 GHz), which probes the plasma center, is already being upgraded and will also be able to operate sweeps in 2 μs. Together with the V and W bands, this should provide very promising capabilities for the systematic analysis of the full plasma in various experimental conditions. 1 μs sweeping time with dead time of 0.5 μs is considered for the V (50-75 GHz) and W (75-110 GHz) bands, which is lower than the fluctuation correlation time in the closed field line region. Such a short sampling time will increase the temporal dynamic by a factor of two but also broaden the complex frequency spectra measurements up to 300 kHz instead of 160 kHz.

Still remains the interpretation and specially the understanding of the plasma-wave interaction, which presently is the object of strongly active researches in the community, to access the 'true' plasma turbulence from the reflected signal fluctuations. A promising method, aiming at correcting the measured correlation lengths, has been recently developed [76] and should be applied to the ultrafast sweeping reflectometer data. The coupling of a synthetic reflectometer with non-linear turbulence simulations will greatly improve the understanding of the recorded signals. The characterization of the turbulent structures properties may gain in reliability if the experimental data are systematically interpreted with the help of numerical simulations.

Appendix A

A method for evaluating the uncertainties affecting the experimental skewness

When investigating the SOL turbulence, the skewness is often used as a measure of the intermittency. However, the skewness is a third order statistical moment and requires long time series to converge. The experimental time series from turbulence diagnostics in Tore Supra are generally of a few thousand points leading thus to statistical uncertainties on the skewness estimate. Here, a simple method is presented to evaluate the uncertainty affecting the skewness. The method consists in generating a large number of numerical time series with a known probability distribution, then the deviation between the theoretical and measured skewness is studied with respect to the length of the time series.

A.1 Model for skewed time series

A model for Langmuir probe time series able to reproduce the shape of the experimental PDF was proposed by Sandberg [146], the signal time series is decomposed into

$$w(t) = Z(t) + \gamma Z(t)^2. \tag{A.1}$$

where Z(t) is a zero mean Gaussian process with a standard deviation equal to one. The parameter γ measures the deviation from Gaussianity of $w(t)$. The skewness of such a process is given by

$$S(\gamma) = 2\gamma \frac{3 + 4\gamma^2}{(1 + 2\gamma^2)^{3/2}}. \tag{A.2}$$

Evidently, the skewness is positive for $\gamma > 0$ and tends to S=$2^{3/2}$ for large γ.

Fig. A.1 a) and b) show a 5000 points time series computed according to Eq. A.1 with $\gamma = 0.15$ and the corresponding distribution, respectively.

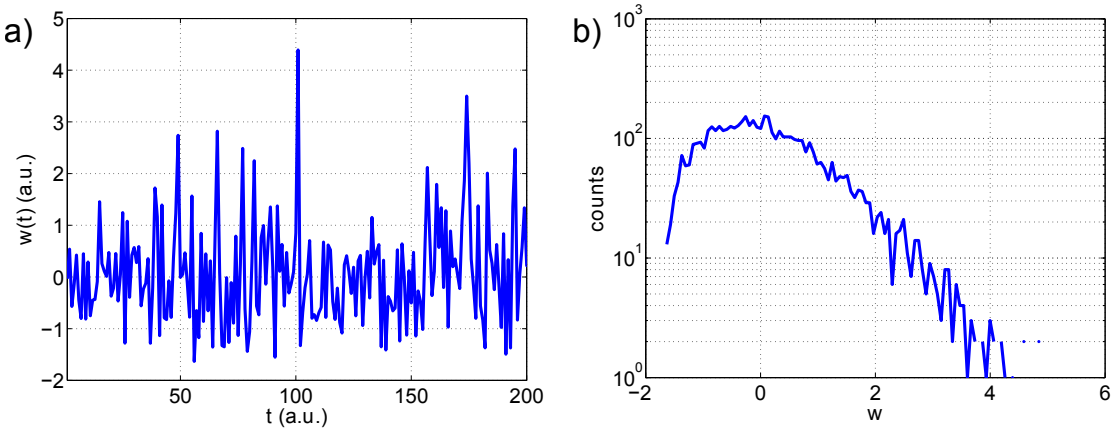

FIGURE A.1: a) Numerical time series computed on 5000 points with $\gamma = 0.15$ and b) its corresponding distribution.

The estimated or measured skewness is $S_m = 0.85$ whereas a theoretical skewness of S_t=0.91 is predicted from Eq. A.2 for $\gamma = 0.15$. The difference between the measured and theoretical skewness is due to the finite length of the time series.

A.2 Method for estimating the error on the measured skewness

Assuming that the experimental time series are well described by Sandberg's model, a numerical experience can be developed to estimate the uncertainty affecting the measured skewness. This method is based on the generation of a large number of numerical time series with different lengths and γ values. The method takes advantage that the *true* (S_t) and estimated skewness (S_m) can be calculated for each time series, consequently statistics can be made on the error $err = S_m - S_t$.

In practice, N=10^4 time series are generated for M=10 distinct time series lengths and P=100 values of γ. The time series length is varied from 10^3 points to 10^4 points by step of 10^3 points. The parameter γ is spaced such that the theoretical skewness varies linearly from 0 to about 2.7.

The definition of the statistical uncertainty is a subtle point. First we want to stress that only the estimated skewness S_m is experimentally known. Also different values of the theoretical skewness S_t can lead to the same value of S_m due to statistical uncertainties. Subsequently, the average deviation between S_m and S_t can be assessed the probability of obtaining S_t for a given value of S_m is known. Thus, a definition for the statistical uncertainty arises quite naturally,

$$\langle err^2 \rangle^{1/2} = \left(\int (S_m - S_t)^2 PDF_{S_m}(S_t) dS_t \right)^{1/2}. \tag{A.3}$$

$\langle err^2 \rangle^{1/2}$ is the root mean square deviation between S_m and S_t and is related to the width of $PDF_{S_m}(S_t)$, the latter being the conditional probability of the true skewness given the measured skewness.

The exact expression of $PDF_{S_m}(S_t)$ is unknown but a discrete sample of the distribution can be obtained from the numerical experience. To this end, the number of event lyings in the interval $[S_m(1-\varepsilon), S_m(1+\varepsilon)]$ is counted for each value of S_t and the associated distribution is built.

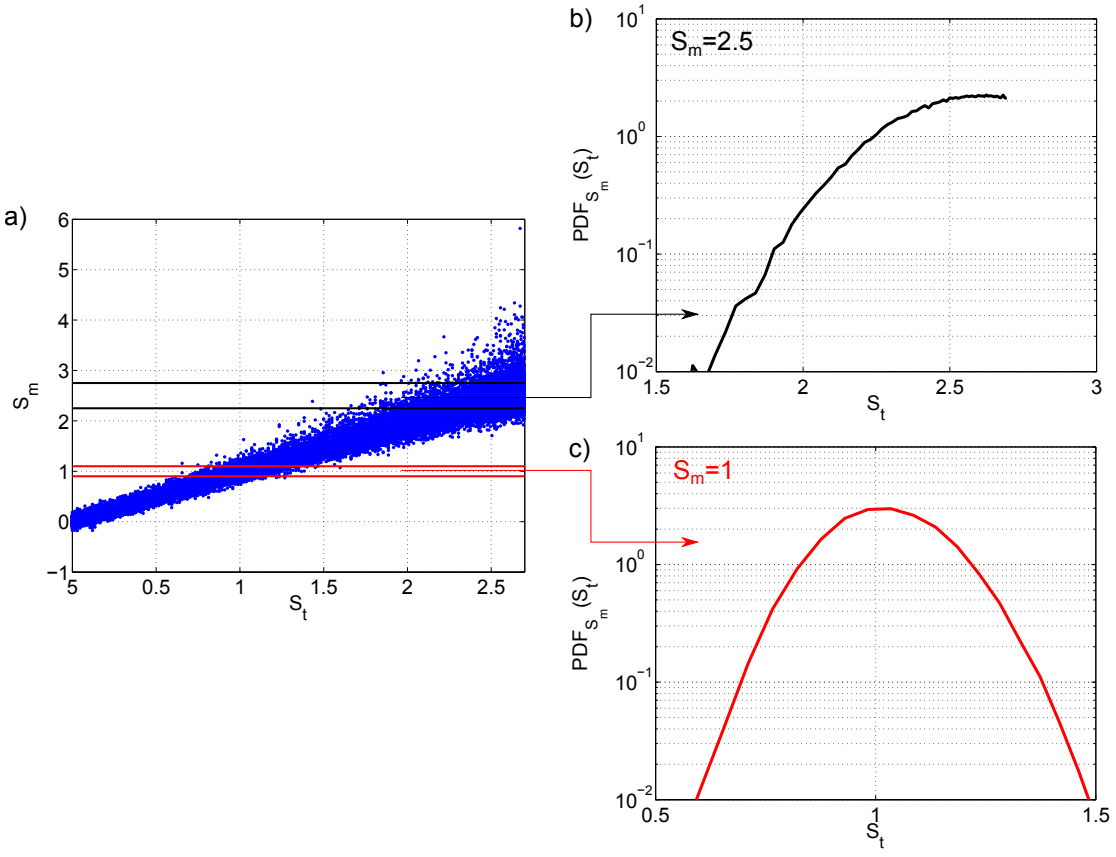

FIGURE A.2: a) Measured skewness with respect to the underlying theoretical skewness. Here, 10^3 points long time series are used. $PDF_{S_m}(S_t)$ are shown on b) and c) for $S_m = 2.5$ and $S_m = 1$, respectively.

The procedure is illustrated in Fig. A.2 with 10^3 points long time series. The intervals on which the distributions are computed are also shown. Note that, $\varepsilon = 10\%$ has been used for the purpose of illustration. However, $\varepsilon = 2\%$ is enough to obtain a sufficiently sampled distribution when applying the method to the experimental data.

Fig. A.2 b) depicts the distribution obtained for $S_m = 2.5$. In this case, the distribution does not drop to zero because S_m is too close to the boundaries of the computing interval ($S_m \in [0, 2.7]$). Consequently, the uncertainty can not be properly inferred for such a high value of S_m. The application of the method is only valid for the interval $S_m \in [0.3, 2]$, which is relevant for most of the experimental situations.

Fig. A.2 c) shows the distribution obtained for $S_m = 1$. In this case, the distribution is well-behaved and the corresponding quadratic error is $\langle err^2 \rangle^{1/2} = 0.13$.

Finally, the quadratic errors are computed for different lengths of the time series. The quadratic error curves are shown in Fig. A.3 for 1000, 5000 and 10000 points time series.

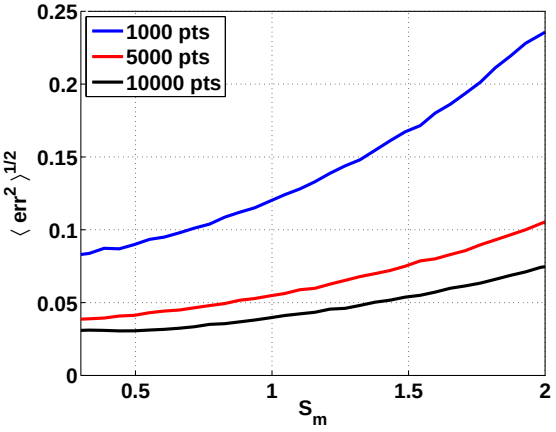

FIGURE A.3: Numerical abacus of the quadratic error affecting the skewnes

Unsurprisingly, the quadratic error increases with the measured skewness and decreases with the length of the time series. The quadratic error is rather small even for 1000 points time series. This is quite encouraging and gives a relative confidence in the skewness measured experimentally. The curves are used as abacuses to estimate the experimental uncertainty. As the lengths of the experimental time series do not generally match the lengths of the numerical time series, the experimental uncertainty is obtained by interpolating the numerical uncertainty.

The main finding of this method is that the statistical uncertainty affecting the skewness is surprisingly small even for short time series. However, this method is based on the strong assumption that experimental time series can be expressed in the form of Eq. A.1. The reliability of this model is questionable given that it does not account for the long correlation time commonly observed in the SOL. Nevertheless, the above method

concerns the statistical properties of the time series which should, at priori, be insensitive to the dynamical properties of the system.

More recently, O. Garcia has proposed a stochastic model accounting for both the statistical and dynamical properties of the probe time series [147]. It will be very interesting to include Garcia's model in our method in other to investigate if a dependence exists between the statistical and dynamical properties of the system.

Appendix B

Considerations on the beam spot size

The spot size is a key parameter to interpret the reflectometer signals. The spot size is directly linked to the antenna radiation pattern which tells us how large is the fraction of the radiated energy in a given direction. The radiation pattern depends mainly on the antenna geometry. The emitting and receiving antennas are 3.2 cm square horn antennas. Fig. B.1 b) and c) show the radiation pattern calculated in the far field region, for two frequencies in the $(\vec{E},\vec{k})$ and $(\vec{H},\vec{k})$ planes, respectively. Taking $\vec{k}$ aligned to the antenna axis, $(\vec{E},\vec{k})$ and $(\vec{H},\vec{k})$ correspond approximately to the poloidal and toroidal planes, respectively. The radiation patterns show clearly that the width of the central lobe is larger for low frequency waves. The angle, for which the fraction of the radiated power is reduced by -3 dB defines the spot size.

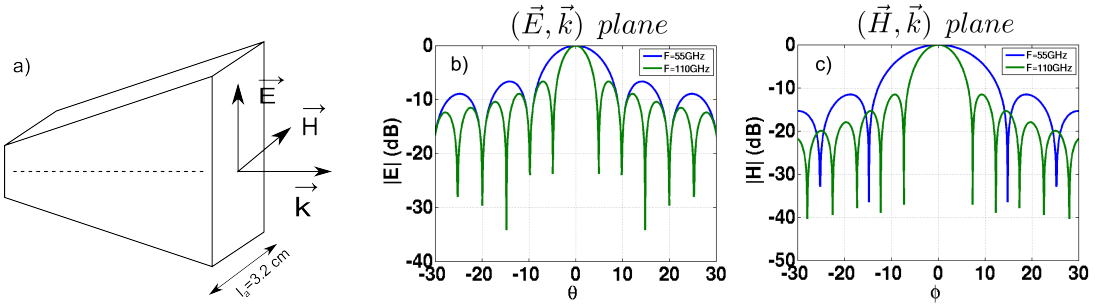

FIGURE B.1: a) Schematic view of the antenna horn. b) radiation diagram for two frequencies in the $(\vec{E},\vec{k})$ plane. c) radiation diagram for two frequencies in the $(\vec{E},\vec{k})$

To evaluate the spot size, one has also to know the distance traveled by the wave between the antenna and the cutoff position. The antenna is located 4.26 m away from Tore Supra vertical axis. The link between the probing frequency and the cut-off position is obtained through the density profile. Fig. B.2 shows the spot sizes in the poloidal and toroidal

planes using Tore Supra #47170 density profile. $D_E \approx 16$ cm and $D_H \approx 22$ cm are the spot sizes in the poloidal and toroidal planes, respectively. The spot sizes have only a weak dependence with respect to the radial position. Larger distances traveled by high frequencies waves are compensated by a narrowing of the radiation pattern. Note that the spot size was evaluated with geometric optics. Effects like refraction, due to the propagation through the plasma, were note taken into account.

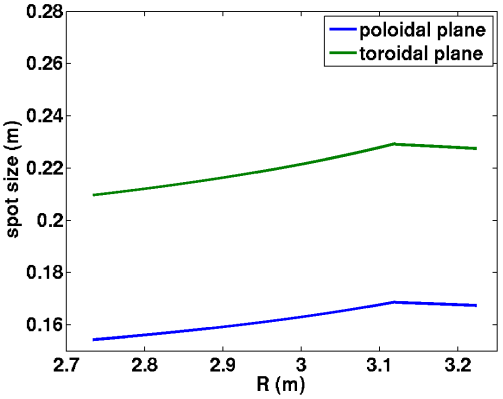

FIGURE B.2: Beam spot sizes evaluated in the poloidal and toroidal planes with respect to the radial cut-off position for #47170 plasma parameters ($B_0 = 3.38T$, $\langle n_e \rangle = 6.310^{18}$ and $Ip = 0.6MA$).

In the following, the spot size is compared to the plasma characteristic lengths, namely the cutoff layer curvature and the turbulent structure size, in order to study its potential impact on the measurements interpretation.

B.1 Mean plasma curvatures

First, the plasma cut-off layers are considered as smooth mirrors curved in both the toroidal and poloidal directions. In the toroidal direction, two disctinct radii of curvature have to be taken into account. The mean toroidal curvature can be fairly estimated by the tokamak major radius. It is found that $D_H/2\pi R_0 << 1$, meaning that the mean toroidal curvature does not play a significant role. Tore Supra is subject to a significant ripple (due to the finite number of poloidal coils) which bends locally the field lines and thus the cutoff layers. Fig. B.3 illustrates the bending of the refraction index contours on Tore Supra. In the SOL, the refraction index contours are only marginally bent on a distance comparable to the toroidal spot size. Moreover, the effect of magnetic ripple is lower when going towards the plasma core.

Fig. B.4 shows the position of cutoff layers on a poloidal cross section calculated with $B = 4$ T and $n_{e0} = 5\ 10^{19}\ m^{-3}$. Again, the cutoff layers curvature is low on a distance of the order of the poloidal spot size.

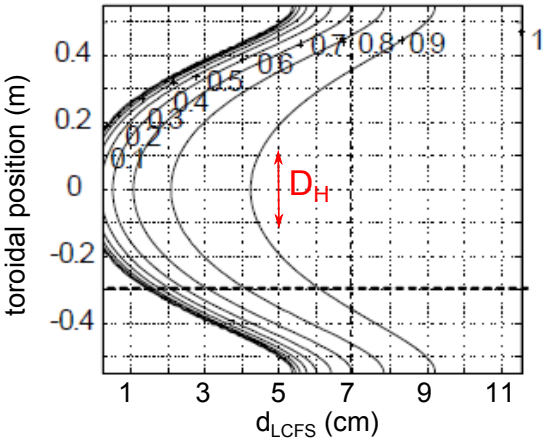

FIGURE B.3: Bending of the refraction index contours due to the magnetic ripple in the Tore Supra SOL. The red arrow represents the toroidal spot size. d_{LCFS} denotes the distance to the LCFS. Adapted from [148].

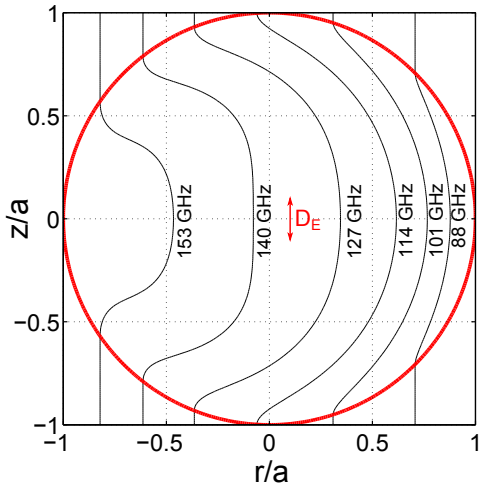

FIGURE B.4: Position of the X-mode cutoff layers on a poloidal cross section for different probing frequencies. The red arrow represents the poloidal spot size. Adapted from [148].

B.2 Plasma turbulence

Additionally to the toroidal and poloidal curvatures, the cutoff layers are deformed by electron density fluctuations. Here, the characteristic scale lengths of the fluctuations are compared to the spot sizes. To this end, the cutoff layers are now represented by corrugated mirrors.

In the poloidal direction, the turbulence structure size is generally centimetric in tokamak core plasmas [149–151] thus smaller than the poloidal spot size. Because of the strong anisotropy of the magnetic field, the particles parallel velocity is much larger than the perpendicular velocitiy. Consequently, the turbulent structures are elongated along the magnetic field with typical length $L_{\|} = 2\pi qR$, q being the safety factor. The safety factor

q is around unity at the plasma center leading to a parallel length $L_{\|} \approx 15m$ which is much bigger than the spot size. However the tilt angle α of the field line has also to be taken into account. Let's call h the distance traveled by the structure in the poloidal plane on the spot size. If h is small with respect to the poloidal spot size, then the turbulence can be considered homogeneous in the toroidal direction. Fig. B.5 illustrates the situation.

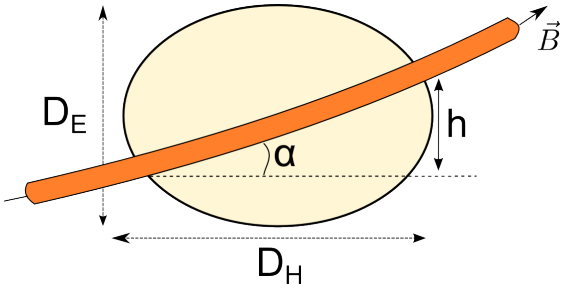

FIGURE B.5: Schematic representation of the tilt of a turbulent structure elongated on a magnetic field line on the illuminated plasma area.

From elementary trigonometry,

$$\frac{h}{D_E} \approx \frac{D_H}{D_E}\frac{r}{qR}. \tag{B.1}$$

Using realistic values of q, the condition $h/D_E << 1$ is fulfilled from the core to the LCFS.

In this discussion, it was shown that the effects of the mean plasma curvatures are not significant on the reflection of the probing wave on the plasma cutoff layer. Taking into account that the irregularities are elongated along the magnetic field lines, only the poloidal size of the structure are smaller than the spot size. Consequently, the modeling of the plasma waves interaction can be restricted, at the first order, to the $r - \theta$ plane in slab geometry.

Appendix C

Comments on the frequency spectra asymmetries

As mentionned in Sec. 7.1.1 and 7.1.2, the observed frequency spectra asymmetries are caused by Doppler shifts. It is yet not fully understood how the plasma motion can lead to the observed spectra. Nevertheless, it is worth to present the main mechanisms which are susceptible to generate the frequency shifts.

Doppler shifts have already been reported on correlation reflectometry spectra. For example, a correlation between the direction of the parallel velocity and the sign of the frequency shift was observed in TEXTOR [103]. It was consequently suggested that the asymmetry of the spectra originates from the parallel velocity.
On Tore Supra, frequency shifts are observed in the edge region on the fixed frequency reflectometer signals. These frequency shifts are attributed to a significant ripple and a non-zero toroidal angle of incidence of the reflectometer beam.

We remind that a plasma moving at a velocity $\vec{V}$ creates a frequency shift Δw on the electromagnetic wave with wave vector $\vec{k}$,

$$\Delta w = \vec{k} \cdot \vec{V}. \tag{C.1}$$

Expanding this relation in the reflectometer frame[1] $(\vec{x}, \vec{y}, \vec{z})$ gives

$$\Delta w = k_x V_x + k_y V_y + k_z V_z. \tag{C.2}$$

[1]The reflectometer frame is illustrated in Fig. C.2.

Contrary to the fixed frequency system, the ultrafast sweeping reflectometer was designed to probe the plasma at normal incidence. Consequently $k_x >> k_y$, $k_z \approx 0$, and the $k_y V_y$ and $k_z V_z$ terms are neglected in the following.

C.1 Doppler shift due to the radial motion of the plasma

Assuming that a global plasma motion along the radial direction is responsible for the observed frequency shifts. As the reflectometer is located in the tokamak midplane, $V_x \approx V_r$. The observed doppler shift is of the order of $\Delta w \approx 20\, kHz$, and the characteristic wavenumber close to the cutoff, $k_x \approx 1\, cm^{-1}$, then a net radial velocity $V_r \approx 500\, m\, s^{-1}$ is obtained. Such a large radial velocity would lead to a very poor confinement of the density due to a strong advection. Consequently, a net radial motion of the plasma is not suitable to explain the Doppler shifts.

C.2 Doppler shift due to the poloidal motion of the plasma

Some insight on the mechanisms underlying the Doppler shift can be obtained by analysing specific experiments during which the contact point between the plasma and the vacuum vessel is modified. During the discharges #47182 and #47183, the contact point was varied from bottom to top, respectively. The plasma poloidal cross sections are depicted on Fig. C.1 as well as the corresponding frequency spectra. Note that apart from the contact point and geometry, the plasma parameters are similar for discharges #47182 and #47183.

The Doppler shift is positive for the plasma limited at the top of the vessel whereas the Doppler shift is negative for the bottom limited plasma. This observation supports the idea that the Doppler effect is, at least partially, due to a counter clockwise poloidal rotation of the plasma. For bottom limited plasmas and density structures rotating poloidally in the electron diagmagnetic direction, the reflectometer *detects* the structure as it was moving radially away. This leads to the experimentally observed negative Doppler shift. Contrarily, if the plasma is top limited, a poloidally rotating density structure appears as it were approaching to the reflectometer when crossing the reflectometer beam.

The effective radial velocity originating from the poloidal plasma motion can be estimated as illustrated in Fig. C.2.

If the structure moves poloidally with a constant velocity V_θ, the effective velocity perceived by the reflectometer is the projection of the poloidal velocity on the reflectometer

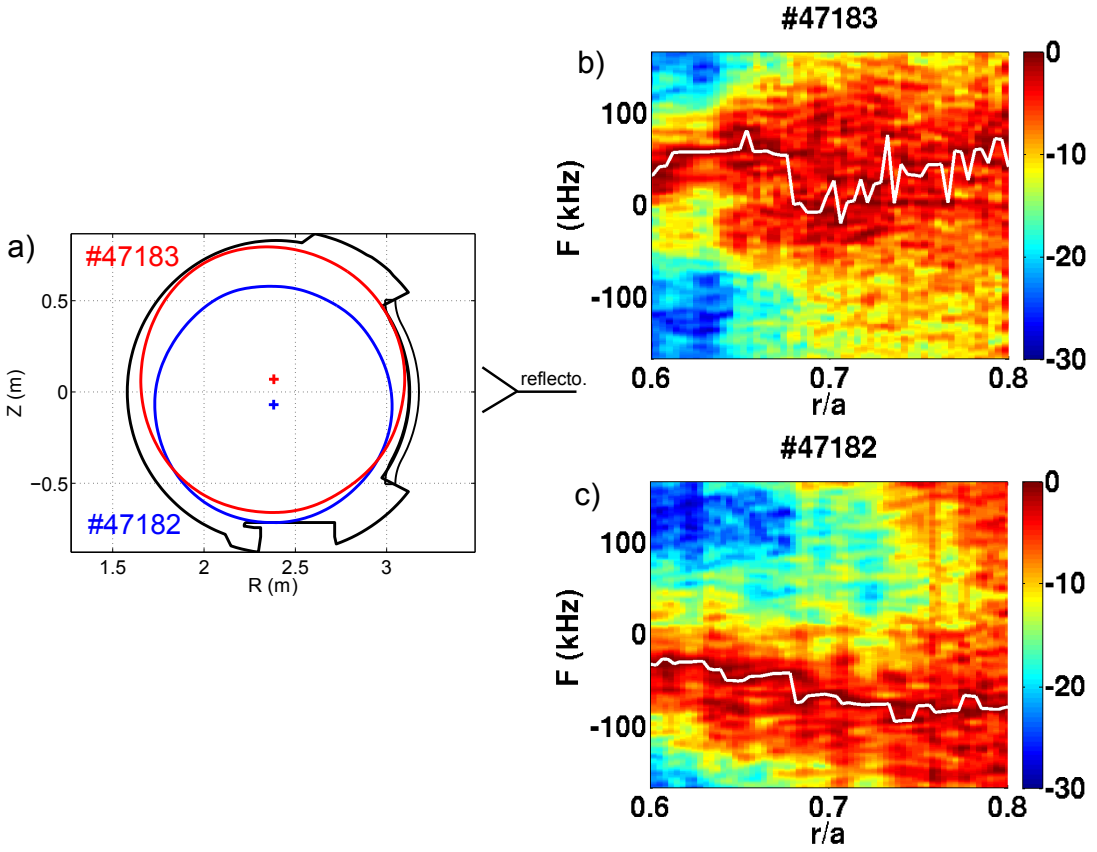

FIGURE C.1: a) Position of the plasma in the Tore Supra vacuum vessel. The plasma center was shifted of $\Delta z = \pm 8$ cm with respect to the midplane. b) and c) show the frequency spectra corresponding to plasma with top and low contact points, respectively. The white curves highlight the frequencies for which the spectra peak.

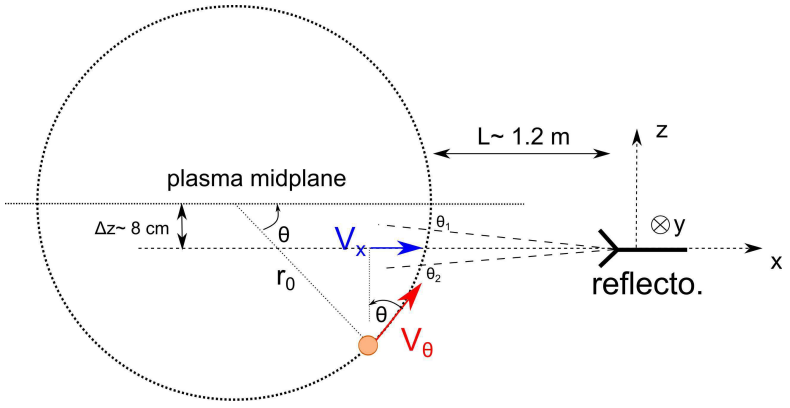

FIGURE C.2: Schematic explanation of the Doppler shift for a top limited plasma.

axis $V_x(\theta) = V_\theta \sin(\theta)$. The resulting Doppler shift is $\Delta w = k_x \langle V_x \rangle_\theta$ where $\langle V_x \rangle_\theta$ is the effective velocity averaged on the beam spot,

$$\langle V_x \rangle_\theta = \frac{1}{\theta_1 - \theta_2} \int_{\theta_2}^{\theta_1} V_x(\theta) d\theta. \tag{C.3}$$

Here, θ_1 and θ_2 are the angles corresponding to the intersection of the beam spot and the poloidal layer. θ_1 and θ_2 can be calculated from θ_b, the aperture of the probing beam, and on the reflectometer position through r_0, L and Δz as defined in Fig. C.2. Using $\theta_b = 3°$, $\Delta z = 8$ cm, $r_0 = 0.7a \approx 50$ cm, and $V_\theta = 2\, km.s^{-1}$ (typical velocity measured by Doppler reflectometry in the edge plasma), the Doppler shift is of the order of 30 kHz. The Doppler shift found with this simplified model agrees within one order of magnitude with the experimental values.

C.3 Local inversions of the Doppler shift

No attention was paid to the detailed evolution of the Doppler shift so far. Nevertheless, the peak frequency position generally varies with respect to the radial position. The peak frequency can even change its sign when the MHD activity is strong as depicted in Fig. C.3 a). On this example, the position of the Doppler shift inversions are clearly correlated with the MHD mode as observed on the phase signals (Fig. C.3 b).

Localized inversions of the peak frequency have already been observed with Doppler reflectometry in the core region of Tore Supra [152]. Change of signs of the radial electric field were proposed to account for the inversion of the Doppler spectra.

Nonetheless, the detailed shape of the frequency spectra are not fully understood and require further investigations. We suspect that the shape of the poloidally rotating turbulent structures, and especially their tilt angle, contribute significantly to the Doppler shifts and to the observed change of signs.

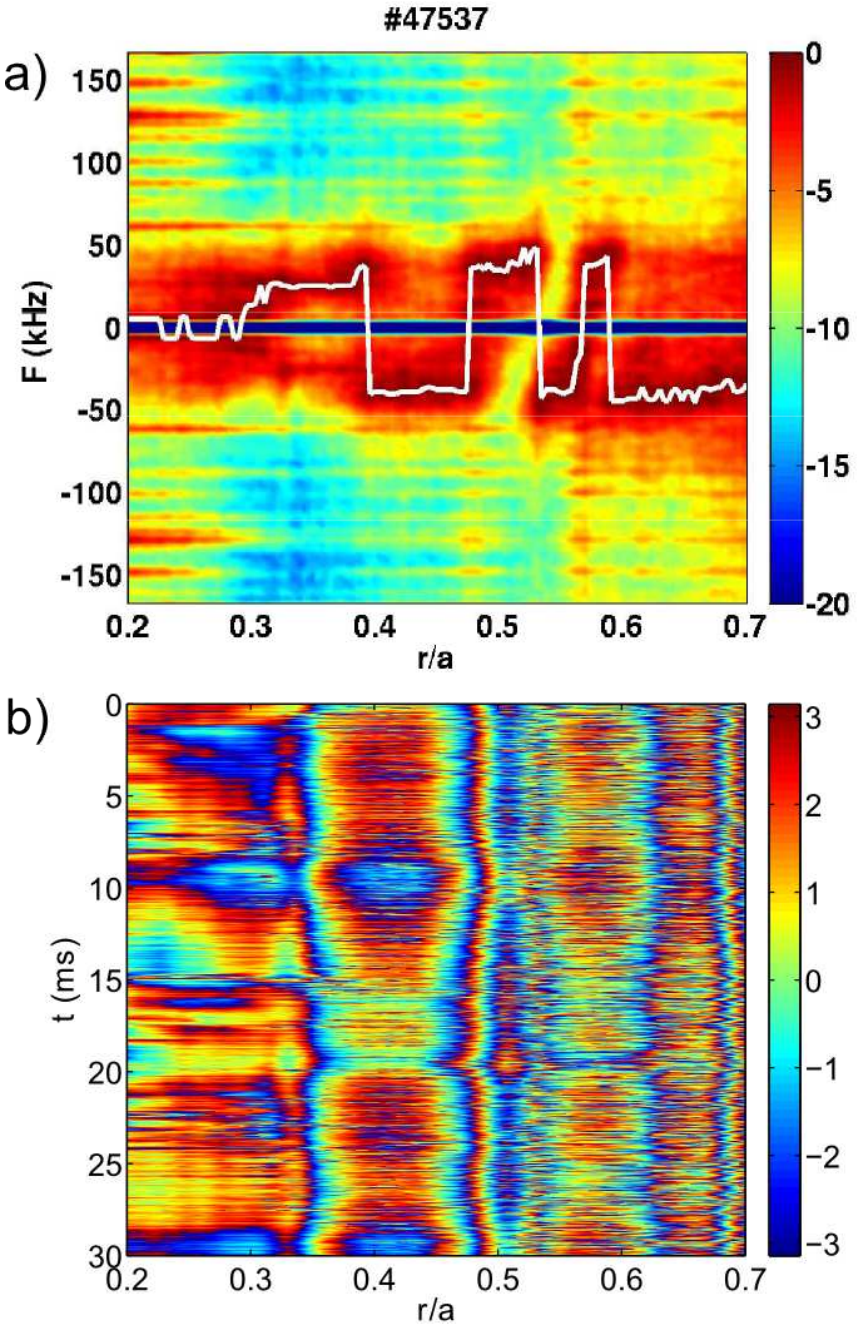

FIGURE C.3: a) frequency spectrum with local inversions of the Doppler shift, b) corresponding phase signals.

Bibliography

[1] JD Lawson. Some criteria for a power producing thermonuclear reactor. *Proceedings of the Physical Society of London section B*, 70(1):6–10, 1957.

[2] Y Sarazin. Turbulence and transport. Lecture given in the french master in fusion sciences.

[3] J. Wesson. *Tokamaks*. International Series of Monographs on Physics. OUP Oxford, 2011.

[4] W Horton. Drift waves and transport. *Rev. Mod. Phys.*, 71(3):735–778, 1999.

[5] M Ottaviani and G Manfredi. The gyro-radius scaling of ion thermal transport from global numerical simulations of ion temperature gradient driven turbulence. *Phys. Plasmas*, 6(8):3267–3275, 1999.

[6] W. Horton. *Turbulent transport in magnetized plasmas*. World Scientific, Singapore, 2013.

[7] Paulett C. Liewer. Measurements of microturbulence in tokamaks and comparisons with theories of turbulence and anomalous transport. *Nuc. Fusion*, 25(5):543, 1985.

[8] N. Bretz. Diagnostic instrumentation for microturbulence in tokamaks. *Rev. Sci. Instrum.*, 1997.

[9] U. Stroth. *Confinement, Transport and Collective Effects in Plasma Physics*. Springer-Verlag, Berlin, Germany, 2005.

[10] S. Chandrasekhar. *Hydrodynamic and Hydromagnetic Stability*. Oxford University Press, London, England, 1961.

[11] MA Beer and GW Hammett. Toroidal gyrofluid equations for simulations of tokamak turbulence. *Phys. Plasmas*, 3(11):4046–4064, 1996.

[12] S Brunner, M Fivaz, TM Tran, and J Vaclavik. Global approach to the spectral problem of microinstabilities in tokamak plasmas using a gyrokinetic model. *Phys. Plasmas*, 5(11):3929–3949, 1998.

[13] BB Kadomtsev and OP Pogutse. Theory of beam-plasma interaction. *Phys. Fluids*, 14(11):2470, 1971.

[14] E.J. Doyle (Chair Transport Physics), W.A. Houlberg (Chair Confinement Database, Modelling), Y. Kamada (Chair Pedestal, Edge), V. Mukhovatov (co Chair Transport Physics), T.H. Osborne (co Chair Pedestal, Edge), A. Polevoi (co Chair Confinement Database, Modelling), G. Bateman, J.W. Connor, J.G. Cordey (retired), T. Fujita, X. Garbet, T.S. Hahm, L.D. Horton, A.E. Hubbard, F. Imbeaux, F. Jenko, J.E. Kinsey, Y. Kishimoto, J. Li, T.C. Luce, Y. Martin, M. Ossipenko, V. Parail, A. Peeters, T.L. Rhodes, J.E. Rice, C.M. Roach, V. Rozhansky, F. Ryter, G. Saibene, R. Sartori, A.C.C. Sips, J.A. Snipes, M. Sugihara, E.J. Synakowski, H. Takenaga, T. Takizuka, K. Thomsen, M.R. Wade, H.R. Wilson, ITPA Transport Physics Topical Group, ITPA Confinement Database, Modelling Topical Group, ITPA Pedestal, and Edge Topical Group. Chapter 2: Plasma confinement and transport. *Nuc. Fusion*, 47(6):S18, 2007.

[15] L. Villard, A. Bottino, S. Brunner, A. Casati, J. Chowdhury, T. Dannert, R. Ganesh, X. Garbet, T. Goerler, V. Grandgirard, R. Hatzky, Y. Idomura, F. Jenko, S. Jolliet, S. Khosh Aghdam, X. Lapillonne, G. Latu, B. F. McMillan, F. Merz, Y. Sarazin, T. M. Tran, and T. Vernay. Gyrokinetic simulations of turbulent transport: size scaling and chaotic behaviour. *Plasma Phys. Control. Fusion*, 52(12, 2), 2010.

[16] T Dannert and F Jenko. Gyrokinetic simulation of collisionless trapped-electron mode turbulence. *Phys. Plasmas*, 12(7), 2005.

[17] T. Goerler and F. Jenko. Multiscale features of density and frequency spectra from nonlinear gyrokinetics. *Phys. Plasmas*, 15(10), 2008.

[18] I. Furno, B. Labit, A. Fasoli, F. M. Poli, P. Ricci, C. Theiler, S. Brunner, A. Diallo, J. P. Graves, M. Podesta, and S. H. Mueller. Mechanism for blob generation in the TORPEX toroidal plasma. *Phys. Plasmas*, 15(5), 2008.

[19] JA Boedo, D Rudakov, R Moyer, S Krasheninnikov, D Whyte, G McKee, G Tynan, M Schaffer, P Stangeby, P West, S Allen, T Evans, R Fonck, E Hollmann, A Leonard, A Mahdavi, G Porter, M Tillack, and G Antar. Transport by intermittent convection in the boundary of the DIII-D tokamak. *Phys. Plasmas*, 8(11):4826–4833, 2001.

[20] S. I. Krasheninnikov, D. A. D'Ippolito, and J. R. Myra. Recent theoretical progress in understanding coherent structures in edge and SOL turbulence. *J. Plasma Phys.*, 74(5):679–717, OCT 2008.

[21] D. A. D'Ippolito, J. R. Myra, and S. J. Zweben. Convective transport by intermittent blob-filaments: Comparison of theory and experiment. *Phys. Plasmas*, 18(6), 2011.

[22] SI Krasheninnikov. On scrape off layer plasma transport. *Phys. Lett. A*, 283(5-6):368–370, 2001.

[23] F Simonet. Measurement of electron-density profile by microwave reflectometry on tokamaks. *Rev. Sci. Instrum.*, 56(5):664–669, 1985.

[24] H Bottollier-Curtet. *Réflectométrie hyperfréquence pour la détermination de la densié électronique et de ses fluctuations sur le tokamak Pétula B.* PhD thesis, Université Paris-XI, Orsay, 1986.

[25] H BottollierCurtet and G Ichtchenko. Microwave reflectometry with the extraordinary mode on tokamaks - determination of the electron-density profile of Petula-B. *Rev. Sci. Instrum.*, 58(4):539–546, 1987.

[26] P Moreau, F Clairet, JM Chareau, M Paume, and C Laviron. Ultrafast frequency sweep heterodyne reflectometer on the Tore Supra tokamak. *Rev. Sci. Instrum.*, 71(1):74–81, 2000.

[27] L Vermare. *Mesures de l'activité magnétohydrodynamique et de la micro-turbulence par réflectométrie à balayage.* PhD thesis, Université Aix-Marseille I, 2005.

[28] T Gerbaud. *Etude de la microturbulence par réflectométrie dans un plasma de fusion sur le tokamak Tore-Supra.* PhD thesis, Université Henri Poincaré, Nancy I, 2008.

[29] M Lennholm, G Agarici, G Berger-By, P Bosia, F Bouquey, E Cellier, J Clary, M Clapit, C Darbos, G Giruzzi, M Jung, R Magne, D Roux, JL Segui, E Traisnel, and X Zou. The ECRH/ECCD system on tore supra, a major step towards continuous operation. *Nuc. Fusion*, 43(11):1458–1476, 2003.

[30] P Bibet, A Ekedahl, P Froissard, F Kazarian, E Bertrand, S Dutheil, and L Tanaskovic. Coupling and power handling of the new Tore Supra LHCD launcher. *Fusion Eng. Des*, 56-57:679–684, 2001.

[31] L. Colas, V. Basiuk, B. Beaumont, A. Becouelt, G. Bosia, S. Bremond, M. Chantant, R. Clairet, A. Ekedahl, E. Faudot, A. Geraud, M. Goniche, S. Heuraux, G. T. Hoang, G. Lombard, L. Millon, R. Mitteau, P. Mollard, K. Vulliez, and Tore Supra Team. Key results of long pulse ICRH operation in Tore Supra. *Nuc. Fusion*, 46(7):S500–S513, 2006.

[32] I. Langmuir and H. M. Mott-Smith. *Gen. Elect. Rev.*, 26:731, 1923.

[33] C. Hidalgo, R. Balbin, M. A. Pedrosa, I. Garcia-Cortes, and M. A. Ochando. Experimental evidence of significant temperature fluctuations in the plasma edge region of the tj-i tokamak. *Phys. Rev. Lett.*, 69:1205–1208, Aug 1992.

[34] L. Giannone, R. Balbín, H. Niedermeyer, M. Endler, G. Herre, C. Hidalgo, A. Rudyj, G. Theimer, and Ph. Verplanke W7-AS Team. Density, temperature, and potential fluctuation measurements by the swept langmuir probe technique in wendelstein 7-as. *Physics of Plasmas*, 1(11):3614–3621, 1994.

[35] D. L. Rudakov, J. A. Boedo, R. A. Moyer, R. D. Lehmer, G. Gunner, and J. G. Watkins. Fast electron temperature diagnostic based on langmuir probe current harmonic detection on diii-d. *Rev. Sci. Instrum.*, 72(1):453–456, 2001.

[36] J. P. Gunn and J. Y. Pascal. A magnetically driven reciprocating probe for tokamak scrape-off layer measurements. *Rev. Sci. Instrum.*, 82(12), 2011.

[37] J. P. Gunn, J. Y. Pascal, F. Saint-Laurent, and C. Gil. Electric Probes in Tokamaks: Experience in Tore Supra. *Contrib. Plasma Phys.*, 51(2-3, SI):256–263, MAR 2011.

[38] R. Sabot, A. Sirinelli, J. M. Chareau, and J. C. Giaccalone. A dual source D-band reflectometer for density profile and fluctuations measurements in Tore-Supra. *Nuc. Fusion*, 46(9):S685–S692, 2006.

[39] P Hennequin, C Honore, A Truc, A Quemeneur, N Lemoine, JM Chareau, and R Sabot. Doppler backscattering system for measuring fluctuations and their perpendicular velocity on Tore Supra. *Rev. Sci. Instrum.*, 75(10, Part 2):3881–3883, 2004.

[40] F Clairet, R Sabot, C Bottereau, JM Chareau, M Paume, S Heuraux, M Colin, S Hacquin, and G Leclert. X-mode heterodyne reflectometer for edge density profile measurements on Tore Supra. *Rev. Sci. Instrum.*, 72(1, Part 2):340–343, 2001.

[41] F. Clairet, S. Heuraux, C. Bottereau, D. Molina, L. Ducobu, F. Leroux, and A. Barbuti. Fast sweeping reflectometry upgrade on Tore Supra. *Rev. Sci. Instrum.*, 81(10), 2010.

[42] R Sabot, C Bottereau, JM Chareau, F Clairet, and M Paume. Single sideband modulator, a key component of Tore-Supra heterodyne reflectometers. *Rev. Sci. Instrum.*, 75(8):2656–2659, 2004.

[43] V.L. Ginzburg. *Propagation of electromagnetic waves in plasma.* Russian monographs and texts on advanced mathematics and physics. Gordon and Breach.

[44] E Mazzucato. Microwave reflectometry for magnetically confined plasmas. *Rev. Sci. Instrum.*, 69(6):2201–2217, 1998.

[45] R. Fitzpatrick. *Introduction to Plasma Physics: A Graduate Level Course*. Lulu.com, 2006.

[46] Ph Moreau. *Développement d'un réflectomètre micro-onde hétérodyne à balayage ultra rapide*. PhD thesis, Université Aix-Marseille I, 1997.

[47] R Nazikian, GJ Kramer, and E Valeo. A tutorial on the basic principles of microwave reflectometry applied to fluctuation measurements in fusion plasmas. *Phys. Plasmas*, 8(5, Part 2):1840–1855, 2001.

[48] C Fanack. *Etude analytique et numérique de la réflectométrie dans un plasma fluctuant. Modeèles à une et deux dimensions*. PhD thesis, Université Henri Poincaé, Nancy I, 1997.

[49] Thomas Howard Stix. *Waves in Plasmas*. Springer, 1992.

[50] C Laviron, AJH Donne, ME Manso, and J Sanchez. Reflectometry techniques for density profile measurements on fusion plasmas. *Plasma Phys. Control. Fusion*, 38(7):905–936, 1996.

[51] JC Forster, PM Schoch, RL Hickok, and WC Jennings. Study of density and potential fluctuations in the Text tokamak with a heavy-ion beam probe. *IEEE T. Plasma. Sci.*, 22(4):359–362, AUG 1994.

[52] T. L. Rhodes, W. A. Peebles, J. C. Deboo, R. Prater, J. E. Kinsey, G. M. Staebler, J. Candy, M. E. Austin, R. V. Bravenec, K. H. Burrell, J. S. deGrassie, E. J. Doyle, P. Gohil, C. M. Greenfield, R. J. Groebner, J. Lohr, M. A. Makowski, X. V. Nguyen, C. C. Petty, W. M. Solomon, H. E. St John, M. A. Van Zeeland, G. Wang, and L. Zeng. Broad wavenumber turbulence and transport during ohmic and electron cyclotron heating in the DIII-D tokamak. *Plasma Phys. Control. Fusion*, 49(12B):B183–B193, DEC 2007. 34th European-Physical-Society Conference on Plasma Physics, Palace Culture & Sci, Warsaw, POLAND, JUL 02-06, 2007.

[53] D. A. et al. Shelukhin. X-mode lower cutoff high field side reflectometer for electron density profile measurements in t-10 tokamak. In *Proc. 11th Intl. Reflectometry Workshop - IRW11 (Palaiseau, April 2013)*, 2013.

[54] L. Vermare, S. Heuraux, F. Clairet, G. Leclert, and F. da Silva. Density fluctuation measurements using X-mode fast sweep reflectometry on Tore Supra. *Nuc. Fusion*, 46(9):S743–S759, 2006.

[55] F. Clairet, B. Ricaud, F. Briolle, S. Heuraux, and C. Bottereau. New signal processing technique for density profile reconstruction using reflectometry. *Rev. Sci. Instrum.*, 82(8), 2011.

[56] T. Gerbaud, F. Clairet, R. Sabot, A. Sirinelli, S. Heuraux, G. Leclert, and L. Vermare. Comparison of density fluctuation measurements between O-mode and X-mode reflectometry on Tore Supra. *Rev. Sci. Instrum.*, 77(10), 2006.

[57] M. Kocan, J. P. Gunn, J. Y. Pascal, and E. Gauthier. Ion Temperature Measurements in the Tore Supra Scrape-Off Layer Using a Retarding Field Analyzer. *Contrib. Plasma Phys.*, 50(9, SI):836–840, 2010.

[58] PC Stangeby. Interpretation of langmuir, heat-flux, deposition, trapping and gridded energy analyzer probe data for impure plasmas. *J. Phys. D Appl. Phys.*, 20(11):1472–1478, 1987.

[59] GY Antar, G Counsell, Y Yu, B Labombard, and P Devynck. Universality of intermittent convective transport in the scrape-off layer of magnetically confined devices. *Phys. Plasmas*, 10(2):419–428, 2003.

[60] I. Nanobashvili, J. P. Gunn, and P. Devynck. Radial profiles of plasma turbulent fluctuations in the scrape-off layer of the Tore Supra tokamak. *J. Nucl. Matter.*, 363:622–627, 2007.

[61] I. Nanobashvili, P. Devynck, J. P. Gunn, S. Nanobashvili, J. Stoeckel, and G. Van Oost. Comparative analysis of intermittent burst temporal characteristics at the edge of the CASTOR and Tore Supra tokamaks. *Phys. Plasmas*, 16(2), 2009.

[62] N. Fedorczak, J. P. Gunn, Ph. Ghendrih, P. Monier-Garbet, and A. Pocheau. Flow generation and intermittent transport in the scrape-off-layer of the Tore Supra tokamak. *J. Nucl. Matter.*, 390-91:368–371, 2009.

[63] N. Fedorczak, J. P. Gunn, J. Y. Pascal, Ph. Ghendrih, G. van Oost, P. Monier-Garbet, and G. R. Tynan. Electrostatic transport in L-mode scrape-off layer plasmas of Tore Supra tokamak. II. Transport by fluctuations. *Phys. Plasmas*, 19(7), 2012.

[64] O.E. Garcia, J. Horacek, R.A. Pitts, A.H. Nielsen, W. Fundamenski, V. Naulin, and J. Juul Rasmussen. Fluctuations and transport in the TCV scrape-off layer. *Nuc. Fusion*, 47(7):667, 2007.

[65] G.S. Xu, V. Naulin, W. Fundamenski, C. Hidalgo, J.A. Alonso, C. Silva, B. Goncalves, A.H. Nielsen, J. Juul Rasmussen, S.I. Krasheninnikov, B.N. Wan, M. Stamp, and JET EFDA Contributors. Blob/hole formation and zonal-flow generation in the edge plasma of the JET tokamak. *Nuc. Fusion*, 49(9):092002, 2009.

[66] J Cheng, L W Yan, W Y Hong, K J Zhao, T Lan, J Qian, A D Liu, H L Zhao, Yi Liu, Q W Yang, J Q Dong, X R Duan, and Y Liu. Statistical characterization of blob turbulence across the separatrix in HL-2A tokamak. *Plasma Phys. Control. Fusion*, 52(5):055003, 2010.

[67] B. Nold, G. D. Conway, T. Happel, H. W. Mueller, M. Ramisch, V. Rohde, U. Stroth, and ASDEX Upgrade Team. Generation of blobs and holes in the edge of the ASDEX Upgrade tokamak. *Plasma Phys. Control. Fusion*, 52(6), 2010.

[68] Samuel Karlin and Howard E Taylor. *A first course in stochastic processes*. Academic press, 1975.

[69] B. Nold, T. T. Ribeiro, M. Ramisch, Z. Huang, H. W. Mueller, B. D. Scott, U. Stroth, and ASDEX Upgrade Team. Influence of temperature fluctuations on plasma turbulence investigations with langmuir probes. *New J. Phys.*, 14, 2012.

[70] GR Hanson, JB Wilgen, E Anabitarte, JD Bell, JH Harris, JL Dunlap, and CE Thomas. ATF 2-frequency correlation reflectometer. *Rev. Sci. Instrum.*, 61(10, Part 2):3049–3051, 1990.

[71] TL Rhodes, WA Peebles, and EJ Doyle. The UCLA frequency tunable correlation reflectometer system on DIII-D. *Rev. Sci. Instrum.*, 63(10, Part 2):4661–4664, 1992.

[72] J Sanchez, B Branas, E Delaluna, and T Estrada. Swept frequency reflectometer for correlation studies in the TJ-I tokamak. *Rev. Sci. Instrum.*, 64(2):487–491, 1993.

[73] E Mazzucato and R Nazikian. Radial scale length of turbulent fluctuations in the main core of TFTR plasmas. *Phys. Rev. Lett.*, 71(12):1840–1843, 1993.

[74] R Nazikian, K Shinohara, GJ Kramer, E Valeo, K Hill, TS Hahm, G Rewoldt, S Ide, Y Koide, Y Oyama, H Shirai, and W Tang. Measurement of turbulence decorrelation during transport barrier evolution in a high-temperature fusion plasma. *Phys. Rev. Lett.*, 94(13), 2005.

[75] A. Kraemer-Flecken, S. Soldatov, B. Vowinkel, and P. Mueller. Correlation reflectometry at TEXTOR. *Rev. Sci. Instrum.*, 81(11), 2010.

[76] N. V. Kosolapova, E. Z. Gusakov, and S. Heuraux. Numerical modeling of micro turbulence wave number spectra reconstruction using radial correlation reflectometry: I. O-mode reflectometry at the linear plasma density profile. *Plasma Phys. Control. Fusion*, 54(3), 2012.

[77] TL Rhodes, WA Peebles, EJ Doyle, P Pribyl, M Gilmore, RA Moyer, and RD Lehmer. Signal amplitude effects on reflectometer studies of density turbulence in tokamaks. *Plasma Phys. Control. Fusion*, 40(4):493–510, 1998.

[78] T Estrada, J Sanchez, V Zhuravlev, E de la Luna, and B Branas. Turbulence and beam size effects on reflectometry measurements. *Phys. Plasmas*, 8(6):2657–2665, 2001.

[79] GD Conway. 2D modelling of radial correlation reflectometry. *Plasma Phys. Control. Fusion*, 39(3):407–421, 1997.

[80] E Blanco, T Estrada, and T Happel. Study of radial correlation reflectometry using a 2D full-wave code. In *Proc. 9th Intl. Reflectometry Workshop - IRW9 (Lisboa, May 2009)*, 2009.

[81] G. Leclert, S. Heuraux, E. Z. Gusakov, A. Yu Popov, I. Boucher, and L. Vermare. Full-wave test of the radial correlation reflectometry analytical theory in linear and nonlinear regimes. *Plasma Phys. Control. Fusion*, 48(9):1389–1400, SEP 2006.

[82] F Clairet, C Bottereau, JM Chareau, and R Sabot. Advances of the density profile reflectometry on TORE SUPRA. *Rev. Sci. Instrum.*, 74(3, Part 2, SI):1481–1484, 2003.

[83] L Vermare, F Clairet, S Heuraux, and G Leclert. Rational surface localization and MHD activity measurements using fast sweep reflectometry on Tore Supra. *Plasma Phys. Control. Fusion*, 47(11):1895–1909, 2005.

[84] R. Sabot, F. Clairet, G. D. Conway, L. Cupido, X. Garbet, G. Falchetto, T. Gerbaud, S. Hacquin, P. Hennequin, S. Heuraux, C. Honore, G. Leclert, L. Meneses, A. Sirinelli, L. Vermare, and A. Truc. Recent results on turbulence and MHD activity achieved by reflectometry. *Plasma Phys. Control. Fusion*, 48(12B, SI):B421–B432, 2006.

[85] J. F. Artaud, V. Basiuk, F. Imbeaux, M. Schneider, J. Garcia, G. Giruzzi, P. Huynh, T. Aniel, F. Albajar, J. M. Ane, A. Becoulet, C. Bourdelle, A. Casati, L. Colas, J. Decker, R. Dumont, L. G. Eriksson, X. Garbet, R. Guirlet, P. Hertout, G. T. Hoang, W. Houlberg, G. Huysmans, E. Joffrin, S. H. Kim, F. Koechl, J. Lister, X. Litaudon, P. Maget, R. Masset, B. Pegourie, Y. Peysson, P. Thomas, E. Tsitroneand, and F. Turco. The CRONOS suite of codes for integrated tokamak modelling. *Nuc. Fusion*, 50(4), 2010.

[86] P Maget, JF Artaud, LG Eriksson, G Huysmans, A Lazaros, P Moreau, M Ottaviani, JL Segui, and W Zwingmann. MHD activity triggered by monster sawtooth crashes on Tore Supra. *Plasma Phys. Control. Fusion*, 47(2):357–377, 2005.

[87] J. Schirmer, G. D. Conway, E. Holzhauer, W. Suttrop, H. Zohm, and ASDEX Upgrade Team. Radial correlation length measurements on ASDEX upgrade using correlation doppler reflectometry. *Plasma Phys. Control. Fusion*, 49(7):1019–1039, 2007.

[88] GR Mckee, C Fenzi, and RJ Fonck. Images of turbulence in a tokamak plasma. *IEEE T. Plasma. Sci.*, 30(1, Part 1):62–63, 2002.

[89] P. Hennequin, C. Honore, A. Truc, A. Quemeneur, C. Fenzi-Bonizec, C. Bourdelle, X. Garbet, G. T. Hoang, and Tore Supra Team. Fluctuation spectra and velocity profile from doppler backscattering on Tore Supra. *Nuc. Fusion*, 46(9):S771–S779, 2006.

[90] D. A. D'Ippolito, J. R. Myra, and S. J. Zweben. Convective transport by intermittent blob-filaments: Comparison of theory and experiment. *Phys. Plasmas*, 18(6), 2011.

[91] I. Nanobashvili, J. P. Gunn, and P. Devynck. Radial profiles of plasma turbulent fluctuations in the scrape-off layer of the Tore Supra tokamak. *J. Nucl. Matter.*, 363:622–627, 2007.

[92] N. Fedorczak, P. Manz, S. C. Thakur, M. Xu, G. R. Tynan, G. S. Xu, and S. C. Liu. On physical interpretation of two dimensional time-correlations regarding time delay velocities and eddy shaping. *Phys. Plasmas*, 19(12):122302, 2012.

[93] JL Segui, D Molina, G Giruzzi, M Goniche, G Huysmans, P Maget, M Ottaviani, and Tore Supra Team. An upgraded 32-channel heterodyne electron cyclotron emission radiometer on Tore Supra. *Rev. Sci. Instrum.*, 76(12), 2005.

[94] R. E. Waltz, J. C. DeBoo, and M. N. Rosenbluth. Magnetic-field scaling of dimensionally similar tokamak discharges. *Phys. Rev. Lett.*, 65:2390–2393, 1990.

[95] U Stroth, F Greiner, C Lechte, N Mahdizadeh, K Rahbarnia, and M Ramisch. Study of edge turbulence in dimensionally similar laboratory plasmas. *Phys. Plasmas*, 11(5):2558–2564, 2004.

[96] M Ramisch, N Mahdizadeh, U Stroth, F Greiner, C Lechte, and K Rahbarnia. rho(s) scaling of characteristic turbulent structures in the torsatron TJ-K. *Phys. Plasmas*, 12(3), 2005.

[97] P Simon. Comparative database analyses of plasma edge turbulence in fusion devices. Master's thesis, Stuttgart Universitaet.

[98] TL Rhodes, JN Leboeuf, RD Sydora, RJ Groebner, EJ Doyle, GR McKee, WA Peebles, CL Rettig, L Zeng, and G Wang. Comparison of turbulence measurements from DIII-D low-mode and high-performance plasmas to turbulence simulations and models. *Phys. Plasmas*, 9(5, 2):2141–2148, 2002.

[99] H Biglari, PH Diamond, and MN Rosenbluth. Toroidal ion-pressure-gradient-driven drift instabilities and transport revisited. *Phys. Fluids B-Plasma*, 1(1):109–118, 1989.

[100] B Kurzan, SD Hempel, E Holzhauer, B Scott, F Serra, W Suttrop, A Zeiler, and ASDEX Upgrade Team. Measurement and scaling of the radial correlation lengths of turbulence at the plasma edge of ASDEX Upgrade. *Plasma Phys. Control. Fusion*, 42(3):237–253, 2000.

[101] C. Bourdelle, X. Garbet, R. Singh, and L. Schmitz. New glance at resistive ballooning modes at the edge of tokamak plasmas. *Plasma Phys. Control. Fusion*, 54(11), 2012.

[102] VA Vershkov, SV Soldatov, DA Shelukhin, and VV Chistiakov. Experimental investigation of ion-temperature-gradient-like turbulence characteristics in T-10 core plasmas with toroidal and poloidal correlation reflectometry. *Nuc. Fusion*, 39(11Y, 2):1775–1783, 1999.

[103] A Kramer-Flecken, V Dreval, S Soldatov, A Rogister, V Vershkov, and TEXTOR-team. Turbulence studies with means of reflectometry at TEXTOR. *Nuc. Fusion*, 44(11):1143–1157, 2004.

[104] H. Arnichand, A. Kraemer-Flecken, S. Hacquin, and R. Sabot. Quasi coherent modes in TEXTOR and Tore Supra tokamaks. In *Proc. 11th Intl. Reflectometry Workshop - IRW11 (Palaiseau, April 2013)*, 2013.

[105] J. Wesson. *Tokamaks*. International Series of Monographs on Physics. OUP Oxford, 2011.

[106] VA Vershkov, DA Shelukhin, SV Soldatov, AO Urazbaev, SA Grashin, LG Eliseev, AV Melnikov, and T-10 team. Summary of experimental core turbulence characteristics in ohmic and electron cyclotron resonance heated discharges in T-10 tokamak plasmas. *Nuc. Fusion*, 45(10):S203–S226, 2005.

[107] C. Bourdelle, X. Garbet, F. Imbeaux, A. Casati, N. Dubuit, R. Guirlet, and T. Parisot. A new gyrokinetic quasilinear transport model applied to particle transport in tokamak plasmas. *Phys. Plasmas*, 14(11), 2007.

[108] Yong Xiao, Ihor Holod, Wenlu Zhang, Scott Klasky, and Zhihong Lin. Fluctuation characteristics and transport properties of collisionless trapped electron mode turbulence. *Phys. Plasmas*, 17(2), 2010.

[109] AM Dimits, G Bateman, MA Beer, BI Cohen, W Dorland, GW Hammett, C Kim, JE Kinsey, M Kotschenreuther, AH Kritz, LL Lao, J Mandrekas, WM Nevins, SE Parker, AJ Redd, DE Shumaker, R Sydora, and J Weiland. Comparisons and physics basis of tokamak transport models and turbulence simulations. *Phys. Plasmas*, 7(3):969–983, 2000.

[110] P H Diamond, S-I Itoh, K Itoh, and T S Hahm. Zonal flows in plasma, a review. *Plasma Phys. Control. Fusion*, 47(5):R35, 2005.

[111] R Gatto, PW Terry, and DA Baver. Nonlinear damping of zonal modes in anisotropic weakly collisional trapped electron mode turbulence. *Phys. Plasmas*, 13(2), 2006.

[112] Z Lin, TS Hahm, WW Lee, WM Tang, and PH Diamond. Effects of collisional zonal flow damping on turbulent transport. *Phys. Rev. Lett.*, 83(18):3645–3648, 1999.

[113] G F Matthews, M Beurskens, S Brezinsek, M Groth, E Joffrin, A Loving, M Kear, M-L Mayoral, R Neu, P Prior, V Riccardo, F Rimini, M Rubel, G Sips, E Villedieu, P de Vries, M L Watkins, and EFDA-JET contributors. JET ITER-like wall overview and experimental programme. *Phys. Scripta*.

[114] M Greenwald, JL Terry, SM Wolfe, S Ejima, MG Bell, SM Kaye, and GH Neilson. A new look at density limits in tokamaks. *Nuc. Fusion*, 28(12):2199–2207, 1988.

[115] M Greenwald. Density limits in toroidal plasmas. *Plasma Phys. Control. Fusion*, 44(8):R27–R80, 2002.

[116] GY Antar, G Counsell, and JW Ahn. On the scaling of avaloids and turbulence with the average density approaching the density limit. *Phys. Plasmas*, 12(8), 2005.

[117] M. Agostini, J. L. Terry, P. Scarin, and S. J. Zweben. Edge turbulence in different density regimes in Alcator C-Mod experiment. *Nuc. Fusion*, 51(5), 2011.

[118] B LaBombard, RL Boivin, M Greenwald, J Hughes, B Lipschultz, D Mossessian, CS Pitcher, JL Terry, SJ Zweben, and Alacator Grp. Particle transport in the scrape-off layer and its relationship to discharge density limit in Alcator C-Mod. *Phys. Plasmas*, 8(5, 2):2107–2117, 2001.

[119] DL Rudakov, JA Boedo, RA Moyer, PC Stangeby, JG Watkins, DG Whyte, L Zeng, NH Brooks, RP Doerner, TE Evans, ME Fenstermacher, M Groth, EM Hollmann, SI Krasheninnikov, CJ Lasnier, AW Leonard, MA Mahdavi, GR McKee, AG McLean, AY Pigarov, WR Wampler, G Wang, WP West, and CPC Wong. Far SOL transport and main wall plasma interaction in DIII-D. *Nuc. Fusion*, 45(12):1589–1599, 2005.

[120] B LaBombard, MV Umansky, RL Boivin, JA Goetz, J Hughes, B Lipschultz, D Mossessian, CS Pitcher, JL Terry, and Alacator Grp. Cross-field plasma transport and main-chamber recycling in diverted plasmas on Alcator C-Mod. *Nuc. Fusion*, 40(12):2041–2060, 2000.

[121] J. R. Myra, D. A. Russell, and D. A. D'Ippolito. Collisionality and magnetic geometry effects on tokamak edge turbulent transport. I. A two-region model with application to blobs. *Phys. Plasmas*, 13(11), 2006.

[122] OE Garcia, NH Bian, V Naulin, AH Nielsen, and JJ Rasmussen. Mechanism and scaling for convection of isolated structures in nonuniformly magnetized plasmas. *Phys. Plasmas*, 12(9), 2005.

[123] Y Sarazin and P Ghendrih. Intermittent particle transport in two-dimensional edge turbulence. *Phys. Plasmas*, 5(12):4214–4228, 1998.

[124] YL Sarazin. *Etude de la Turbulence de Bord dans les Plasmas de Tokamaks*. PhD thesis, Université Joseph Fourier-Grenoble 1, 1998.

[125] Y Sarazin, P Ghendrih, G Attuel, C Clement, X Garbet, V Grandgirard, M Ottaviani, S Benkadda, P Beyer, N Bian, and C Figarella. Theoretical understanding of turbulent transport in the SOL. *J. Nucl. Matter.*, 313:796–803, MAR 2003.

[126] M Becoulet, L Colas, S Pecoul, J Gunn, P Ghendrih, A Becoulet, and S Heuraux. Edge plasma density convection during ion cyclotron resonance heating on Tore Supra. *Phys. Plasmas*, 9(6):2619–2632, 2002.

[127] L. Colas, L. Costanzo, C. Desgranges, S. BrÃ©mond, J. Bucalossi, G. Agarici, V. Basiuk, B. Beaumont, A. BÃ©coulet, and F. Nguyen. Hot spot phenomena on Tore Supra ICRF antennas investigated by optical diagnostics. *Nuc. Fusion*, 43(1):1, 2003.

[128] A. Ekedahl, V. Basiuk, J. Bucalossi, L. Colas, Y. Corre, R. Dumont, L. G. Eriksson, M. Goniche, J. P. Gunn, F. Kazarian, L. Manenc, O. Meyer, P. Monier-Garbet, Ph. Moreau, F. G. Rimini, C. Balorin, G. Berger-By, L. Delpech, G. Lombard, L. Millon, P. Mollard, and M. Prou. RF coupling and antenna heat load control

for combined LHCD and ICRH in Tore Supra. In PM Ryan and DA Rasmussen, editors, *Radio Frequency Power In Plasmas*, volume 933 of *AIP CONFERENCE PROCEEDINGS*, pages 237–244. Amer Phys Soc, 2007. 17th Topical Conference on Radio Frequence Power in Plasmas, Clearwater, FL, MAY 07-09, 2007.

[129] S. J. Wukitch, B. Lipschultz, E. Marmar, Y. Lin, A. Parisot, M. Reinke, J. Rice, J. Terry, and C-Mod Team. RF plasma edge interactions and their impact on ICRF antenna performance in Alcator C-Mod. *J. Nucl. Matter.*, 363:491–497, 2007.

[130] Vl. V. Bobkov, F. Braun, R. Dux, A. Herrmann, A. Kallenbach, R. Neu, J.-M. Noterdaeme, Th. Puetterich, and ASDEX Upgrade Team. Compatibility of ICRF antennas with W-coated limiters for different plasma geometries in ASDEX Upgrade. *J. Nucl. Matter.*, 363:122–126, 2007.

[131] L Colas. Heat Load Patterns on Tore Supra ICRH Antennas. In *Proceedings of 27th European Physical Society (EPS) Conference on Controlled Fusion and Plasma Physics, Budapest, 2000)*, 2000.

[132] G. Antar, S. Assas, V. Bobkov, J. M. Noterdaeme, E. Wolfrum, A. Herrmann, V. Rohde, and ASDEX Upgrade Team. Convective transport suppression in the scrape-off layer using ion cyclotron resonance heating on the ASDEX Upgrade tokamak. *Phys. Rev. Lett.*, 105(16), 2010.

[133] G. Y. Antar, M. Goniche, A. Ekedahl, and L. Colas. The role of power and magnetic connection to the active antenna in the suppression of intermittent structures by ion cyclotron resonance heating. *Nuc. Fusion*, 52(10), 2012.

[134] K. Vulliez, L. Colas, A. Argouarch, A. Mendes, C. Hamlyn-Harris, A. Ekedahl, and J. C. Patterlini. A new faraday screen for Tore Supra ICRH Antenna. *AIP Conf. Proc.*, 1187(1):145–148, 2009.

[135] L. Colas, A. Argouarch, S. Brémond, M. Chantant, Y. Corre, M. Firdaouss, M. Goniche, D. Guilhem, J.-P. Gunn, J. Jacquot, M. Kubic, X. Litaudon, G. Lombard, O. Meyer, P. Mollard, and K. Vulliez. RF-sheath patterns modification via novel Faraday screen and strap voltage imbalance on Tore Supra ion cyclotron antennae . *J. Nucl. Matter.*, 438, Supplement(0):S330 – S333, 2013.

[136] FW Perkins. Radiofrequency sheaths and impurity generation by ICRF antennas. *Nuc. Fusion*, 29(4):583–592, 1989.

[137] JM Noterdaeme and G Vanoost. The interaction between waves in the ion-cyclotron range of frequencies and the plasma boundary. *Plasma Phys. Control. Fusion*, 35(11):1481–1511, 1993.

[138] M Kubic, J Gunn, L Colas, S Heuraux, and E Faudot. Measurements of RF-induced sol modifications in Tore Supra tokamak. In *Proceedings of 20th International Conference on Nuclear Engineering ICONE 2012*, 2012.

[139] P Ghendrih, Y Sarazin, G Attuel, S Benkadda, P Beyer, G Falchetto, C Figarella, X Garbet, V Grandgirard, and M Ottaviani. Theoretical analysis of the influence of external biasing on long range turbulent transport in the scrape-off layer. *Nuc. Fusion*, 43(10):1013–1022, 2003.

[140] CF Figarella, P Ghendrih, Y Sarazin, G Attuel, S Benkadda, P Beyer, G Falchetto, E Fleurence, X Garbet, and V Grandgirard. Control of long range turbulent transport with biasing in the tokamak scrape-off-layer. *J. Nucl. Matter.*, 337(1-3):342–346, 2005.

[141] L Colas. Linear and non-linear physics of high power radio-frequency waves in the edge of magnetized plasmas., 2009.

[142] L. Colas. private communication, 2013.

[143] G. Y. Antar, M. Goniche, A. Ekedahl, and L. Colas. On the interaction between the ion cyclotron resonance heating and scrape-off layer turbulence via sound waves. *Phys. Rev. Lett.*, 2013. Submitted.

[144] R. Ochoukov, D.G. Whyte, D. Brunner, I. Cziegler, B. LaBombard, B. Lipschultz, J. Myra, J. Terry, and S. Wukitch. Investigation of RF-enhanced plasma potentials on Alcator C-Mod . *J. Nucl. Matter.*, 438, Supplement(0):S875 – S878, 2013.

[145] D.A. D'Ippolito, J.R. Myra, R. Ochoukov, and D.G. Whyte. Modeling far-field radio-frequency sheaths in Alcator C-Mod. *Plasma Phys. Control. Fusion.*

[146] I. Sandberg, S. Benkadda, X. Garbet, G. Ropokis, K. Hizanidis, and D. del Castillo-Negrete. Universal probability distribution function for bursty transport in plasma turbulence. *Phys. Rev. Lett.*, 103(16), 2009.

[147] O. E. Garcia. Stochastic modeling of intermittent scrape-off layer plasma fluctuations. *Phys. Rev. Lett.*, 108(26), 2012.

[148] F Clairet. Réflectométrie de balayage en fréquence sur le tokamak Tore Supra, 2007.

[149] GR Mckee, C Fenzi, and RJ Fonck. Images of turbulence in a tokamak plasma. *IEEE T. Plasma. Sci.*, 30(1, Part 1):62–63, 2002.

[150] JL Terry, R Maqueda, CS Pitcher, SJ Zweben, B LaBombard, ES Marmar, AY Pigarov, and G Wurden. Visible imaging of turbulence in the SOL of the Alcator C-Mod tokamak. *J. Nucl. Matter.*, 290:757–762, 2001.

[151] S J Zweben, J A Boedo, O Grulke, C Hidalgo, B LaBombard, R J Maqueda, P Scarin, and J L Terry. Edge turbulence measurements in toroidal fusion devices. *Plasma Phys. Control. Fusion*, 49(7):S1, 2007.

[152] E Trier. *Champ électrique radial dans les plasmas de tokamak non axi-symétrique, étude par réflectométrie Doppler*. PhD thesis, Ecole Polytechnique, 2010.